ALMA MATER STUDIORUM
UNIVERSITÀ DI BOLOGNA

DOTTORATO DI RICERCA IN

CHIMICA

Ciclo 36

Settore Concorsuale: 03/A2 - MODELLI E METODOLOGIE PER LE SCIENZE CHIMICHE

Settore Scientifico Disciplinare: CHIM/02 - CHIMICA FISICA

EXPLORING ELECTRIC FIELD APPLICATIONS IN CHEMISTRY: A MULTISCALE INVESTIGATION

Presentata da: Marco Severi

Coordinatore Dottorato

Luca Prodi

Supervisore

Francesco Zerbetto

Co-supervisore

Elisabetta Venuti

Esame finale anno 2024

Contents

Abstract

Electric fields have gained a prominent role in modern chemistry. From the first spectroscopic investigations, through catalysis, to their role in solar cells, the application of electric fields at the interface with chemistry is the most diverse. The variety of applications of electric fields necessitates, when viewed from a theoretical standpoint, a set of methodologies for both modeling and simulation. This doctoral thesis reports three investigations exploring phenomena induced by electric fields, each one described with a distinct level of theory.

The thesis commences with the application of time-dependent perturbation theory to a transflection spectroscopy setup, a widely adopted approach for analyzing real samples, aiming to interpret the artifacts in the absorption spectra.

Subsequently, the thesis introduces a novel model for electrostatic catalysis. Electrostatic catalysis does not employ light, as traditional photocatalysis, but a static electric field. The model determines the amplitude and direction of the field for the optimal catalysis of a chemical reaction.

In its final investigation, the thesis employs a quantum model of the electric field to describe the formation of hybrid light-matter states and their catalytic effects on molecular isomerizations.

Chapter 1

Introduction

The word "field" was introduced in physics by Michael Faraday in 1849 [1]. Initially introduced as mathematical tools, fields have since evolved to be regarded as fundamental constituents of the universe, as particles are. This conceptual transformation has not only had a profound impact on physics but has also extended its influence into other scientific disciplines, notably in the field of chemistry.

In chemistry, the electromagnetic field plays a prominent role. Two paradigmatic examples are: firstly, the interaction between the electromagnetic field and the human eye is fundamental for the process of vision [2]. Here, vision emerges as a consequence of the interplay between matter and a classical oscillating electric field. Secondly, the electric field is responsible for a large part of the catalytic effects observed in enzymes [3]. In this case, enzyme catalysis is the outcome of the interaction between matter and a classical static electric field.

The surge of quantum field theory improved drastically the comprehension of the electromagnetic field, giving a strong theoretical justification to the existence of photons and leading to advances in all areas of physics. In chemistry, quantum field theory is crucial to understand spontaneous emission [4] and the theoretical description of photons led to new experimental techniques based on the control of a few (or a single) photons, such as ultrafast spectroscopies [5] and quantum imaging techniques [6].

This overview, while far from exhaustive, serves as an example of the rich applicability of electric fields in chemistry. The interplay between electric fields and matter in various experimental setups is often non-trivial, posing challenges in result interpretation. In this context, computational methods emerge as tools to reach a deeper comprehension of chemical processes under the effect of electric fields.

The purpose of this thesis is to computationally study chemical phenomena modified by the presence of electric fields. The investigation reported here is multiscale: it adopts different levels of approximation regarding the description of matter, field and their interaction. To structure this study, three phenomena have been selected, and for each, a distinct level of theoretical approximation has been employed, progressing from coarser to more refined models. Each of these phenomena corresponds to a dedicated chapter within the thesis.

In Chapter 2, the focus is on spectroscopy, which represents a traditional

application of electric fields in chemistry. In this context, matter interacts with a classical oscillating electric field, specifically in transflection spectroscopy. This widely used technique involves placing a sample on a reflective plate, where light interacts twice with the sample—before and after reflection. This setup leads to deviations from the usual absorption experiments, primarily due to the formation of an electric field standing wave within the sample [7]. Theoretical modeling serves as a useful tool in interpreting these experiments. In this approach, matter is considered as a collection of simple two-level systems, and the field is viewed as a sinusoidal wave. The interaction between the field and matter is treated within the framework of time-dependent perturbation theory, applied to both linear and non-linear absorption phenomena.

Chapter 3 advances to a more accurate description of matter while retaining a classical description of the electric field. The chapter focuses on electrostatic catalysis, that is the usage of a static electric field to catalyze a chemical reaction. This application of electric fields gained popularity in the last two decades and several theoretical and experimental investigations have been published [8]. In this context, one of the central problems is how to determine the direction and strength of the electric field able to catalyze the reaction. In this thesis, a model is presented and applied in order to find the smallest electric field able to remove the reaction barrier. The method considers explicitly the molecular structure, describing the molecule through the common quantum mechanical electronic structure methods, while the field is simply classical and static.

Chapter 4 is the last step in the scale of the approximations, describing both the molecules and the electric field at the quantum mechanical level. The focus shifts to the formation of hybrid light-matter states, called polaritons. The generation of polaritons, mostly formed inside micro and nanocavities, can ease or hinder a chemical reaction, or even modify its mechanism. Generally, these phenomena are grouped in the research field called polaritonic chemistry [9]. Theoretical modeling of hybrid light-matter states requires a description of matter and light on the same footing, therefore it is necessary to consider the quanta of the electric field, that is the photons. This leads to a new class of electronic structure methods, able to solve an Hamiltonian that takes into account the molecule, the photons and their interaction. These new methods are briefly described and then applied to simple polyenic isomerizations.

References

[1] Steven Weinberg. “The Search for Unity: Notes for a History of Quantum Field Theory”. In: *Daedalus* 106.4 (1977), pp. 17–35. ISSN: 00115266. URL: http://www.jstor.org/stable/20024506.

[2] Vitalijs Zubkovs et al. “Single vs. two-photon microscopy for label free intrinsic tissue studies in the UV light region”. In: *Analyst* 139 (11 2014), pp. 2663–2667. DOI: 10.1039/C4AN00203B. URL: http://dx.doi.org/10.1039/C4AN00203B.

[3] Stephen D. Fried and Steven G. Boxer. "Electric Fields and Enzyme Catalysis". In: *Annual Review of Biochemistry* 86.1 (2017). PMID: 28375745, pp. 387–415. DOI: 10.1146/annurev-biochem-061516-044432. URL: https://doi.org/10.1146/annurev-biochem-061516-044432.

[4] Orazio Svelto. *Principles of Lasers*. en. Boston, MA: Springer US, 2010. ISBN: 978-1-4419-1301-2. DOI: 10.1007/978-1-4419-1302-9. URL: http://link.springer.com/10.1007/978-1-4419-1302-9.

[5] Margherita Maiuri, Marco Garavelli, and Giulio Cerullo. "Ultrafast Spectroscopy: State of the Art and Open Challenges". In: *J. Am. Chem. Soc.* 142.1 (Jan. 2020). Publisher: American Chemical Society, pp. 3–15. ISSN: 0002-7863. DOI: 10.1021/jacs.9b10533. URL: https://doi.org/10.1021/jacs.9b10533.

[6] Marta Gilaberte Basset et al. "Perspectives for Applications of Quantum Imaging". en. In: *Laser & Photonics Reviews* 13.10 (2019), p. 1900097. ISSN: 1863-8899. DOI: 10.1002/lpor.201900097. URL: https://onlinelibrary.wiley.com/doi/abs/10.1002/lpor.201900097.

[7] Jacob Filik et al. "Electric field standing wave artefacts in FTIR microspectroscopy of biological materials". In: *Analyst* 137 (4 2012), pp. 853–861. DOI: 10.1039/C2AN15995C. URL: http://dx.doi.org/10.1039/C2AN15995C.

[8] Sason Shaik and Thijs Stuyver, eds. *Effects of Electric Fields on Structure and Reactivity*. New Horizons in Chemistry, Theoretical and Computational Chemistry Series. The Royal Society of Chemistry, 2021, pp. 001–428.

[9] Thomas W. Ebbesen. "Hybrid Light–Matter States in a Molecular and Material Science Perspective". In: *Acc. Chem. Res.* 49.11 (Nov. 2016). Publisher: American Chemical Society, pp. 2403–2412. ISSN: 0001-4842. DOI: 10.1021/acs.accounts.6b00295. URL: https://doi.org/10.1021/acs.accounts.6b00295.

Chapter 2

Transflection Spectroscopy

This first chapter approaches light-matter interaction from a simple semiclassical point of view. Matter is treated as a set of energy levels and the electromagnetic field is classical. Such a simple model has been employed to study a variety of field effects, for instance the Stark and Zeeman effects [1].

Of special importance is the study of the interaction of matter with an oscillating field, which opens the gates to the field of spectroscopy. A simple two-level system interacting with an oscillating electric field has been used as a model to predict and interpret experiments such as the stimulated absorption or the two-photon spectroscopy, or to derive laws as the Fermi golden rule.

Even though more accurate models are now available, based on a quantum description of the electromagnetic field, a simplified approach still gives valuable insights, especially when a fully quantum approach is hardly applicable. One of these is the description of real spectroscopic techniques, where it is considerably easier to describe the process in classical terms.

This chapter analyzes from a theoretical point of view one of these techniques: transflection spectroscopy. Transflection spectroscopy is widely used in the analysis of real samples and a deep theoretical understanding is useful in interpreting the spectra and in predicting the absorption patterns.

In fact recently, there has been a growing interest in the use of non-destructive spectroscopic techniques to study samples of diverse origins in the conditions in which they were found or applied. This approach is becoming a necessity for far-afield areas that range from biology to medicine to cultural heritage [2–8]. Among the most popular techniques are UV-vis, infrared and Raman spectroscopy, which can also be used microscopically [9–18].

One historically popular approach to the spectroscopy of real samples is to perform measurements in reflection-absorption, also called transflection [19–21]. In this setup, the sample is placed on top of a reflective plate. Light passes through the sample, is reflected, passes again through the sample, and reaches the detector. The optical path is doubled and the absorbance increases. According to the Beer-Lambert law, the absorbance should increase linearly with the length of the optical path. However, several experiments have disproven this hypothesis [22–27]. Previous investigations have identified deviations from the Beer-Lambert law, attributing these anomalies to the influence of an electric field standing wave

(EFSW) in the optical absorption process. Classical optical theories suggest the generation of standing waves through the interference of incident and reflected waves upon the reflection of a traveling wave. Contrary to these classical expectations, it has been demonstrated that EFSW phenomena manifest for arbitrary substrates with layers of moderate thickness, even in transmission setups[28–30]. Beyond the EFSW contribution, non-linearity in absorption is also linked to scattering phenomena, such as Mie scattering. Importantly, these two sources of aberrations are not interconnected. Here, Mie scattering is not considered and the focus is solely on the EFSW. Excellent references regarding the aberrations due to Mie scattering can be found in refs.[31–36].

Previous studies have addressed deviations from linearity in absorption using classical wave optics-based methodologies, which have provided excellent results in absorbance calculations [29]. However, a quantum mechanical approach offers a molecular-level comprehension of the EFSW effects. This approach evaluates the effect of the standing wave on the absorption on a single chemical entity, which holds potential significance in the analysis of systems where a molecule serves as a diagnostic indicator for chemical processes, such as in the study of disease-modified biological tissues [5, 26]. Specifically, alterations in vibrational patterns or shifts in electronic transitions induced by standing waves may compromise the diagnostic efficacy of the probe molecule [26].

The aim of this chapter is a treatment of transflection spectroscopy based on time-dependent perturbation theory, with application to both electronic and vibrational spectroscopy. This approach allows to disentangle the effects of standing waves and traveling waves on individual molecules at both linear and non-linear levels. Furthermore, the proposed methodology is well-suited for materials characterized by planar layers, where the regularity of layers diminishes Mie scattering, allowing for its neglect as a first-order approximation [24, 37, 38].

Given that experimental studies predominantly operate within the linear intensity regime, the initial effort lies on linear transitions induced by the simultaneous presence of standing and traveling waves. Nevertheless, the study extends to the non-linear regime, recognizing that the combined influence of standing and propagating waves can enhance the effective field experienced by the molecule.

Section 2.1 presents a concise treatment of time-dependent perturbation theory, collecting all the results needed for the application to transflection spectroscopy. The mathematical framework outlined is then applied to linear and non-linear transitions in section 2.2.

2.1 Brief Review of Time-Dependent Perturbation Theory

This introduction to time-dependent perturbation theory is mainly taken from[39], the exposition may be somewhat different from the modern textbook material but elegantly and concisely leads to the important results.

Assume that a system can be described through the time independent $\hat{H}_0$ Hamiltoninan. On the system acts a perturbation, which lasts for a certain amount

of time τ. The operator associated with the perturbation is therefore

$$V(t) = \begin{cases} W(t) \text{ if } 0 \leq t \leq \tau \\ 0 \text{ if } t < 0 \text{ or } t > \tau \end{cases} \tag{2.1}$$

it follows that the time dependent Hamiltonian is

$$\hat{H} = \hat{H}_0 + \hat{V}(t) \tag{2.2}$$

and the associated Schrödinger equation is solved by non stationary states. In many cases the $\hat{V}(t)$ describes the interaction of the system with the environment or with an external body, here will later characterize an external electric field.

A solution of the time-dependent Schrödinger equation can be written as

$$\Psi = \sum_n c_n \psi_n \exp\left\{-iE_n \frac{t}{\hbar}\right\} \tag{2.3}$$

where ψ_n and E_n are the eigenfunctions and eigenvalues of the $\hat{H}_0$ operator. Now the task it to determine the c_n coefficients.

It is reasonable to assume that for $t < 0$ (perturbation off) the system is in a stationary state with E_l energy. Therefore the eigenfunction for $t < 0$ is

$$\Psi_{initial} = c_l \psi_l \exp\left\{-iE_l \frac{t}{\hbar}\right\} \tag{2.4}$$

After the perturbation ($t > \tau$) the system will be in a final state which depends on the perturbation operator, the perturbation time and the initial state.

$$\Psi_{final} = \sum_f c_{fl} \psi_f \exp\left\{-iE_f \frac{t}{\hbar}\right\} \tag{2.5}$$

the c_{fl} notation has been adopted to underline the dependency of the final state coefficients on the initial state.

From the principles of quantum mechanics the probability that the system is in one of the ψ_f eigenstates is given by the square of the modulus of the coefficient [40]. The quantity

$$M_{fl}(\tau) = |c_{fl}(\tau)|^2 \tag{2.6}$$

is equal to the transition probability from the initial state l to the final state f, during a time τ.

To compute the c_{fl} coefficients it sufficient to put eq. (2.3) in the time-dependent Schrödinger equation, multiply both the terms by ψ_f and integrate over the entire configuration space. The resulting system of equations is

$$i\hbar \frac{d}{dt} c_f(t) = \sum_l \langle \psi_f | \hat{W}(t) | \psi_l \rangle e^{i\omega_{fl} t} c_l(t) \tag{2.7}$$

where

$$\omega_{fl} = \frac{E_f - E_l}{\hbar} \tag{2.8}$$

For simplicity it is convenient to consider only the set of perturbation operators $\hat{W}$ such as $\langle\psi_f|\,\hat{W}(t)\,|\psi_l\rangle = 0$. This is equivalent to saying that the shifts of the energy levels due to the perturbation are neglected, in the context of computing the transitions probabilities it is a widely adopted approximation.

Another reasonable approximation is to consider that, at $t = 0$, the system is in the state ψ_l or in the state ψ_f, which can be translated to

$$c_f(t=0) = \delta_{fl} \tag{2.9}$$

Assuming that the perturbation is weak and short, the c_f variation after a time τ is small, therefore eq. (2.7) can be solved with the successive approximations method.

The first order approximation of the c_f coefficient can be constructed substituting eq. (2.9) into eq. (2.7), which leads to (for a single fixed ψ_l)

$$i\hbar\frac{d}{dt}c_{fl}^{(1)}(t) = \langle\psi_f|\,\hat{W}(t)\,|\psi_l\rangle\, e^{i\omega_{fl}t} \tag{2.10}$$

, which can be solved recurring to the initial conditions defined in eq. (2.9)

$$c_{fl}^{(1)}(t) = \frac{1}{i\hbar}\int_0^t \langle\psi_f|\,\hat{W}(t')\,|\psi_l\rangle\, e^{i\omega_{fl}t'}dt' \tag{2.11}$$

The approximation of c_f including the second order terms is found by substituting eq. (2.11) into the right term of eq. (2.7).

$$\begin{aligned} &i\hbar\frac{d}{dt}c_{fl}^{(2)}(t) = \langle\psi_f|\,\hat{W}(t)\,|\psi_l\rangle\, e^{i\omega_{fl}t} + \\ &\frac{1}{i\hbar}\sum_{f'(f'\neq l)}\langle\psi_f|\,\hat{W}(t')\,|\psi_{f'}\rangle\, e^{i\omega_{ff'}t'}\int_0^t \langle\psi_{f'}|\,\hat{W}(t')\,|\psi_l\rangle\, e^{i\omega_{f'l}t'}dt' \end{aligned} \tag{2.12}$$

which leads to

$$\begin{aligned} c_{fl}^{(2)}(t) &= \frac{1}{i\hbar}\int_0^t \langle\psi_f|\,\hat{W}(t')\,|\psi_l\rangle\, e^{i\omega_{fl}t'}dt' + \\ &+ \left(\frac{1}{i\hbar}\right)^2\sum_{f'(f'\neq l)}\int_0^t \langle\psi_f|\,\hat{W}(t')\,|\psi_{f'}\rangle\, e^{i\omega_{ff'}t'}\times\int_0^{t'} \langle\psi_{f'}|\,\hat{W}(t'')\,|\psi_l\rangle\, e^{i\omega_{f'l}t''}dt''dt' \end{aligned} \tag{2.13}$$

Repeating the same substitution into eq. (2.7) it is possible to compute the coefficients with an arbitrary order of approximation, leading to an infinite (or Dyson) series. For the majority of chemical applications and the cases covered in this chapter a second order approximation is sufficient and, therefore, higher approximations will not be discussed.

This brief review of time-dependent perturbation theory paves the ground to spectroscopic applications, in which the central quantity is the transition probability. It is worth writing explicitly a general expression for the transition probability from an initial state ψ_l to a final state ψ_f computed at the first order of approximation

$$M_{fl}(\tau) = \left|c_{fl}^{(1)}(\tau)\right|^2 = \frac{1}{\hbar^2}\left|\int_0^\tau \langle\psi_f|\,\hat{W}(t)\,|\psi_l\rangle\, e^{i\omega_{fl}tdt}\right|^2 \tag{2.14}$$

2.2 Results and Discussion

Following a concise overview of time-dependent perturbation theory, this section delves into the theoretical modeling of transflection spectroscopy.

In transflection spectroscopy a travelling wave hits the sample, is reflected, interferes forming a standing wave and is eventually detected.

The starting point is the semiclassical definition of electric fields associated with both propagating and standing waves. The 1D electric field associated with the propagating wave (EFPW) is given by

$$E_{\text{prop}} = A\cos(kx - \omega t) \tag{2.15}$$

while the corresponding standing wave is

$$E_{\text{stand}} = 2A\cos(kx)\cos(\omega t) \tag{2.16}$$

where A is the amplitude, k is the spatial angular frequency, x is the distance from the reflecting plate, ω is the frequency of the wave and t is time. For simplicity, the index of refraction is set to one. The approach can be trivially extended to a 3-dimensional problem. The choice of considering the standing wave uniform through the whole medium concurs with recent finding that the standing wave does propagate through the whole medium and its effects are not limited to the neighborhoods of the reflective surface[29, 30]. Furthermore, two waves propagating in the same direction and perpendicular to the reflecting substrate are examined, which avoids the suppression of the component of the electric field parallel to the surface. Nevertheless the model can take into account the suppression due to the metal surface modulating the amplitude of the travelling or standing wave.

Figure 2.1 represents the electric field as a function of the distance, x, from the reflecting plate, after an arbitrary time of $\approx 70\,\text{fs}$. Notably, the plot is configured to showcase a node of the stationary wave at $x = 0$. Beyond trivial changes in intensity, the distinguishing feature among the curves is the position of the minima. The first minima for the standing and traveling waves can be analytically determined, while for their combination, the position can be found numerically.

2.2.1 Linear Transitions

Considering the semiclassical interaction between light and matter, the Hamiltonian is given by

$$\hat{H} = \hat{H}_{\text{mol}} + \hat{\mu}E \tag{2.17}$$

where $\hat{H}_{\text{mol}}$ is the molecular Hamiltonian, $\hat{\mu}$ is the dipole moment operator and E is here the sum of the electric fields of the EFPW and EFSW. The associated Schrödinger equation can be solved using first-order time-dependent perturbation theory (section 2.1). For a weak perturbation applied for a short time, the evolution from an initial state, Ψ_{I}, to a final state, Ψ_{F}, is described by

$$P_{\text{IF}}(t) = |c_{\text{IF}}(t)|^2 = \left| \int_0^t -\frac{i}{\hbar} V_{\text{FI}} e^{\frac{i(\varepsilon_{\text{F}} - \varepsilon_{\text{I}})t'}{\hbar}} \mathrm{d}t' \right|^2 \tag{2.18}$$

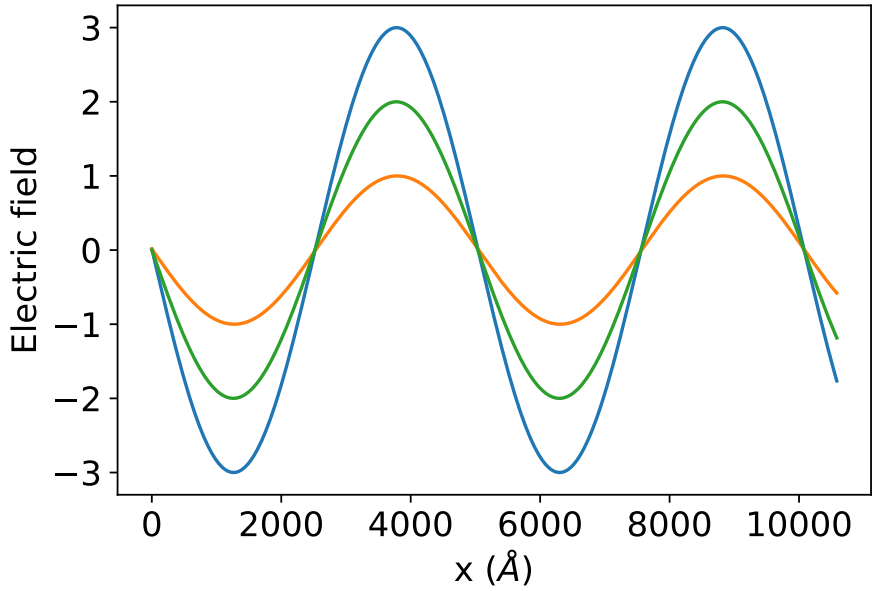

Figure 2.1: Electric fields of the travelling wave (orange line), standing wave (green line), and sum of the two (blue line). The parameters were $\omega = 20\,000\,\mathrm{cm}^{-1}$, $k = 0.001\,26\,\text{Å}^{-1}$, $t = 70$ fs, $A = 1\ \mathrm{Vm}^{-1}$.

where ε_I and ε_F are the energies of the initial and the final state. The rotating wave approximation allows to simplify the $V_\mathrm{FI} = \int_{R^\mathrm{n}} \Psi_\mathrm{F}^* \hat{\mu} E \Psi_\mathrm{I} dx$ integral, that is E is taken as constant in the infinitesimal dx range. Equation (2.18) becomes

$$P_\mathrm{IF}(t) = |c_\mathrm{IF}(t)|^2 = \left| \int_0^t -\frac{i}{\hbar} E(t') \mu_\mathrm{FI} e^{i\omega_\mathrm{FI} t'} \mathrm{d}t' \right|^2 \tag{2.19}$$

where $\omega_\mathrm{FI} = \frac{\varepsilon_\mathrm{F} - \varepsilon_\mathrm{I}}{\hbar}$ and $\mu_\mathrm{FI} = \int_{R^\mathrm{n}} \Psi_\mathrm{F}^* \hat{\mu} \Psi_\mathrm{I} dx$ to yield

$$\begin{aligned} c_\mathrm{IF} = \frac{A\mu_\mathrm{FI}}{\hbar} \Bigg[& \frac{1 - e^{i(\omega_\mathrm{FI} - \omega)t}}{\omega_\mathrm{FI} - \omega} \left(\cos(kx) + \frac{e^{ikx}}{2} \right) \\ & + \frac{1 - e^{i(\omega_\mathrm{FI} + \omega)t}}{\omega_\mathrm{FI} + \omega} \left(\cos(kx) + \frac{e^{-ikx}}{2} \right) \Bigg] \end{aligned} \tag{2.20}$$

where A is the field amplitude as in eqs. (2.15) and (2.16).

It is essential to note that these equations are applicable in 1D. If the molecular dipole moment is perpendicular to the field, the model predicts no absorption and no modifications due to the EFSW. However, in real samples, absorption can still occur due to scattering, such as Mie scattering, which changes the direction of the propagating wave.

Figure 2.2 presents the calculated maximal transition probability as a function of x and its associated integrated transition probability. Such maximal probability is reached when $\omega = \omega_\mathrm{FI}$. The orange line represents the result for the Electric Field Propagating Wave (EFPW), showing minimal dependence of the maximum intensity on the position, while its integrated intensity follows a Beer-Lambert-like behavior, as shown in fig. 2.2b. In contrast, the integrated probability of the

standing wave oscillates periodically within the sample, going through a minimum where there is no absorption. The locations of these minima inside the material are governed by the value of k. Consequently, the Beer-Lambert law is not strictly satisfied. The model predicts that absorbance (related to the transition probability) oscillates as the sample location is modified, resembling experimental observations when the sample is moved towards and away from the mirror [24].

Interestingly, the black dotted line in fig. 2.2a shows that the contributions of EFSW and EFPW are *additive*: the total transition probability is the sum of the EFPW plus twice the EFSW. This result can be justified on a trigonometric basis, implying that if the standing wave contribution were experimentally obtained, the propagating wave term would also become accessible. Up to 50 nm, the effect of the EFSW is to introduce a small perturbation of the usual Beer-Lambert law. Moreover, in fig. 2.2b there is a region where the orange line is above the green line. In this region, the contribution to the absorbance due to EFPW is greater than the contribution to the absorbance due to the EFSW.

The curve associated to the integrated absorption probability of the standing wave can be fitted by

$$\int_0^l sin^2(kx)dx = \frac{l}{2} - \frac{\sin(2kl)}{4k} \tag{2.21}$$

which is consistent with the result obtained experimentally in [22]. The curve associated to the linear combination of the two electric fields can be fitted by

$$\int_0^l \left(\frac{e^{ikx}}{2} + cos(kx)\right)\left(\frac{e^{-ikx}}{2} + cos(kx)\right)dx = \frac{\sin(2kl)}{2k} + \frac{5l}{4} \tag{2.22}$$

These equations can be used to identify the dominant contributions to experimental results of transflection experiments.

As an illustration, two cases are examined. In a study by Bassan et al. [26] cytosine IR spectra were measured as a function of sample thickness. The general trend was that as the film thickness increased, more IR radiation was absorbed but not in the expected linear fashion across the spectrum. From the experimental data, the authors calculated the ratio of the absorbance values at 3300 cm^{-1} and 1655 cm^{-1} for the N–H stretch and Amide I bands. In the context of the present model, an explanation can be put forward. The CO bonds whose stretching is responsible for amide band I are oriented differently from the NH bonds. The standing wave affects them differently. The model suggests that the Amide band I that increases its intensity with the thickness of the layer is interacting more with the EFSW than the NH stretch. The apparatus proposed below could be employed to experimentally validate this hypothesis. In the investigation by Staniszewska-Slezak et al.[5], IR spectra recorded in transflection mode exhibited a significant shift in the amide I band (up to 1667 cm^{-1}) in comparison to the one recorded in transmission (1658 cm^{-1}) as a function of the thickness of the material. Again, a hypothesis similar to the previous one can be proposed on the basis of the present model. In the material layers, the CO bonds of the Amide I band have diverse orientations. With transflection, the appearance of EFSW results in higher absorbance for CO bonds aligned along the field, leading to shifts in the most intense bands. Thus, the formation of EFSW, along with the model, could offer structural insights.

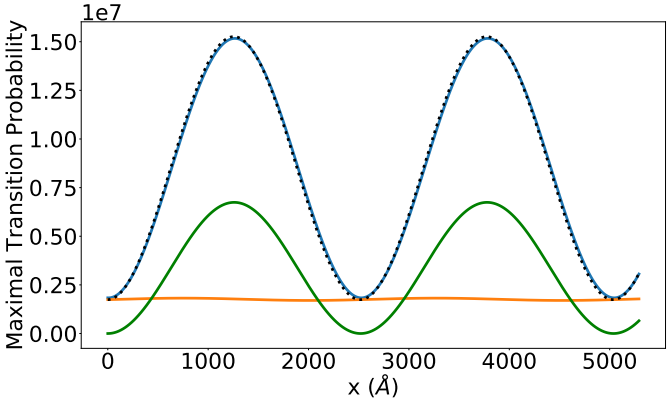

(a)

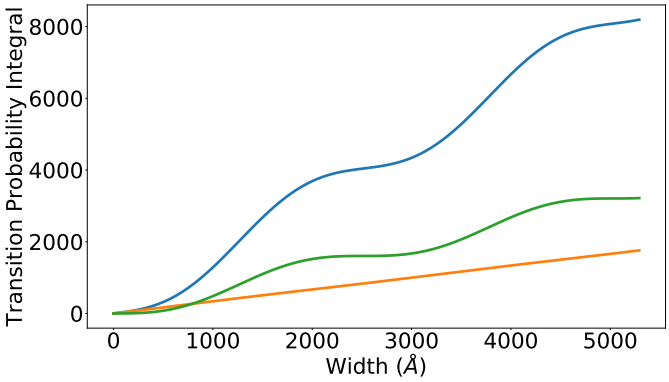

(b)

Figure 2.2: (a) Non normalized maximal transition probability in the linear regime as a function of the position in the absorbing sample. (b) Integral of the curves of (a) calculated as a function of the width of the sample. Travelling wave (orange line), standing wave (green line), and the combinations of the two (blue line). The black dotted line is the difference between the blue curve and the sum of the orange and green curves. Parameters are $\omega = 20000$ cm^{-1}, $k = 0.00126$ Å^{-1}, $t = 70$ fs, $A\mu_{\mathrm{FI}}/\hbar = 1$ cm^{-1}

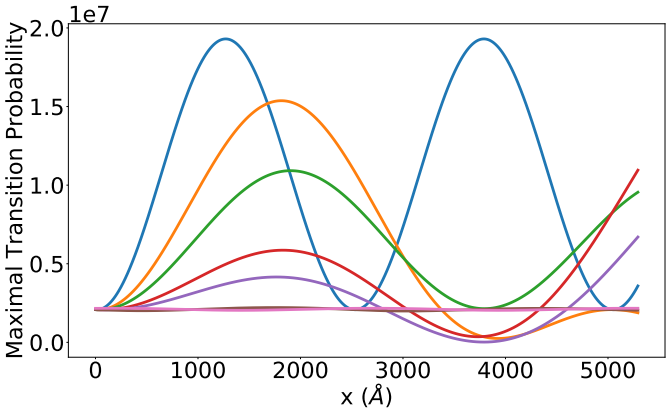

(a)

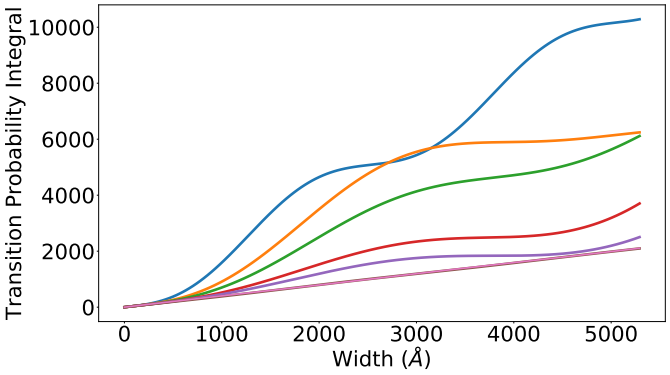

(b)

Figure 2.3: As fig. 2.2 for different ratios of the wave vectors of EFPW, k, and EFSW k'. Blue: $k' = k$, orange: $k' = k/2$, green: $k' = k/3$, red: $k' = k/6$, purple: $k' = k/10$, brown: $k' = k/1000$, pink: only EFPW. $k = 0.00126$ Å^{-1}

In a more complicated set up, the wave vectors of EFPW, k, and EFSW k' can differ. Figure 2.3 and fig. 2.4 show a variety of cases where k and k' are multiples of one another. The non-Beer-Lambert behavior is conserved. As a rule, the integrated transition probability is largest when the two values coincide. However, there is also a small region where the integrated transition probability is greater. It occurs for $k' = k/2$. Numerically, this is found in the region between 2400 Å and 3200 Å . These values are multiples of the reciprocal of k and k' which are 800 Å and 1600 Å and it is tempting to ascribe the augmented intensity to constructive interference of the two waves that are brought about by the "absorbing system". As the difference between the two values of k increases, the linear behaviour appears as an asymptotic limit.

2.2.2 Non-Linear Transitions

In general, the presence of an electric field can induce a variation in the dipole moment of the system, leading to various spectroscopic effects. Notable ones are two-photon absorption and Raman absorption/emission. These non-linear phenomena arise at large field intensities. The presence of both a propagating and standing

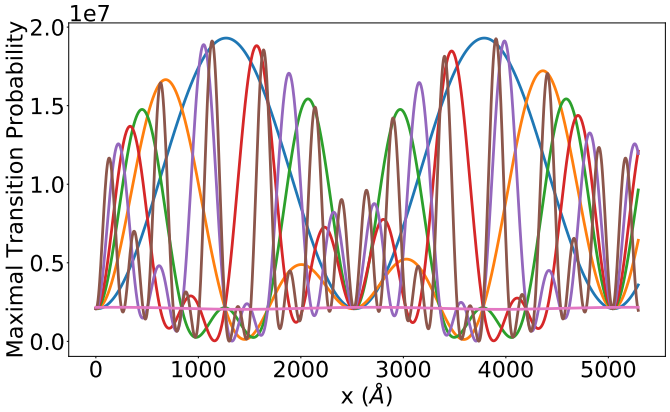

(a)

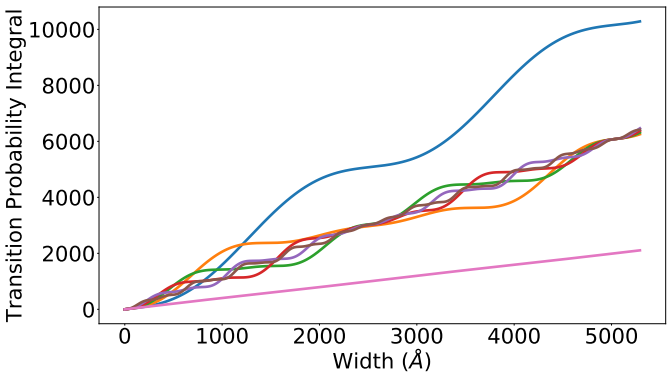

(b)

Figure 2.4: As fig. 2.2 for different ratios of the wave vectors of EFPW, k, and EFSW k'. Blue: $k' = k$, orange: $k' = 2k$, green: $k' = 3k$, red: $k' = 4k$, purple: $k' = 6k$, brown: $k' = 10k$, pink: only EFPW. $k = 0.00126$ Å^{-1}

wave wave increases the intensity, therefore non-linear phenomena may arise. Here, the discussion of the non-linear regime is qualitative and not specific to Raman or two-photon processes, following the approach presented in ref. [41].

To start, the induced dipole moment, μ_{ind}, is directly proportional to the electric field, and depends on the polarizability α, which in 3D is a 3x3 matrix.

$$\mu_{\text{ind}} = \alpha E \tag{2.23}$$

For simplicity, the discussion is restrained to the 1D case along the x-axis. The Hamiltonian becomes

$$\hat{H} = \hat{H}_{mol} + \hat{\alpha}_{xx} E_x^2 \tag{2.24}$$

so that first order time dependent perturbation theory, in the rotating wave approximation, yields

$$\begin{aligned} c_{\text{IF}} = \frac{A_x^2 \alpha_{\text{FI}}}{\hbar} \Bigg[& \frac{1 - e^{i(\omega_{\text{FI}} - 2\omega)t}}{\omega_{\text{FI}} - 2\omega} \left(e^{2ikx} + \frac{e^{-2ikx}}{4} + 1 \right) \\ & + \frac{1 - e^{i(\omega_{\text{FI}} + 2\omega)t}}{\omega_{\text{FI}} + 2\omega} \left(e^{-2ikx} + \frac{e^{2ikx}}{4} + 1 \right) \Bigg] \end{aligned} \tag{2.25}$$

where α_{FI} is the expectation value of the polarizability in the Ψ_F/Ψ_I basis and the remaining symbols follow the notation introduced in the previous section.

The same result is obtained if one considers a second order expansion with a set of virtual states [42], M, to give

$$P_{\text{IF}}^{(2)} = \left| c^{(2)} \right|^2 = \left| -\frac{1}{\hbar^2} \sum_M \int_0^t dt' \int_0^{t'} e^{i\omega_{\text{FM}} t'} e^{i\omega_{\text{MI}} t''} \hat{\mu}_{\text{FM}} \hat{\mu}_{\text{MI}} E(t') E(t'') dt'' \right|^2 \tag{2.26}$$

and treats the dipole moment integrals as constant.

In analogy with fig. 2.2, fig. 2.5 presents the simulation of the maximal transition probabilities and their integration for EFPW and EFSW. The maximal transition probability and its integral are numerically much smaller than in the case of the linear perturbation.

In fig. 2.5a the non-linear transition probability is displayed as a function of the position in the absorbing system. Maxima are reached for $\omega_{\text{FI}} = 2\omega$ and $\omega_{\text{FI}} = -2\omega$. In the case of the linear transitions, the form of the curve due to the combination of two fields is a linear combination of the individual contributions. This is not the case for the non-linear transitions. The black dotted line shows the difference between the blue curve obtained in the presence of the two fields and the sum of the individual EFPW and EFSW orange and green curves. Such difference does not coincide with any of the simpler processes.

The curve associated to the linear combination of the two electric fields presents a flat region and can be fitted by

$$\begin{aligned} & \int_0^l \left(e^{2ikx} + \frac{e^{-2ikx}}{4} + 1 \right) \left(e^{-2ikx} + \frac{e^{2ikx}}{4} + 1 \right) = \\ & = \frac{33kl + 20\sin(2kl) + 2\sin(4kl)}{16k} \end{aligned} \tag{2.27}$$

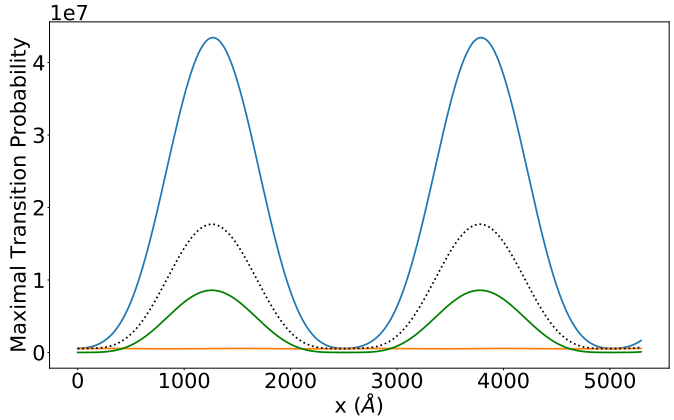

(a)

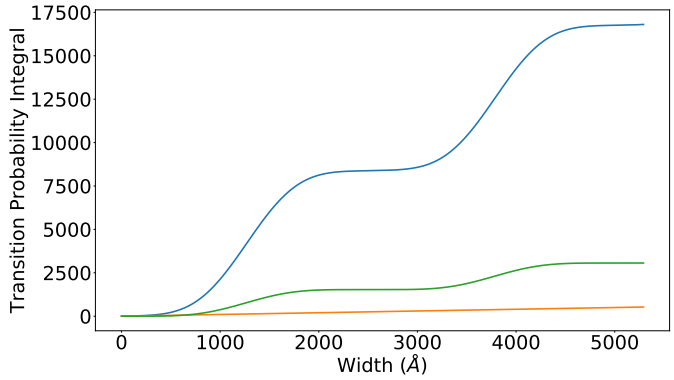

(b)

Figure 2.5: (a) Non normalized maximal transition probability in the non-linear regime as a function of the position in the absorbing sample. (b) Integrals of the curves of (a) calculated as a function of the width of the sample. Travelling wave (orange line), standing wave (green line) and the linear combinations of the two (blue line).The black dotted line is the difference between the blue curve and the sum of the orange and green curves. Parameters are $\omega = 20000$ cm^{-1}, $k = 0.00126$ Å^{-1}, $t = 70$ fs, $A_x^2 \alpha_{\mathrm{FI}}/\hbar = 1$ cm^{-1}

2.3 Towards Standing Wave Experiments

Despite the conceptual simplicity and their usefulness for the investigation of real samples, experiments with well-defined standing waves-without a reflecting mirror-could be non-trivial. On the other hand, the linear combination of electric fields used here may make it easier. To this end, fig. 2.6 sketches an experimental apparatus that generates a standing wave from a travelling wave generator, i.e. laser.

Using the standing wave approximation it is possible to consider the spatial variables of the electric fields as constants phase factors, this approximation is employed for simplicity. An incident electric field is of the form

$$E = 2A\cos(\omega t) \tag{2.28}$$

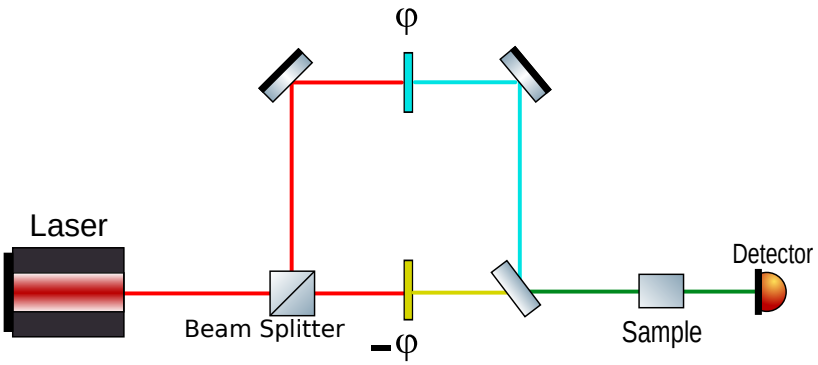

Figure 2.6: Sketch of an experimental apparatus that generates a standing wave (in green).

In fig. 2.6 the incident field (eq. (2.28)) passes through a dielectric beam splitter, then to one beam is applied a phase factor of $+\phi$ and to the other beam is applied a phase factor of $-\phi$. Then the two beams reach a semi-reflecting mirror, in this way the two beams overlap and the total electric field becomes the sum of the electric fields associated to the two beams. Then the standing wave may interact with a sample and reach the detector. Using this experimental apparatus and starting from the electric field of eq. (2.28) the standing wave obtained is of the form

$$E = 2\sqrt{2}A\cos(\phi)\cos(\omega t) \tag{2.29}$$

Then this simple apparatus can be used with a travelling wave generator to construct the linear combination of electric fields that were discussed in this work and to test the theoretical results reported here.

2.4 Remarks

This chapter explored the influence of EFSW on absorption spectra using time-dependent perturbation theory within the framework of semiclassical light-matter

interaction. The proposed framework allows the deviations from the Beer-Lambert law due to the EFSW to arise naturally. The effects of the EFSW can be tuned modifying the sample width or moving the sample. The trends predicted are in agreement with the experimental findings.

Initially, attention was directed toward linear transitions, founding a dependence of absorbance on the distance between the absorbing system and the reflective plate. The integral of transition probability deviates from the linearity predicted by the Beer-Lambert law. The effects of EFSW are minimized at the nodes of the standing wave, as expected. Varied effects can arise from the difference in wavevectors between standing and propagating waves, with absorption approaching Beer-Lambert behavior as the more the wavevectors differ. The models based on the wave optics also predicts a shift of the position of the peaks that is not present here. The origin of the shifts is still debated [29]. Experimentally, it was observed that IR spectra recorded in transflection mode exhibited an upward shift of 9 cm^{-1} of the amide I band (to 1667 cm^{-1}) in comparison to the one recorded in transmission (1658 cm^{-1})[5]. Further work will have to include interference effects that are thought to cause the shift of the position of the peaks.

The approximation employed seems to be adequate to describe the artifacts to the EFSW, therefore the investigation has been extended to the non-linear regime, simulating the transition probability and its integral. In such regime, the transition probability due to the combination of travelling and standing wave differs from that due to the standing wave and there are regions where the integrated probability of transition does not grow inside the sample.

References

[1] P.W. Atkins and R.S. Friedman. *Molecular Quantum Mechanics*. Oxford University Press, Oxford, 2011.

[2] Krzysztof B. Beć, Justyna Grabska, and Christian W. Huck. "Biomolecular and bioanalytical applications of infrared spectroscopy – A review". In: *Anal. Chim. Acta* 1133 (2020), pp. 150–177. ISSN: 0003-2670. DOI: https://doi.org/10.1016/j.aca.2020.04.015. URL: https://www.sciencedirect.com/science/article/pii/S0003267020304062.

[3] Imali A. Mudunkotuwa, Alaa Al Minshid, and Vicki H. Grassian. "ATR-FTIR spectroscopy as a tool to probe surface adsorption on nanoparticles at the liquid–solid interface in environmentally and biologically relevant media". In: *Analyst* 139 (5 2014), pp. 870–881. DOI: 10.1039/C3AN01684F. URL: http://dx.doi.org/10.1039/C3AN01684F.

[4] Jitraporn Vongsvivut et al. "Synchrotron macro ATR-FTIR microspectroscopy for high-resolution chemical mapping of single cells". In: *Analyst* 144 (10 2019), pp. 3226–3238. DOI: 10.1039/C8AN01543K. URL: http://dx.doi.org/10.1039/C8AN01543K.

[5] Emilia Staniszewska-Slezak et al. "Transmission versus transflection mode in FTIR analysis of blood plasma: is the electric field standing wave effect the only reason for observed spectral distortions?" In: *Analyst* 140 (7 2015), pp. 2412–2421. DOI: 10.1039/C4AN01842G. URL: http://dx.doi.org/10.1039/C4AN01842G.

[6] Guan-Lin Liu and Sergei G. Kazarian. "Recent advances and applications to cultural heritage using ATR-FTIR spectroscopy and ATR-FTIR spectroscopic imaging". In: *Analyst* 147 (9 2022), pp. 1777–1797. DOI: 10.1039/D2AN00005A. URL: http://dx.doi.org/10.1039/D2AN00005A.

[7] Stijn Legrand et al. "Macroscopic Fourier transform infrared scanning in reflection mode (MA-rFTIR), a new tool for chemical imaging of cultural heritage artefacts in the mid-infrared range". In: *Analyst* 139 (10 2014), pp. 2489–2498. DOI: 10.1039/C3AN02094K. URL: http://dx.doi.org/10.1039/C3AN02094K.

[8] G. Vaggelli and R. Cossio. "μ-XRF analysis of glasses: a non-destructive utility for cultural heritage applications". In: *Analyst* 137 (3 2012), pp. 662–667. DOI: 10.1039/C1AN15518K. URL: http://dx.doi.org/10.1039/C1AN15518K.

[9] Vitalijs Zubkovs et al. "Single vs. two-photon microscopy for label free intrinsic tissue studies in the UV light region". In: *Analyst* 139 (11 2014), pp. 2663–2667. DOI: 10.1039/C4AN00203B. URL: http://dx.doi.org/10.1039/C4AN00203B.

[10] Rachael Smith, Karen L. Wright, and Lorna Ashton. "Raman spectroscopy: an evolving technique for live cell studies". In: *Analyst* 141 (12 2016), pp. 3590–3600. DOI: 10.1039/C6AN00152A. URL: http://dx.doi.org/10.1039/C6AN00152A.

[11] Grace M. Sarabia and Bhavya Sharma. "Non-destructive raman spectroscopic determination of freshwater mollusk composition, growth, and damage repair". In: *Analyst* 146 (20 2021), pp. 6288–6296. DOI: 10.1039/D1AN01088C. URL: http://dx.doi.org/10.1039/D1AN01088C.

[12] Elena Possenti et al. "What's underneath? A non-destructive depth profile of painted stratigraphies by synchrotron grazing incidence X-ray diffraction". In: *Analyst* 143 (18 2018), pp. 4290–4297. DOI: 10.1039/C8AN00901E. URL: http://dx.doi.org/10.1039/C8AN00901E.

[13] Ruru Chen et al. "Proteomics and Immunology Provide Insight into the Degradation Mechanism of Historic and Artificially Aged Silk". In: *Analytical Chemistry* 92.3 (2020), pp. 2435–2442. DOI: 10.1021/acs.analchem.9b03616. URL: https://doi.org/10.1021/acs.analchem.9b03616.

[14] Shengjie Ling et al. "Synchrotron FTIR Microspectroscopy of Single Natural Silk Fibers". In: *Biomacromolecules* 12.9 (2011), pp. 3344–3349. DOI: 10.1021/bm2006032. URL: https://doi.org/10.1021/bm2006032.

[15] Gerrit Renner et al. "Robust Automatic Identification of Microplastics in Environmental Samples Using FTIR Microscopy". In: *Anal. Chem.* 91.15 (2019), pp. 9656–9664. DOI: 10.1021/acs.analchem.9b01095. URL: https://doi.org/10.1021/acs.analchem.9b01095.

[16] Camilo L. M. Morais et al. "Tutorial: multivariate classification for vibrational spectroscopy in biological samples". en. In: *Nat Protoc* 15.7 (July 2020), pp. 2143–2162. ISSN: 1750-2799. DOI: 10.1038/s41596-020-0322-8. URL: https://www.nature.com/articles/s41596-020-0322-8.

[17] Stefan Schütz and Remco Sprangers. "Methyl TROSY spectroscopy: A versatile NMR approach to study challenging biological systems". In: *Progress in Nuclear Magnetic Resonance Spectroscopy* 116 (2020), pp. 56–84. ISSN: 0079-6565. DOI: https://doi.org/10.1016/j.pnmrs.2019.09.004. URL: https://www.sciencedirect.com/science/article/pii/S0079656519300470.

[18] Giles Blaney et al. "Broadband absorption spectroscopy of heterogeneous biological tissue". In: *Appl. Opt.* 60.25 (2021), pp. 7552–7562. DOI: 10.1364/AO.431013. URL: https://opg.optica.org/ao/abstract.cfm?URI=ao-60-25-7552.

[19] P.R. Griffiths, J.A. De Haseth, and J.D. Winefordner. *Fourier Transform Infrared Spectrometry*. Chemical Analysis: A Series of Monographs on Analytical Chemistry and Its Applications. New York: Wiley, 2007. ISBN: 9780470106297.

[20] Joe Lee. "On the non-existence of the so-called "electric field standing wave effect" in transflection FTIR spectra". In: *Vibrational Spectroscopy* 90 (2017), pp. 104–111. ISSN: 0924-2031. DOI: https://doi.org/10.1016/j.vibspec.2017.03.007. URL: https://www.sciencedirect.com/science/article/pii/S0924203116302880.

[21] Melissa Romeo and Max Diem. "Correction of dispersive line shape artifact observed in diffuse reflection infrared spectroscopy and absorption/reflection (transflection) infrared micro-spectroscopy". In: *Vibrational Spectroscopy* 38.1 (2005), pp. 129–132. ISSN: 0924-2031. DOI: https://doi.org/10.1016/j.vibspec.2005.04.003. URL: https://www.sciencedirect.com/science/article/pii/S0924203105000640.

[22] Heather Brooke et al. "A Study of Electric Field Standing Waves on Reflection Microspectroscopy of Polystyrene Particles". In: *Appl. Spectr.* 63.11 (2009), pp. 1293–1302. DOI: 10.1366/000370209789806902. URL: https://doi.org/10.1366/000370209789806902.

[23] Jacob Filik et al. "Electric field standing wave artefacts in FTIR microspectroscopy of biological materials". In: *Analyst* 137 (4 2012), pp. 853–861. DOI: 10.1039/C2AN15995C. URL: http://dx.doi.org/10.1039/C2AN15995C.

[24] Josée Maurais and Patrick Ayotte. "Tailoring Electric Field Standing Waves in Reflection–Absorption Infrared Spectroscopy to Enhance Absorbance in Buried Molecular Layers". In: *J. Phys. Chem. C* 124.31 (2020), pp. 17158–17164. DOI: 10.1021/acs.jpcc.0c05309. URL: https://doi.org/10.1021/acs.jpcc.0c05309.

[25] Paul Bassan et al. "Reflection contributions to the dispersion artefact in FTIR spectra of single biological cells". In: *Analyst* 134 (6 2009), pp. 1171–1175. DOI: 10.1039/B821349F. URL: http://dx.doi.org/10.1039/B821349F.

[26] Paul Bassan et al. "The inherent problem of transflection-mode infrared spectroscopic microscopy and the ramifications for biomedical single point and imaging applications". In: *Analyst* 138 (1 2013), pp. 144–157. DOI: 10.1039/C2AN36090J. URL: http://dx.doi.org/10.1039/C2AN36090J.

[27] Joe Lee et al. "Optical artefacts in transflection mode FTIR microspectroscopic images of single cells on a biological support: the effect of backscattering into collection optics". In: *Analyst* 132 (8 2007), pp. 750–755. DOI: 10.1039/B702064C. URL: http://dx.doi.org/10.1039/B702064C.

[28] Thomas G. Mayerhöfer, Susanne Pahlow, and Jürgen Popp. "The Bouguer-Beer-Lambert Law: Shining Light on the Obscure". In: *ChemPhysChem* 21.18 (2020), pp. 2029–2046. DOI: https://doi.org/10.1002/cphc.202000464. URL: https://chemistry-europe.onlinelibrary.wiley.com/doi/abs/10.1002/cphc.202000464.

[29] Thomas G. Mayerhöfer and Jürgen Popp. "The electric field standing wave effect in infrared transflection spectroscopy". In: *Spectrochimica Acta Part A: Molecular and Biomolecular Spectroscopy* 191 (2018), pp. 283–289. ISSN: 1386-1425. DOI: https://doi.org/10.1016/j.saa.2017.10.033. URL: https://www.sciencedirect.com/science/article/pii/S1386142517308314.

[30] Thomas G. Mayerhöfer, Harald Mutschke, and Jürgen Popp. "The Electric Field Standing Wave Effect in Infrared Transmission Spectroscopy". In: *ChemPhysChem* 18.20 (2017), pp. 2916–2923. DOI: https://doi.org/10.1002/cphc.201700688. URL: https://chemistry-europe.onlinelibrary.wiley.com/doi/abs/10.1002/cphc.201700688.

[31] Paul Bassan et al. "FTIR microscopy of biological cells and tissue: data analysis using resonant Mie scattering (RMieS) EMSC algorithm". In: *Analyst* 137 (6 2012), pp. 1370–1377. DOI: 10.1039/C2AN16088A. URL: http://dx.doi.org/10.1039/C2AN16088A.

[32] Keith R. Bambery, Bayden R. Wood, and Don McNaughton. "Resonant Mie scattering (RMieS) correction applied to FTIR images of biological tissue samples". In: *Analyst* 137 (1 2012), pp. 126–132. DOI: 10.1039/C1AN15628D. URL: http://dx.doi.org/10.1039/C1AN15628D.

[33] Paul Bassan et al. "FTIR microscopy of biological cells and tissue: data analysis using resonant Mie scattering (RMieS) EMSC algorithm". In: *Analyst* 137 (6 2012), pp. 1370–1377. DOI: 10.1039/C2AN16088A. URL: http://dx.doi.org/10.1039/C2AN16088A.

[34] Paul Bassan et al. "Resonant Mie scattering in infrared spectroscopy of biological materials – understanding the 'dispersion artefact'". In: *Analyst* 134 (8 2009), pp. 1586–1593. DOI: 10.1039/B904808A. URL: http://dx.doi.org/10.1039/B904808A.

[35] Paul Bassan et al. "Resonant Mie Scattering (RMieS) correction of infrared spectra from highly scattering biological samples". In: *Analyst* 135 (2 2010), pp. 268–277. DOI: 10.1039/B921056C. URL: http://dx.doi.org/10.1039/B921056C.

[36] Paul Bassan et al. "RMieS-EMSC correction for infrared spectra of biological cells: Extension using full Mie theory and GPU computing". In: *Journal of Biophotonics* 3.8-9 (2010), pp. 609–620. DOI: https://doi.org/10.1002/jbio.201000036. URL: https://onlinelibrary.wiley.com/doi/abs/10.1002/jbio.201000036.

[37] Anupama B. Kaul. "Two-dimensional layered materials: Structure, properties, and prospects for device applications". en. In: *Journal of Materials Research* 29.3 (Feb. 2014), pp. 348–361. ISSN: 2044-5326. DOI: 10.1557/jmr.2014.6. URL: https://doi.org/10.1557/jmr.2014.6.

[38] Bo Guo et al. "2D Layered Materials: Synthesis, Nonlinear Optical Properties, and Device Applications". In: *Laser Photonics Rev.* 13.12 (2019), p. 1800327. DOI: https://doi.org/10.1002/lpor.201800327. URL: https://onlinelibrary.wiley.com/doi/abs/10.1002/lpor.201800327.

[39] A.S. Davydov. *Quantum Mechanics*. A-W series in advanced physics. Pergamon Press, 1976. ISBN: 9780080204383.

[40] D.J. Griffiths. *Introduction to Quantum Mechanics*. Cambridge University Press, 2017. ISBN: 9781107179868.

[41] G. Herzberg. *Infrared and Raman Spectra of Polyatomic Molecules*. Molecular spectra and molecular structure. Van Nostrand, 1945.

[42] Dmitrij Rappoport, Sangwoo Shim, and Alán Aspuru-Guzik. "Simplified Sum-Over-States Approach for Predicting Resonance Raman Spectra. Application to Nucleic Acid Bases". In: *J. Phys. Chem. Lett.* 2.11 (2011). PMID: 26295418, pp. 1254–1260. DOI: 10.1021/jz200413g. URL: https://doi.org/10.1021/jz200413g.

Chapter 3

Electrostatic Catalysis

Following the path to the fully quantum description of light-matter interactions we stop for a not-so-short moment in the semiclassical region.

The two level system employed in chapter 2 is hardly useful when dealing with molecular movements, for which is needed an atomistic description of the molecule. Several phenomena have been studied under this approximation [1–6] and an area that particularly profits from the combination between an atomistic molecular description and a classical electric field is electrostatic catalysis.

Electrostatic catalysis is the promotion and control of chemical reactivity of molecular systems through the utilization of oriented external electrostatic fields (OEEFs). Since the 1980s computational chemists have been interested in controlling chemical reactions via external electric fields, it is shown by the pioneering investigations on S_N2 reactions, [7] Friedel-Crafts reactions, [8] Diels-Alder cycloadditions, [9] C-H hydroxylations [10] and activations, [11] and C=C epoxidations [10].

The experimental feasibility was confirmed in 2016 using a scanning tunnelling microscopy break-junction (STM-BJ) apparatus to alter the rate of a Diels-Alder reaction [12]. This breakthrough opened the way to a series of STM-BJ controlled chemical reactions. Experiments showed that OEEFs can accelerate the cleavage of alkoxyamine C-ON bonds, [13] two-step cascade reactions of a Diels-Alder addition followed by an aromatization process, [14] isomerization reactions of cumulenes, [15] scission of C-C bonds via electrophilic aromatic substitutions, [16] homolysis of O-O bonds in peroxyanhydrides [17] and acylation of amines [18]. Other experimental techniques that exhibit a greater potential for scalability in the utilization of OEEFs for controlling reactivity have been also reported [19–25].

Recent advancements in experimental techniques have spurred a wave of new computational investigations, as documented in a range of references (e.g., [26–47]), with a primary focus on predicting and comprehending the means by which chemical reactivity and selectivity can be influenced through the application of oriented external electric fields (OEEFs). Concurrently, recent experimental and computational research has furnished evidence highlighting the central role of electric fields in the catalytic action of enzymes[48–57].

Despite the collective effort there still are open problems: is it possible to define the *optimal* electric field for catalyzing a reaction? If so, is it computable?

Under the condition that the desired outcome of the electric field usage is solely the catalysis, it is possible to assume that the desired electric field is the one that completely removes the reaction barrier. Starting from this ansatz it has been developed and implemented a model that finds the electric field with the smallest amplitude able to remove completely the reaction barrier. It has been named the polarizable molecular electric dipole (PMED) model, since it takes into account also the effects due to the polarizability.

The activities and outcomes described in this chapter have been performed in the research group of Professor Josep Maria Bofill Villà, with the invaluable help of Prof. J. Ribas Ariño, Prof. I. Ribeiro Moreira, Dr. W. Quapp and Dr. G. Albareda. This chapter is devoted to the derivation of the model and its application to real chemical systems. Section 3.1 presents some elements of catastrophe theory, whose concepts are central in the development of the model, section 3.2 introduces the model in the context of current theoretical models of electrostatic catalysis and section 3.3 contains applications of the PMED model to chemical reactions and molecular isomerizations.

3.1 Elements of Catastrophe Theory

The PMED model has its mathematical roots in catastrophe theory, which is briefly introduced in this chapter. The seeds of catastrophe theory have been planted in the 1880s by Henri Poincaré while working on dynamical systems, they sprouted with the contributions of Aleksandr Michajlovič Lyapunov and Marston Morse and finally catastrophe theory bloomed with René Thom, which forged the expression "catastrophe theory" almost a century after the seminal contributions of Poincaré.[58]

Given the stature of the mathematicians involved it is clear that catastrophe theory is far from being trivial. Catastrophe theory is a topological (and qualitative) theory, therefore to fully grasp the profoundness of Thom's theorems it is required a certain level of intimacy with topology. However, in this chapter, only the material needed for the application of catastrophe theory to electrostatic catalysis will be introduced, for this purpose the tools of real analysis are sufficient. This introduction is mostly adapted from ref. [59].

3.1.1 Objects of Catastrophe Theory

What is catastrophe theory,exactly? It is the study of how the solutions of equations change varying the parameters.

As simple as it sounds, in the most general form it is a formidable problem. In principle the equations could be of the integro-differential kind, non-linear and with derivatives of arbitrary order. Consequently Thom simplified the problem focusing on gradient systems, that is a system of partial differential equations of the form

$$F_i = \frac{\mathrm{d}x_i}{\mathrm{d}t} + \frac{\partial V(x_j; c_\alpha)}{\partial x_i} \tag{3.1}$$

where x_i is one of the solutions (in general it has nothing to do with a single space variable), V is some potential function, c_α is one of the control parameters and t is one of the variables, usually time.

Since catastrophe theory is interested in the qualitative behaviour of the solutions it is useful to define the equilibrium points ($\frac{\mathrm{d}x_i}{\mathrm{d}t} = 0$) of gradient systems. It can be proven that the equilibria of gradient systems obey the following

$$\frac{\partial V(x_j; c_\alpha)}{\partial x_i} = 0 \tag{3.2}$$

The study of how the equilibria $x_j(c_\alpha)$ of $V(x_j; c_\alpha)$ change as the control parameters c_α change is the object of elementary catastrophe theory.

From now on the focus is on elementary catastrophe theory, which is sufficient for the purpose of this introduction. It is useful to begin with a simple classification of the points of the potential $V(x_j; c_\alpha)$:$\mathbb{R}^n \to \mathbb{R}$.

1. $\nabla V \neq 0$
   The majority of the points of the potential V are non-stationary points, however an import theorem can be stated. In the neighborhood of these point the implicit function theorem guarantees the existence of a smooth change of variables

$$\begin{aligned} y_1 &= y_1(x_1, x_2, ..., x_n) \\ y_2 &= y_2(x_1, x_2, ..., x_n) \\ &... \\ &... \\ &... \\ y_n &= y_n(x_1, x_2, ..., x_n) \end{aligned} \tag{3.3}$$

   such that the potential V can be written as

$$V = y_1 + \text{a constant} \tag{3.4}$$

   That is, the potential V can be expressed as a linear function in the neighborhood of a non-critical point after a smooth change of variables.

2. $\nabla V = 0$ and nonsingular Hessian
   In the neighborhood of equilibrium points the implicit function theorem (eq. (3.4)) does not hold and the potential cannot be expressed as a linear function. An extension has been provided by Morse, that describes the neighborhood of the now called Morse critical points, that is points in which $\nabla V = 0$ and the determinant of the Hessian matrix (V_{ij}) is non-zero. The Morse theorem states that there exists a smooth change of variables such as, in the neighborhood of a Morse critical point, the potential can be expressed as

$$V = \sum_{i=1}^{n} \lambda_i y_i^2 \tag{3.5}$$

   This result is similar to the implicit function theorem, it simply tells that the linear approximation around a Morse critical point is not sufficient, and the potential must be approximated with a quadratic expression

3. $\nabla V = 0$ and singular Hessian
   The extension of Morse theorem is one of the main results of catastrophe theory, in fact Thom proved an extension of the results of Morse in neighborhoods of non-Morse equilibrium points ($\nabla V = 0$, $\det(V_{ij}) = 0$). Assuming $V(x;c)$,$x \in \mathbb{R}^n$ and $c \in \mathbb{R}^k$ the potential can be modified by a smooth change of variables such as the potential is split in two parts, a Morse part and a non-Morse part.

$$V = Cat(l,k) + \sum_{j=l+1}^{n} \lambda_j y_j^2 \tag{3.6}$$

   where $Cat(l,k)$ is called a catastrophe function, or a catastrophe; l is the number of null eigenvalues of V_{ij} and k is the number of control parameters. Moreover Thom proved that the catastrophe function contains two distinct contributions

$$Cat(l,k) = CG(l) + Pert(k,l) \tag{3.7}$$

   where $CG(l)$ is called catastrophe germ and $Pert(k,l)$ is a Perturbation. For $l \leq 2$ and $k \leq 5$ it is possible to analytically compute the CG and $Pert$ functions.

Now that the essential elements of catastrophe theory have been introduced, it is time to clarify the reasoning behind its name. The motivation lies in how the potential changes around equilibrium points after a variation of the control parameters. To do see it is useful to make a Taylor series expansion of the potential function about the equilibrium point $(x^0;c^0)$.

$$\begin{aligned} V(x,c) = V(x^0;c^0) + (x-x^0)_i V_i + (c-c^0)_\alpha V_\alpha \\ \frac{1}{2}(x-x^0)_i(x-x^0)_j V_{ij} + (x-x^0)_i(c-c^0)_\alpha V_{i\alpha} + \\ + \frac{1}{2}(c-c^0)_\alpha(c-c^0)_\beta V_{\alpha\beta} + \mathcal{O}(3) \end{aligned} \tag{3.8}$$

where all the derivatives are evaluated at $(x^0;c^0)$. $(x^0;c^0)$ is an equilibrium point, so V_i is zero. Now it is introduced a small variation of the control parameter, namely $c = c^0 + \delta c^0$ and look for the equilibrium points of $V(x;c^0+\delta c^0)$.

$$\frac{\partial V}{\partial x_i} = V_{ij}\delta x_j^0 + V_{i\alpha}\delta c_\alpha^0 + \mathcal{O}(2) = 0 \tag{3.9}$$

To understand how the equilibrium point moves as the parameters change it is convenient to rephrase eq. (3.9) isolating δx_j^0.

$$\delta x_j^0 = -(V^{-1})_{ij} V_{i\alpha}\delta c_\alpha^0 \tag{3.10}$$

or

$$\frac{\partial x_j^0}{\partial c_\alpha^0} = -(V^{-1})_{ij} V_{i\alpha} \tag{3.11}$$

It is clear that the Hessian must be nonsingular. Lastly the change of the potential function V due to a change of the control parameters can be computed substituting eq. (3.11) into eq. (3.8).

$$V(x^0+\delta x; c^0+\delta c) = V(x^0;c^0) + \delta^{(1)}V + \delta^{(2)}V + ... \tag{3.12}$$

$$\delta^{(1)}V = V_\alpha \delta c_\alpha \tag{3.13}$$

$$\delta^{(2)}V = \frac{1}{2}\delta c_\alpha \left[V_{\alpha\beta} - V_{\alpha i}(V)^{-1}_{ij} V_{j\beta}\right] \delta c_\beta \tag{3.14}$$

Equation (3.11) tells how the location of equilibrium points changes under small variations of the control parameters, eq. (3.12) tells how the potential function value in the equilibrium points changes under the same variation of the control parameters. The message of this derivation is that small changes of the control parameters produce only small changes in the position of the equilibrium points, as in a linear response regime. Moreover the same small change of the control parameters produces a small variation of the potential.

However, these important results do not hold in the neighborhood of a non-Morse equilibrium point. That is, in the neighborhood of a non-Morse critical point the Hessian is not invertible and a small change in the control parameters may produce a great variation of the location of the equilibrium point and of the potential function value. This is the reason of catastrophe theory: around non-Morse critical points a small variation of the parameters produces a large effect, a catastrophe. The effect of this small change of parameters is enclosed in the catastrophe function defined in eqs. (3.6) and (3.7), since the Morse part of the potential follows the linear response.

The consequence of this is (for the reader) the most important result obtained from catastrophe theory.

If $V(x;c)$ has at least a non-Morse critical point at (x^0, c^0) then at this point eq. (3.11) is not valid because the Hessian is not invertible. Therefore as $c \to c^0$ two isolated equilibrium points coalesce into one degenerate equilibrium point, located at $x = x^0$. This leads to a topological change of the function. It can be shown that the catastrophe function eq. (3.6) is the one that governs the topology of the potential, since the remaining quadratic part has no qualitative new properties, more precisely qualitative changes of the topology arise only through the perturbation of the catastrophe germ (eq. (3.7)).

This information is extremely appealing and has a two-fold consequence. I) If there is some information on the catastrophe point it is immediate to know how to modify the potential in order to isolate or remove the critical points, II) In order to make two isolated critical points coalesce it is sufficient to find a point in between them that could become a non-Morse equilibrium point, then Thom's theorem gives the certainty that the two nearest equilibrium points coalesce into one, creating a flat region.

Point II is the cornerstone of the application of catastrophe theory to electrostatic catalysis. It is possible to apply the theory to a potential energy surface making a minimum and a transition state coalesce, de facto removing the potential energy barrier.

In section 3.1.2 it is reported a simple example, in which the application of the aforementioned concepts leads to the formation and removal of equilibrium points.

3.1.2 A simple example

Consider a general 1-parameter family of potentials $V(x_1, x_2, x_3, ..., x_n; c)$, it is reasonable to expect the existence of a function with a non-Morse equilibrium point.

Around the non-Morse point the potential can be expressed according eq. (3.6). The form of the catastrophe function can be analytically determined and is

$$Cat(x;a) = \frac{1}{3}x^3 + ax \tag{3.15}$$

It is sufficient to focus on the catastrophe function to determine the topology of the potential function V upon variations of the a parameter, since the quadratic Morse part does not change its qualitative behaviour under a perturbation (eq. (3.11)).

It is immediate to locate the equilibrium points of $Cat(x;a)$:

$$\begin{aligned} \frac{\mathrm{d}Cat(x;a)}{\mathrm{d}x} &= 0 \\ x^2 + a &= 0 \end{aligned} \tag{3.16}$$

$$\begin{aligned} \frac{\mathrm{d}^2Cat(x;a)}{\mathrm{d}x^2} &= 0 \\ 2x &= 0 \end{aligned} \tag{3.17}$$

For $a > 0$ the catastrophe function has no equilibrium points, for $a < 0$ the catastrophe function has two equilibrium points (one maximum and one minimum), for $a = 0$ the catastrophe function has one non-Morse equilibrium point. Figure 3.1 shows a representation of the catastrophe function.

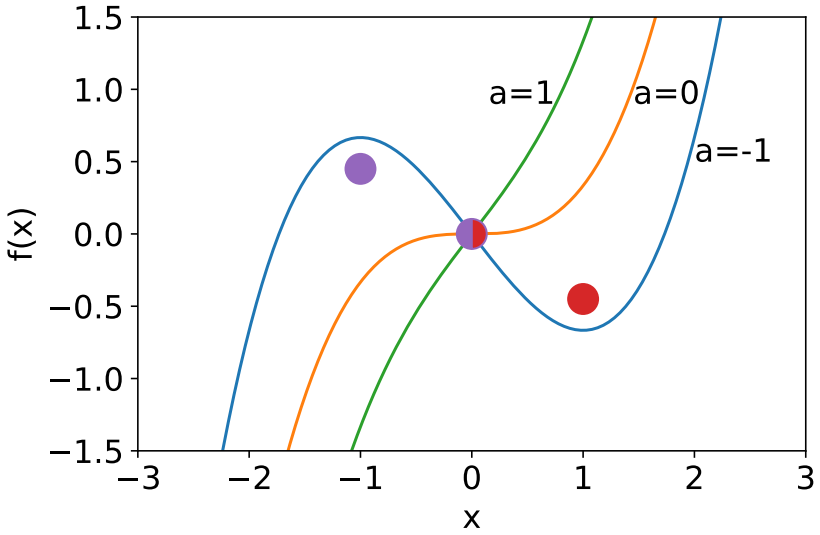

Figure 3.1: Plots of $Cat(x;a) = \frac{1}{3}x^3 + ax$ for $a = -1$, $a = 0$ and $a = 1$. All the functions with $a > 0$ have the same topology, that is zero equilibrium points. All the functions with $a < 0$ have the same topology as well, with two equilibrium points. The two families are separated by $a = 0$ in which there is a non-Morse equilibrium point. The red and purple dots represent the equilibrium points of the function, they coalesce into a red-purple dot when $a = 0$

This simple example showcases the power of catastrophe theory: even if the form of the potential V is complicated, knowing that there is just one control parameter is sufficient to draw simple conclusions on the nature and the number

of the equilibrium points. Figure 3.1 shows how two isolated equilibrium points, marked by a red and purple dot, coalesce into a degenerate equilibrium point as $a \to 0$.

The same reasoning can be readily applied backwards: catastrophe theory furnishes a set of rules to let two equilibrium points coalesce, generating a non-Morse equilibrium point and a flat region in the neighborhood of that point.

This idea is then applied to electrostatic catalysis. In fig. 3.1 the function computed for $a = -1$ could be a rough approximation of the section of a potential energy surface, in between the reactants (red dot) and the transition state (purple dot). Catastrophe theory can be used to let the reactants coalesce into one point, removing the energy barrier. Importantly from catastrophe theory it is assured that, after the coalescence of the equilibrium points, the surrounding region will be flat, avoiding the rising of unexpected maxima or minima.

The application of these concepts to electrostatic catalysis will be the object of section 3.2.

3.2 Introducing a New Model

In section 3.1 the core concepts of catastrophe theory have been introduced along with a brief outline about how these can be applied to electrostatic catalysis. Roughly speaking it is necessary to let two stationary points of the Potential Energy Surface (PES) coalesce into one, removing the energy barrier. The way to do so is to introduce a non-Morse equilibrium point, that is a point in which the gradient of the PES is zero and in which the determinant of the Hessian is zero. In this context, the way to introduce a non-Morse stationary point is via an external electric field.

Since this approach to electrostatic catalysis is undoubtedly exotic, in section 3.2.1 the most popular computational approaches to electrostatic catalysis are summarized and in section 3.2.2 the PMED model is introduced.

3.2.1 Current Theoretical Approaches

The majority of the computational methods for electrostatic catalysis rely on the dipole-field interaction, neglecting the polarizability contributions. The energy of the reactants can be written as

$$V_R = V_R^0 - E \cdot d_R \tag{3.18}$$

where V_R^0 is the energy of the reactants without the external field, E is the electric field vector and d_R is the molecular dipole moment vector in the geometry of the reactants. The same equation holds for the transition state

$$V_{TS} = V_{TS}^0 - E \cdot d_{TS} \tag{3.19}$$

From this equations the variation to the reaction barrier induced by the field is

$$\Delta B = E \cdot (d_{TS} - d_R) \tag{3.20}$$

The largest barrier variation is achieved when the electric field E is aligned with the $(d_{TS} - d_R)$ vector. This simple quantitative criterion has been used to determine the direction of the field. There are also qualitative procedures to determine the direction of the field, based on chemical intuition, e.g: the field is along the direction of a bond that should be broken/formed or the field is in a direction that solely stabilizes the transition state [26].

As it stands, this approach does not consider the second order contributions due to the polarizability and, importantly, it implicitly assumes that the reactants and transition state geometry is not distorted by the presence of the field. Consequently, this approximation is exclusively valid in scenarios characterized by low field strength. It is crucial to acknowledge that higher field strengths lead to significant induced dipoles and substantial geometric alterations, as documented in previous studies [9, 32]. Therefore, it is important to establish theoretical models that predict the most suitable field orientation while accounting for both polarizability and geometric perturbations.

3.2.2 Derivation of the PMED Model

The polarizable molecular electric dipole (PMED) model aims at overcoming the limitations of the first order dipolar approximations (eqs. (3.18) and (3.19)), proposing a procedure to determine the smallest possible electric field able to perfectly catalyze a chemical reaction, that is to completely erase the energy barrier.

This determination relies upon the identification of a specific point within the PES denoted as the "optimal barrier breakdown point" or, alternatively, the "optimal bond breaking point" (oBBP). The oBBP is nothing more than the non-Morse equilibrium point described in section 3.1.

Suppose that the reaction undergoes under the effect of the optimal Oriented External Electric Field (oOEEF). This results in a continuous deformation of the original PES. Initially, with a weak field, the reactants undergo distortion, bringing their nuclear configuration closer to that of the transition state (TS). In turn, the TS experiences distortion, aligning its nuclear configuration more closely with that of the reactants. As the field strength increases, both reactants and TS become increasingly distorted, and their configurations approach convergence. At a specific field strength determined by the oOEEF, these configurations merge. The precise point in the perturbed PES where the TS and reaction configurations coalesce under the influence of the oOEEF is the the oBBP. This is the same phenomenon predicted by catastrophe theory, which describes the coalescence of two equilibrium points (see fig. 3.1). The oOEEF is the external electric field with minimal amplitude able to induce the formation of the (optimal) BBP.

Now the derivation of the necessary and sufficient conditions for the location of the oBBP and the quantification of the oOEEF is reported.

The starting point of the model is the description of the PES under and OEEF given by $\mathbf{e} = (\epsilon_x, \epsilon_y, \epsilon_z) = E\mathbf{e}_n$ (with modulus E and normalized direction $\mathbf{e}_n$). This is done referring to the polarizable molecular electric dipole (PMED) ansatz[60] as

$$V_{\mathbf{e}_n}(\mathbf{x}, E) = V(\mathbf{x}) + P_{\mathbf{e}_n}(\mathbf{x}, E) = V(\mathbf{x}) - E\mathbf{e}_n^T\{\mathbf{d}(\mathbf{x}) + 1/2\mathbf{A}(\mathbf{x})\mathbf{e}_n E\} \tag{3.21}$$

where $V(\mathbf{x})$ is the original PES, $P_{\mathbf{e}_n}(\mathbf{x}, E)$ is the (electrostatic) perturbation energy, $\mathbf{d}(\mathbf{x})$ is the electric dipole moment vector, $\mathbf{x}^T = (x_1, y_1, z_1, \ldots, x_M, y_M, z_M)$ is the vector of the Cartesian coordinates of all M atoms of the system, $\mathbf{e}_n^T = (e_x, e_y, e_z)$ is the three-dimensional normalized field direction vector of the applied OEEF and $\mathbf{A}(\mathbf{x})$ is the 3x3 electric polarizability tensor, its elements are denoted as $a_{i,j}(\mathbf{x})$.

It is assumed that $V(\mathbf{x})$, $d_i(\mathbf{x})$ and $a_{i,j}(\mathbf{x})$ have continuous second derivatives with respect to $\mathbf{x}$.

Since, under the effect of the oOEEF, the oBBP is an equilibrium point the equilibrium condition is

$$\begin{aligned} \nabla_{\mathbf{x}} V_{\mathbf{e}_n}(\mathbf{x}, E) = \nabla_{\mathbf{x}} V(\mathbf{x}) + \nabla_{\mathbf{x}} P_{\mathbf{e}_n}(\mathbf{x}, E) = \\ \nabla_{\mathbf{x}} V(\mathbf{x}) - \{[\nabla_{\mathbf{x}} \mathbf{d}^T(\mathbf{x})] + 1/2E[\nabla_{\mathbf{x}}[\mathbf{A}(\mathbf{x})\mathbf{e}_n]^T]\}\mathbf{e}_n E = \mathbf{0} \end{aligned} \tag{3.22}$$

To simplify eq. (3.22) it is useful to define the vectors

$$\mathbf{h}_{\mathbf{e}_n}(\mathbf{x}) = [\nabla_{\mathbf{x}} \mathbf{d}^T(\mathbf{x})]\mathbf{e}_n = \sum_{i=(x,y,z)} e_i(\nabla_{\mathbf{x}} d_i(\mathbf{x})) \tag{3.23}$$

$$\mathbf{f}_{\mathbf{e}_n}(\mathbf{x}) = \mathbf{A}(\mathbf{x})\mathbf{e}_n = \sum_{i=(x,y,z)} e_i \mathbf{a}_i(\mathbf{x}) \tag{3.24}$$

where $\mathbf{a}_i(\mathbf{x})$ is the i-column of the $\mathbf{A}(\mathbf{x})$ matrix, namely, $\mathbf{a}_i^T(\mathbf{x}) = (a_{x,i}(\mathbf{x}), a_{y,i}(\mathbf{x}), a_{z,i}(\mathbf{x}))$, and

$$\mathbf{p}_{\mathbf{e}_n}(\mathbf{x}) = [\nabla_{\mathbf{x}} \mathbf{f}_{\mathbf{e}_n}^T(\mathbf{x})]\mathbf{e}_n = \sum_{i=(x,y,z)} e_i(\nabla_{\mathbf{x}} f_{\mathbf{e}_n i}(\mathbf{x})) = \sum_{i=(x,y,z)} e_i \left(\sum_{j=(x,y,z)} e_j(\nabla_{\mathbf{x}} a_{i,j}(\mathbf{x})) \right) \tag{3.25}$$

being $f_{\mathbf{e}_n i}(\mathbf{x})$ the i component of the three-dimensional $\mathbf{f}_{\mathbf{e}_n}(\mathbf{x})$ vector and finally, $\mathbf{g}(\mathbf{x}) = \nabla_{\mathbf{x}} V(\mathbf{x})$. With these definitions eq. (3.22)) can be stated in a more compact form

$$\mathbf{g}(\mathbf{x}) - [\mathbf{h}_{\mathbf{e}_n}(\mathbf{x})E + 1/2\mathbf{p}_{\mathbf{e}_n}(\mathbf{x})E^2] = \mathbf{g}(\mathbf{x}) + \mathbf{m}_{\mathbf{e}_n}(\mathbf{x}, E) = \mathbf{0} \ . \tag{3.26}$$

To find the oBBP and the oEEF, one approach is to examine the evolution of stationary points under the influence of an EEF and, later, consider the optimality conditions. Using a normalized constant vector $\mathbf{e}_n$, it is possible to define the force displaced stationary point (FDSP) curve as the set of points $(\mathbf{x}, E)$ satisfying eq. (3.26). At each point $(\mathbf{x}(t), E(t))$ on this curve, where t is the parameter characterizing the curve, an effective PES $V_{\mathbf{e}_n}(\mathbf{x}, E(t))$ is generated, meeting the stationary condition in eq. (3.26). For each normalized $\mathbf{e}_n$-vector, the corresponding FDSP curve generates a sequence of $V_{\mathbf{e}_n}(\mathbf{x}, E)$ effective potentials. Each effective potential maintains its own fixed E, with the $\mathbf{x}$ coordinates serving as variables. Therefore, the set of coordinates $\mathbf{x}$ assumes the role of variables, while the intensity E acts as a parameter. It is interesting to note that the normalized vector $\mathbf{e}_n$ plays the role of the control axis. A point that satisfies eq. (3.26) and $\det[\mathbf{H}_{\mathbf{e}_n}(\mathbf{x}, E)] = 0$ is called Bond-Breaking Point (BBP). However, for the moment being, $\mathbf{e}_n$ is fixed and the BBP associated with an arbitrary $\mathbf{e}_n$ may be non-optimal.

It is possible to locate the BBP looking for the point on the FDSP curve in which $\det[\mathbf{H}_{\mathbf{e}_n}(\mathbf{x}, E)] = 0$. The application of the Implicit Function Theorem[61] to

the expression $d(\nabla_{\mathbf{x}} V_{\mathbf{e}_n}(\mathbf{x}, E))/dt = \mathbf{0}$ leads to a differential equation that defines the FDSP curve.[60]

$$\mathbf{H}_{\mathbf{e}_n}(\mathbf{x}, E)\left(\frac{d\mathbf{x}}{dt}\right) = \mathbf{r}_{\mathbf{e}_n}(\mathbf{x}, E)\left(\frac{dE}{dt}\right) . \tag{3.27}$$

In this expression, the $\mathbf{r}_{\mathbf{e}_n}(\mathbf{x}, E)$ vector is

$$\mathbf{r}_{\mathbf{e}_n}(\mathbf{x}, E) = \mathbf{h}_{\mathbf{e}_n}(\mathbf{x}) + E\mathbf{p}_{\mathbf{e}_n}(\mathbf{x}) , \tag{3.28}$$

The explicit form of the Hessian matrix reads

$$\mathbf{H}_{\mathbf{e}_n}(\mathbf{x}, E) = \mathbf{H}(\mathbf{x}) - \mathbf{F}_{\mathbf{e}_n}(\mathbf{x}, E) \tag{3.29}$$

being $\mathbf{H}(\mathbf{x}) = \nabla_{\mathbf{x}}\nabla_{\mathbf{x}}^T V(\mathbf{x})$ the Hessian matrix of the original PES, $V(\mathbf{x})$, and

$$\begin{aligned} \mathbf{F}_{\mathbf{e}_n}(\mathbf{x}, E) &= E\nabla_{\mathbf{x}}\mathbf{h}_{\mathbf{e}_n}^T(\mathbf{x}) + \frac{1}{2}E^2\nabla_{\mathbf{x}}\mathbf{p}_{\mathbf{e}_n}^T(\mathbf{x}) \\ &= E\sum_{i=(x,y,z)} e_i[(\nabla_{\mathbf{x}}\nabla_{\mathbf{x}}^T d_i(\mathbf{x})) + \frac{E}{2}(\nabla_{\mathbf{x}}\nabla_{\mathbf{x}}^T f_{\mathbf{e}_n i}(\mathbf{x}))] \\ &= \sum_{i=(x,y,z)} \epsilon_i \mathbf{M}_i(\mathbf{x}, \mathbf{e}) . \end{aligned} \tag{3.30}$$

Equation (3.30) has been derived using$-\mathbf{F}_{\mathbf{e}_n}(\mathbf{x}, E) = \nabla_{\mathbf{x}}\nabla_{\mathbf{x}}^T P_{\mathbf{e}_n}(\mathbf{x}, E)$ and eqs. (3.23) and (3.25). The specific form of $\nabla_{\mathbf{x}}\nabla_{\mathbf{x}}^T f_{\mathbf{e}_n i}(\mathbf{x})$ appearing in eq. (3.30) is

$$\nabla_{\mathbf{x}}\nabla_{\mathbf{x}}^T f_{\mathbf{e}_n i}(\mathbf{x}) = \sum_{j=(x,y,z)} e_j(\nabla_{\mathbf{x}}\nabla_{\mathbf{x}}^T a_{i,j}(\mathbf{x})) \quad i = x, y, z . \tag{3.31}$$

On the FDSP curve defined by eq. (3.27) there is one point is which $\det[\mathbf{H}_{\mathbf{e}_n}(\mathbf{x}, E)] = 0$, which is the *barrier breakdown or bond-breaking point* (BBP). The corresponding field intensity is labeled as E_{BBP}. This is equivalent to saying that an eigenvector of $\mathbf{H}_{\mathbf{e}_n}(\mathbf{x}, E)$ has null eigenvalue and, in this case, $d\mathbf{x}/dt$ is taken as normalized tangent vector [60]. Therefore the left-hand side of eq. (3.27) is zero, which leads to $\frac{dE}{dt} = 0$. The presence of a turning point of the E parameter at the BBP implies that the solution is optimal with respect to E.

Now that the optimality of the E parameter has been defined it is necessary to introduce the optimality condition on the $\mathbf{x}$ variables. To do so it is sufficient to examine the conditions defined above. In a (at the moment non optimal) BBP the following conditions are satisfied

$$\left.\frac{dE}{dt}\right|_{E=E_{BBP}} = 0 \tag{3.32a}$$

$$\mathbf{H}_{\mathbf{e}_n}(\mathbf{x}, E)\left(\frac{d\mathbf{x}}{dt}\right)\Bigg|_{\substack{\mathbf{x} = \mathbf{x}_{BBP} \\ E = E_{BBP}}} = \mathbf{0} . \tag{3.32b}$$

Substituting eq. (3.29) in eq. (3.32b), and then applying the resolution of identity and dividing by the tangent norm the result is

$$\begin{aligned}\left(\mathbf{I}-\frac{\dot{\mathbf{x}}\dot{\mathbf{x}}^T}{\dot{\mathbf{x}}^T\dot{\mathbf{x}}}\right)\left[\mathbf{H}(\mathbf{x}_{BBP})-\mathbf{F}_{\mathbf{e}_n}(\mathbf{x}_{BBP},E_{BBP})\right]\frac{\dot{\mathbf{x}}}{\sqrt{\dot{\mathbf{x}}^T\dot{\mathbf{x}}}}+\\ \left(\frac{\dot{\mathbf{x}}\dot{\mathbf{x}}^T}{\dot{\mathbf{x}}^T\dot{\mathbf{x}}}\right)\left[\mathbf{H}(\mathbf{x}_{BBP})-\mathbf{F}_{\mathbf{e}_n}(\mathbf{x}_{BBP},E_{BBP})\right]\frac{\dot{\mathbf{x}}}{\sqrt{\dot{\mathbf{x}}^T\dot{\mathbf{x}}}}=\mathbf{0}\end{aligned} \tag{3.33}$$

with $\dot{\mathbf{x}}=d\mathbf{x}/dt$. Equation (3.33) asserts that at the BBP, the tangent $\dot{\mathbf{x}}$ is an eigenvector of the effective Hessian, $\mathbf{H}_{\mathbf{e}_n}(\mathbf{x},E)$, as defined in eq. (3.29). Consequently, the two expectation values, namely, $\dot{\mathbf{x}}^T\mathbf{H}(\mathbf{x}_{BBP})\dot{\mathbf{x}}/(\dot{\mathbf{x}}^T\dot{\mathbf{x}})$, and $-\dot{\mathbf{x}}^T\mathbf{F}_{\mathbf{e}_n}(\mathbf{x}_{BBP},E_{BBP})\dot{\mathbf{x}}/(\dot{\mathbf{x}}^T\dot{\mathbf{x}})$, must be equal but opposite in sign at the BBP, $(\mathbf{x}_{BBP}^T,E_{BBP})$. This implies that $\dot{\mathbf{x}}^T\mathbf{H}_{\mathbf{e}_n}(\mathbf{x}_{BBP},E_{BBP})\dot{\mathbf{x}}/(\dot{\mathbf{x}}^T\dot{\mathbf{x}})=0$. The first and second derivatives of $V(\mathbf{x})$ and $P_{\mathbf{e}_n}(\mathbf{x},E)$ are, thus, equal but with opposite sign at the BBP with $E=E_{BBP}$. A point in which the first and second derivatives of two functions coincide is said a contact point of order two. At $\mathbf{x}=\mathbf{x}_{BBP}$ and $E=E_{BBP}$, $V(\mathbf{x})$ and $P_{\mathbf{e}_n}(\mathbf{x},E)$ have a contact point of order two. This property is central in the development of the model.

It is useful to notice that $\dot{\mathbf{x}}$ is equal to $\mathbf{g}(\mathbf{x})$ and $\mathbf{m}_{\mathbf{e}_n}(\mathbf{x},E)$ in the BBP. This follows from the fact that the BBP belongs to the FDSP curve and that since BBP is a point of a FDSP curve and eq. (3.26) should be true.

$$\frac{\dot{\mathbf{x}}}{\sqrt{\dot{\mathbf{x}}^T\dot{\mathbf{x}}}}=\frac{\mathbf{g}(\mathbf{x}_{BBP})}{\sqrt{\mathbf{g}^T(\mathbf{x}_{BBP})\mathbf{g}(\mathbf{x}_{BBP})}}=-\frac{\mathbf{m}_{\mathbf{e}_n}(\mathbf{x}_{BBP},E_{BBP})}{\sqrt{\mathbf{m}_{\mathbf{e}_n}^T(\mathbf{x}_{BBP},E_{BBP})\mathbf{m}_{\mathbf{e}_n}(\mathbf{x}_{BBP},E_{BBP})}} \tag{3.34}$$

This allows to partially drop the curve parameter and rewrite eq. (3.32)

$$\left.\frac{dE}{dt}\right|_{E=E_{BBP}}=0 \tag{3.35a}$$

$$\mathbf{H}_{\mathbf{e}_n}(\mathbf{x},E)\left(\frac{\mathbf{g}(\mathbf{x})}{\sqrt{\mathbf{g}^T(\mathbf{x})\mathbf{g}(\mathbf{x})}}\right)\Bigg|_{\begin{pmatrix}\mathbf{x} & =\mathbf{x}_{BBP}\\ E & =E_{BBP}\end{pmatrix}}=\mathbf{0}\qquad \mathbf{g}(\mathbf{x})\neq\mathbf{0}\ . \tag{3.35b}$$

In the same fashion of eq. (3.33), eq. (3.35) becomes

$$\mathbf{k}(\mathbf{x})=\left[\mathbf{I}-\frac{\mathbf{g}(\mathbf{x})\mathbf{g}^T(\mathbf{x})}{\mathbf{g}^T(\mathbf{x})\mathbf{g}(\mathbf{x})}\right]\mathbf{H}(\mathbf{x})\frac{\mathbf{g}(\mathbf{x})}{\sqrt{\mathbf{g}^T(\mathbf{x})\mathbf{g}(\mathbf{x})}}=\left[\mathbf{I}-\frac{\mathbf{g}(\mathbf{x})\mathbf{g}^T(\mathbf{x})}{\mathbf{g}^T(\mathbf{x})\mathbf{g}(\mathbf{x})}\right]\mathbf{F}_{\mathbf{e}_n}(\mathbf{x},E)\frac{\mathbf{g}(\mathbf{x})}{\sqrt{\mathbf{g}^T(\mathbf{x})\mathbf{g}(\mathbf{x})}}\ , \tag{3.36a}$$

$$\frac{\mathbf{g}(\mathbf{x})}{\sqrt{\mathbf{g}^T(\mathbf{x})\mathbf{g}(\mathbf{x})}}k(\mathbf{x})=\frac{\mathbf{g}(\mathbf{x})}{\sqrt{\mathbf{g}^T(\mathbf{x})\mathbf{g}(\mathbf{x})}}\frac{\mathbf{g}^T(\mathbf{x})\mathbf{H}(\mathbf{x})\mathbf{g}(\mathbf{x})}{\mathbf{g}^T(\mathbf{x})\mathbf{g}(\mathbf{x})}=\frac{\mathbf{g}(\mathbf{x})}{\sqrt{\mathbf{g}^T(\mathbf{x})\mathbf{g}(\mathbf{x})}}\frac{\mathbf{g}^T(\mathbf{x})\mathbf{F}_{\mathbf{e}_n}(\mathbf{x},E)\mathbf{g}(\mathbf{x})}{\mathbf{g}^T(\mathbf{x})\mathbf{g}(\mathbf{x})} \tag{3.36b}$$

where, $k(\mathbf{x})=\mathbf{g}^T(\mathbf{x})\mathbf{H}(\mathbf{x})\mathbf{g}(\mathbf{x})/(\mathbf{g}^T(\mathbf{x})\mathbf{g}(\mathbf{x}))=\mathbf{g}^T(\mathbf{x})\mathbf{F}_{\mathbf{e}_n}(\mathbf{x},E)\mathbf{g}(\mathbf{x})/(\mathbf{g}^T(\mathbf{x})\mathbf{g}(\mathbf{x}))$.

Combining eq. (3.33) and eq. (3.34) it follows that, in the BBP, $\mathbf{k}(\mathbf{x})=0$. Recalling that in the BBP $V(\mathbf{x})$ and $P_{\mathbf{e}_n}(\mathbf{x},E)$ have a contact point of order two it

follows that the two terms of eq. (3.36) must be independently zero, that is

$$\left[\mathbf{I} - \frac{\mathbf{g}(\mathbf{x})\mathbf{g}^T(\mathbf{x})}{\mathbf{g}^T(\mathbf{x})\mathbf{g}(\mathbf{x})}\right]\mathbf{H}(\mathbf{x})\frac{\mathbf{g}(\mathbf{x})}{\sqrt{\mathbf{g}^T(\mathbf{x})\mathbf{g}(\mathbf{x})}} = \mathbf{0} \tag{3.37a}$$

$$\left[\mathbf{I} - \frac{\mathbf{m}_{\mathbf{e}_n}(\mathbf{x},E)\mathbf{m}^T_{\mathbf{e}_n}(\mathbf{x},E)}{\mathbf{m}^T_{\mathbf{e}_n}(\mathbf{x},E)\mathbf{m}_{\mathbf{e}_n}(\mathbf{x},E)}\right]\mathbf{F}_{\mathbf{e}_n}(\mathbf{x},E)\frac{\mathbf{m}_{\mathbf{e}_n}(\mathbf{x},E)}{\sqrt{\mathbf{m}^T_{\mathbf{e}_n}(\mathbf{x},E)\mathbf{m}_{\mathbf{e}_n}(\mathbf{x},E)}} = \mathbf{0}\ , \tag{3.37b}$$

If eq. (3.37) is satisfied at $(\mathbf{x_{BBP}}, E_{BBP})$ then the BBP is a gradient extremal point of both the potential energy surface $(V(\mathbf{x}))$ and of the perturbing function $(P_{\mathbf{e}_n}(\mathbf{x},E))$.[62–72]

So, the BBP must be a point of the FDSP curve (eq. (3.26)) and a gradient extremal point for the unperturbed PES and for the perturbing function (eq. (3.37)).

It is of central importance that the BBP is a gradient extremal point, because these points are characterized by optimal properties.[66, 72] It has already been proven the optimality with respect to E, it necessary to prove the optimality of the field with respect to the coordinates $\mathbf{x}$, and this is where the gradient extremals are useful. The electric force applied to the unperturbed PES is simply $\mathbf{m}_{\mathbf{e}_n}(\mathbf{x},E)$ and, in order to be optimal, its norm should be as small as possible.

In the BBP the gradient extremal point satisfies the $\det[\mathbf{H}(\mathbf{x_{BBP}})] = 0$ condition (eq. (3.36a)) and it has been shown that in this point the square of the gradient norm, $\mathbf{g}^T(\mathbf{x_{BBP}})\mathbf{g}(\mathbf{x_{BBP}})$, is stationary with respect to all independent directions.[73]. Since in the BBP $\mathbf{g}(\mathbf{x_{BBP}}) = -\mathbf{m}_{\mathbf{e}_n}(\mathbf{x_{BBP}}, E_{BBP})$ and the same condition is satisfied also regarding $\mathbf{F}_{\mathbf{e}_n}(\mathbf{x_{BBP}}, E_{BBP})$ also the squared norm $\mathbf{m}^T_{\mathbf{e}_n}(\mathbf{x_{BBP}}, E_{BBP})\mathbf{m}_{\mathbf{e}_n}(\mathbf{x_{BBP}}, E_{BBP})$ is stationary.

This proves the existence of an optimal solution with respect to $\mathbf{x}$, in which the squared norm $\mathbf{m}^T_{\mathbf{e}_n}(\mathbf{x_{BBP}}, E_{BBP})\mathbf{m}_{\mathbf{e}_n}(\mathbf{x_{BBP}}, E_{BBP})$, and therefore the electrical force applied is the lowest one able to remove the barrier between reactants and transition state. The point in which all the aforementioned conditions are satisfied and the field amplitude is minimal is the *optimal* BBP and the corresponding field is the *optimal* OEEF. From now on the optimal OEEF is denoted $\mathbf{e}^* = E\mathbf{e}^*_n$.

Now that the only missing step is the actual location of the optimal solution.

3.2.3 Calculation of the Optimal External Electric Field

The necessary and sufficient conditions for the location of the optimal BBP and the optimal OEEF are eqs. (3.34) and (3.37). This section is devoted to the presentation of an algorithm able to find the optimal BBP and the optimal OEEF. The algorithm is implemented in the MANULS program [74] and the numerical details of the implementation are discussed in section 3.A.1. The algorithm can be conveniently summed up in points

1. *Location of* $\mathbf{x}_{oBBP}$
   The $\mathbf{x}_{oBBP}$ is the optimal BBP, the point that satisfies eq. (3.37), being a GE point with eigenvalue equal zero. The location of this point is based in finding the point $\mathbf{x}$ where the so-called $\sigma(\mathbf{x})$- function, $\sigma(\mathbf{x}) = \mathbf{g}^T(\mathbf{x})\mathbf{H}^2(\mathbf{x})\mathbf{g}(\mathbf{x})/(\mathbf{g}^T(\mathbf{x})\mathbf{g}(\mathbf{x}))$, has value zero. The $\sigma(\mathbf{x})$-function was presented in [75, 76]. As trivial as it may sound it is also important to check that

$\mathbf{g}(\mathbf{x}) \neq 0$, $\mathbf{H}(\mathbf{x})$ is not the zero matrix, and the dipoles and polarizabilities have definite first and second derivatives.

2. *The $\mathbf{x}_{oBBP}$ point belongs to the FDSP*
After the optimal BBP has been located it sufficient to impose the necessary and sufficient conditions described in section 3.2.2 in order to find the optimal OEEF. The optimal BBP must belong to the FDSP, that is the gradient of the perturbed PES must be zero. The condition is defined in eq. (3.26)), which can be multiplied from the left by the outer gradient projector to obtain

$$\left(\mathbf{I} - \frac{\mathbf{g}(\mathbf{x}_{oBBP})\mathbf{g}^T(\mathbf{x}_{oBBP})}{\mathbf{g}^T(\mathbf{x}_{oBBP})\mathbf{g}(\mathbf{x}_{oBBP})}\right)\mathbf{m}_{\mathbf{e}_n^*}(\mathbf{x}_{oBBP}, E_{oBBP}) = \mathbf{0} \ . \tag{3.38}$$

Using eqs. (3.25) and (3.28) and recalling that, $\mathbf{e} = E\mathbf{e}_n$, the $\mathbf{m}_{\mathbf{e}_n}(\mathbf{x}, E)$ vector at the optimal BBP is

$$\begin{aligned}\mathbf{m}_{\mathbf{e}_n^*}(\mathbf{x}_{oBBP}, E_{oBBP}) &= -\{[\nabla_{\mathbf{x}}\mathbf{d}^T(\mathbf{x}_{oBBP})] + E_{oBBP}/2[\nabla_{\mathbf{x}}\mathbf{f}^T_{\mathbf{e}_n^*}(\mathbf{x}_{oBBP})]\}\mathbf{e}^*_{oBBP} \\ &= -\mathbf{N}_{\mathbf{e}_n^*}(\mathbf{x}_{oBBP}, E_{oBBP})\mathbf{e}^*_{oBBP} \ .\end{aligned} \tag{3.39}$$

Substituting Eq. (3.39) into Eq. (3.38) and multiplying the resulting expression from the left by its transposed, one finds

$$\begin{aligned}&\mathbf{e}^{*T}_{oBBP}\mathbf{N}^T_{\mathbf{e}_n^*}(\mathbf{x}_{oBBP}, E_{oBBP})\left[\mathbf{I} - \frac{\mathbf{g}(\mathbf{x}_{oBBP})\mathbf{g}^T(\mathbf{x}_{oBBP})}{\mathbf{g}^T(\mathbf{x}_{oBBP})\mathbf{g}(\mathbf{x}_{oBBP})}\right]\mathbf{N}_{\mathbf{e}_n^*}(\mathbf{x}_{oBBP}, E_{oBBP})\mathbf{e}^*_{oBBP} = \\ &\mathbf{e}^{*T}_{oBBP}\mathbf{D}(\mathbf{x}_{oBBP}, \mathbf{e}^*_{oBBP})\mathbf{e}^*_{oBBP} = 0 \ .\end{aligned} \tag{3.40}$$

3. *The optimal BBP is a gradient extremal point of the original PES and of the perturbation potential*
The perturbation potential,$P_{\mathbf{e}_n}(\mathbf{x}, E)$, defined in eq. (3.21), depends on the direction, $\mathbf{e_n}$, and amplitude E, of the external electric field. The optimal BBP must be a gradient extremal point of both the unperturbed PES and the perturbation potential. This conditions are satisfied if eq. (3.36) is zero. A simple rewriting of eq. (3.36) leads to two conditions that must be simultaneously met

- $$\begin{aligned}&\frac{\mathbf{g}^T(\mathbf{x}_{oBBP})\mathbf{F}_{\mathbf{e}_n^*}(\mathbf{x}_{oBBP}, E_{oBBP})\mathbf{g}(\mathbf{x}_{oBBP})}{\mathbf{g}^T(\mathbf{x}_{oBBP})\mathbf{g}(\mathbf{x}_{oBBP})} = \\ &\sum_{i=x,y,z}\epsilon^{*o}_i\frac{\mathbf{g}^T(\mathbf{x}_{oBBP})\mathbf{M}_i(\mathbf{x}_{oBBP}, \mathbf{e}^*_{oBBP})\mathbf{g}(\mathbf{x}_{oBBP})}{\mathbf{g}^T(\mathbf{x}_{oBBP})\mathbf{g}(\mathbf{x}_{oBBP})} = \\ &\sum_{i=x,y,z}\epsilon^{*o}_i\frac{\mathbf{g}^T(\mathbf{x}_{oBBP})\mathbf{t}_i(\mathbf{x}_{oBBP}, \mathbf{e}^*_{oBBP})}{\sqrt{\mathbf{g}^T(\mathbf{x}_{oBBP})\mathbf{g}(\mathbf{x}_{oBBP})}} =: \\ &\sum_{i=x,y,z}\epsilon^{*o}_i z_i(\mathbf{x}_{oBBP}, \mathbf{e}^*_{oBBP}) = \\ &\mathbf{e}^{*T}_{oBBP}\mathbf{z}(\mathbf{x}_{oBBP}, \mathbf{e}^*_{oBBP}) = 0 \ .\end{aligned} \tag{3.41}$$

- $$\frac{\mathbf{g}^T(\mathbf{x}_{oBBP})\mathbf{F}^2_{\mathbf{e}^*_n}(\mathbf{x}_{oBBP}, E_{oBBP})\mathbf{g}(\mathbf{x}_{oBBP})}{\mathbf{g}^T(\mathbf{x}_{oBBP})\mathbf{g}(\mathbf{x}_{oBBP})} = \sum_{i=x,y,z}\sum_{j=x,y,z} \epsilon^{*o}_i \epsilon^{*o}_j \mathbf{t}^T_i(\mathbf{x}_{oBBP}, \mathbf{e}^*_{oBBP})\mathbf{t}_j(\mathbf{x}_{oBBP}, \mathbf{e}^*_{oBBP}) = \mathbf{e}^{*T}_{oBBP}\mathbf{T}(\mathbf{x}_{oBBP}, \mathbf{e}^*_{oBBP})\mathbf{e}^*_{oBBP} = 0\ . \tag{3.42}$$

The optimal external electric field, therefore, must be chosen such as eqs. (3.40) to (3.42) are satisfied.

For numerical reasons it is preferable to condense the three conditions into a single function, called f.

$$\begin{pmatrix} \mathbf{e}^{*T}\mathbf{D}(\mathbf{x}_{BBP}) \\ \mathbf{z}^T(\mathbf{x}_{BBP}) \\ \mathbf{e}^{*T}\mathbf{T}(\mathbf{x}_{BBP}) \end{pmatrix} \mathbf{e}^*_{BBP} = \begin{pmatrix} 0 \\ v \\ \mathbf{v}^T\mathbf{v} + v^2 \end{pmatrix} \tag{3.43}$$

where

$$v = \mathbf{g}^T(\mathbf{x}_{BBP})\mathbf{F}_{\mathbf{e}^*_n}(\mathbf{x}_{BBP}, E_{BBP})\mathbf{g}(\mathbf{x}_{BBP}) \tag{3.44}$$

and

$$\mathbf{v}^T\mathbf{v} + v^2 = \mathbf{g}^T(\mathbf{x}_{BBP})\mathbf{F}^2_{\mathbf{e}^*_n}(\mathbf{x}_{BBP}, E_{BBP})\mathbf{g}(\mathbf{x}_{BBP}) \tag{3.45}$$

Equation (3.43) can be rewritten as

$$\mathbf{B}(\mathbf{x}_{BBP})\mathbf{e}^*_{BBP} = \mathbf{b} \tag{3.46}$$

And, lastly, the f function is defined as

$$f(\mathbf{e}^*_{BBP}) = 1/2\mathbf{e}^*_{BBP}\mathbf{B}(\mathbf{x}_{BBP}, \mathbf{e}^*_{BBP})\mathbf{e}^*_{BBP} - \mathbf{b}^T\mathbf{B}(\mathbf{x}_{BBP}, \mathbf{e}^*_{BBP})\mathbf{e}^*_{BBP} + 1/2\mathbf{b}^T\mathbf{b} \tag{3.47}$$

Equation (3.47) contains all the information needed to find the optimal external electric field. **If the f function is zero then the optimal oriented external electric field is acting on the optimal BBP**. The lowest amplitude OEEF which turns the f function to zero is the optimal external electric field. Having a zero f function means that the optimal BBP, a gradient extremal point of the unperturbed PES, becomes, under the effect of an OEEF, a degenerate stationary point of perturbed PES. In the optimal BBP coalesce two stationary points of the unperturbed PES, removing the energy barrier between them.

The numerical problem of finding an appropriate field direction such as the f function is zero is discussed in section 3.A.1.

3.3 Applications

In this section, the PMED is applied to two chemical examples.

Since the present model extends the usual dipolar approximation a comparison with a simplified version of the PMED model that does not include the polarizability contributions is also reported, in order to clarify the effect of polarizability in the context of the PMED model.

The calculations were made with the ORCA 5.0.3 [77–81] program system. The potential energy surfaces were computed by means of relaxed surface scans and for each geometry the energy $V(\mathbf{x})$, the electric dipole moment $\mathbf{d}(\mathbf{x})$ and the electric polarizability tensor $\mathbf{A}(\mathbf{x})$ have been extracted. The calculation of the derivatives, the location of the optimal BBP and the quantification of the optimal OEEF were handled by the MANULS program , an open source Python program developed by the author of this thesis[74].

3.3.1 Isomerization of a [3]Cumulene Derivative

The first example is the trans-to-cis isomerization of a [3]Cumulene derivative, it has been selected due to recent experiments indicating that OEEFs accelerate isomerizations in such systems.[82] Figure 3.2 illustrates the molecular process under investigation along with the atom numbering employed.

The investigation begins with the computation of the potential energy curve describing the isomerization. Constrained geometry optimizations are performed, wherein the dihedral angle involving the C1–C2–C3–C4 atoms is fixed, and the remaining degrees of freedom are optimized (refer to fig. 3.2 for the atom numbering). The dihedral angle is scanned from 0° to 180° with a 5° step. A 0° dihedral angle denotes the s-cis isomer, while a 180° dihedral angle denotes the s-trans isomer.

The calculations utilize the UHF [83, 84] method and the 6-31G* basis set [85] in gas phase. The computational approach relies on the broken-symmetry formalism as implemented in ORCA. This approach is adopted due to the singlet state exhibiting a significant open shell/diradical character around the transition state (TS) structure.

Figure 3.2a, fig. 3.2b, fig. 3.2c represent the s-trans isomer, the s-cis isomer and the transition state, respectively. Figure 3.3 shows the unperturbed potential energy curve and curves perturbed by the electric field computed with the PMED model and the simplified PMED model. The geometry of the optimal BBP is reported in fig. 3.4, along with the direction of the optimal external electric field computed with and without the dipolar approximation.

The optimal BBP is a property of the unperturbed potential energy curve, so its determination is independent on the choice of the model. The optimal BBP corresponds to a geometry in which the dihedral angle is equal to 140°.

In this point the optimal OEEF calculated considering both the electric dipole moment and polarizability is in the $(-0.459, 0.487, 0.743)$ direction and its amplitude is 0.0086 a.u. $= 4.43 \cdot 10^9$ V/m. The optimal external electric field calculated considering only the electric dipole moment is in the $(-0.808, 0.273, 0.522)$ direction and its amplitude is 0.0091 a.u. $= 4.70 \cdot 10^9$ V/m. Both the fields are able to remove the isomerization barrier, creating a flat region around the optimal BBP. Even though the amplitudes computed with the two levels of approximation are similar the effect of the polarizability is non negligible on the direction of the optimal field, in fact the angle between the fields 26.9°, underscoring the significance of the polarizability on the response to external electric fields.

It is worth noticing that the application of the electric field modified the entire potential energy curve, this is a numerical example of the shortcomings of the most

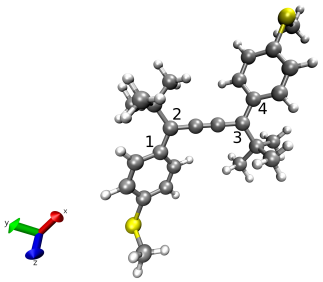

(a) *s-trans isomer*

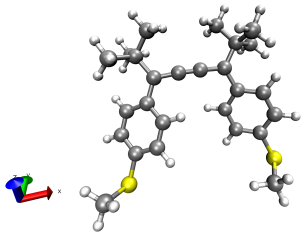

(b) *s-cis isomer*

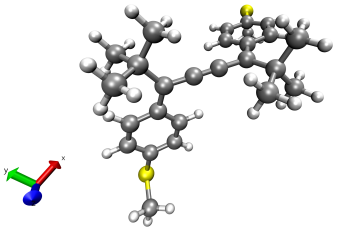

(c) *transition state*

Figure 3.2: Structures of the stationary points of the potential energy curve. The atom numbering used to define the central dihedral angle is indicated in fig. 3.2a

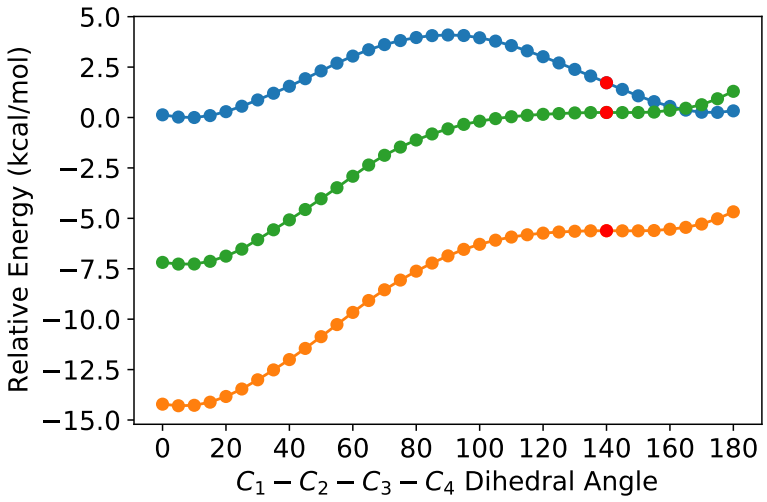

Figure 3.3: Potential energy curves describing the s-trans to s-cis isomerization in all the three discussed cases: no OEEF applied (unperturbed PES) in blue; perturbed PES with optimal OEEF calculated considering the PMED model in orange; perturbed PES with optimal OEEF calculated with the simplified model considering only the electric dipole moment in green. The energy values are relative to the energy minimum of the PES calculated without the effect of the electric field, that is the s-cis isomer in gas phase. The red dot represents the location of the optimal bond breaking point.

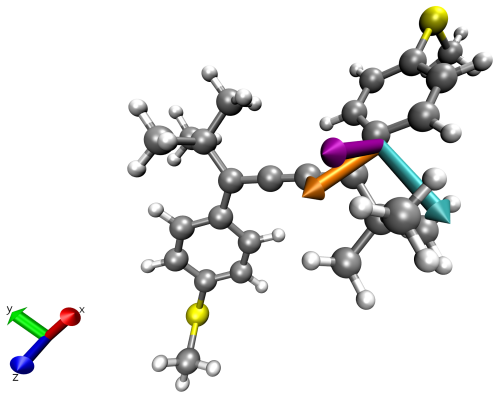

Figure 3.4: Molecular geometry of the optimal BBP. Purple arrow: direction of the optimal external electric field calculated considering the polarizability and the dipole. Orange arrow:direction of the optimal external electric field calculated considering only the dipole. Cyan arrow: direction of molecular electric dipole moment vector.

common theoretical models, based only on the local properties of the reactant and the transition state.

3.3.2 Huisgen Cycloaddition

The second chemical example is taken from the important class of Huisgen cycloaddition reactions, or 1, 3-dipolar cycloadditions [86]. In this reactions a 1,3-dipolar species with 4 π electrons reacts with a dipolarophile with 2 π electrons, forming a five-membered ring.

The case under examination is the addition of ethylene to fulminic acid to give isoxazole. A scheme of the reaction is reported in fig. 3.5, a 3-D representation of the reactants, transition state and product in fig. 3.6.

The PES associated with this reaction can be studied choosing just two internal coordinates, the C_1–C_2 and C_3–O bonds. The goal is not only to find the optimal OEEF, but also to study the optimal FDSP, which was trivial in the one dimensional case.

The ORCA 5.0.3 program system [77–81] has been employed for the characterization of the stationary points and for the relaxed PES scans. The level of theory is B3LYP/def2-TZVP [87–90]. Every calculation employed the D3BJ dispersion correction[91, 92] and the RIJCOSX approximation[93] (which is set by default in the ORCA code for hybrid functionals).

The potential energy surface scans performed constrained the selected internal variables and optimized the remaining degrees of freedom. The exploration of the PES began with a coarse scan, varying the C_1–C_2 and C_3–O bonds (see fig. 3.5 for the atom numbering) from 3.4 Å to 1.2 Å with a step of 0.1 Å. A finer second scan followed, in order to locate precisely the optimal BBP, with the C_1–C_2 and C_3–O bonds scanned from 3.0 Å to 2.4 Å with a step of 0.025 Å. Lastly another scan was

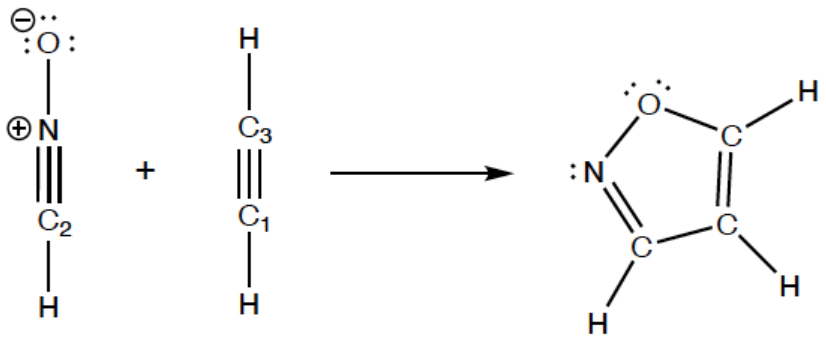

Figure 3.5: The Huisgen reaction between fulminic acid plus acetylene to give isoxazole. The atom numbering is also reported.

used to compute the FDSP, this scan modified the C_1–C_2 and C_3–O bonds from 3.0 Å to 2.1 Å with a step of 0.04 Å.

The optimal BBP is then located on the PES section defined by the C_1–C_2 and C_3–O coordinates. Figure 3.7 shows the PES in vacuum without the effect of the external electric field, the red dot corresponds to the optimal BBP.

Once the optimal BBP is located the field is computed with and without considering the polarizability terms, fig. 3.8 shows the variation on the direction of the optimal OEEF due to the inclusion of polarizability.

The application of the PMED model leads to an optimal OEEF in the (−0.871, 0.036, −0.489) direction with 0.0879 a.u. = 4.52 V/Å amplitude whereas the simplified model leads to a oOEEF pointing in the (−0.722, +0.666, −0.188) direction with an amplitude of 0.1937 a.u. = 9.96 V/Å. Figure 3.8 shows the direction of the two optimal fields with respect to the molecular geometry, fig. 3.9 shows the PES perturbed by the optimal OEEF computed by the PMED model and fig. 3.10 shows the PES perturbed by the simplified version of the PMED model.

The optimal OEEFs derived from both approximations are effective in erasing the reaction barrier but notably differ. The intensities of the oOEEFs computed with the two approximation levels differ by 73%, and the angle between the two field directions is substantial, measuring 44.7°. This emphasizes the essential contribution of polarizability in diminishing the strength of the oOEEF. Importantly, the optimal FDSP computed with the PMED model describes a concerted formation of the $C_1 - C2$ and $C_3 - O$, as expected in this class of reactions.

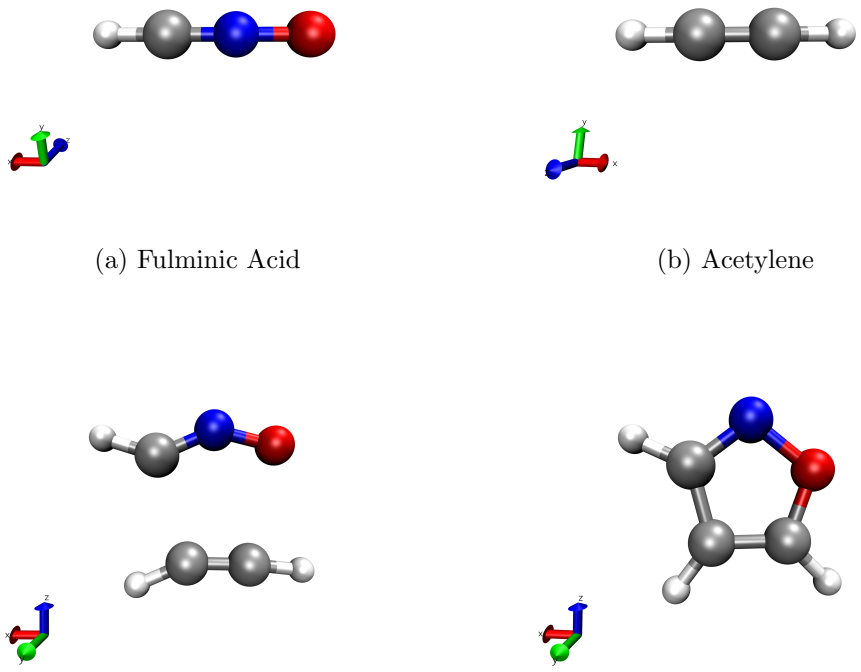

(a) Fulminic Acid

(b) Acetylene

(c) Transiton State

(d) Isoxazole

Figure 3.6: Representation of a-b) the reactants, c) the transition state and d) the product of the 1-3 cycloaddition of fulminic acid and acetylene to isoxazole. The $C_1 - C2$ and $C_3 - O$ bond distances are 2.17 and 2.38 Å for TS, and 1.42 and 1.34 Å for isoxazole.

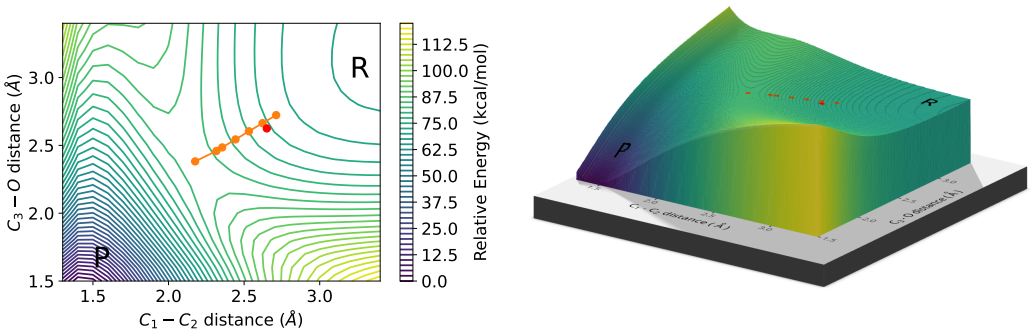

(a) (b)

Figure 3.7: 2D (top) and 3D representations of the original (or unperturbed) PES in the space represented by the $C_1 - C2$ and $C_3 - O$ bond distances. The "R" and "P" denote the reactants and product region. The red dot is the optimal BBP. The orange dots represent the IRC trajectory. The energy is relative to the minimum of the surface of fig. 3.7a.

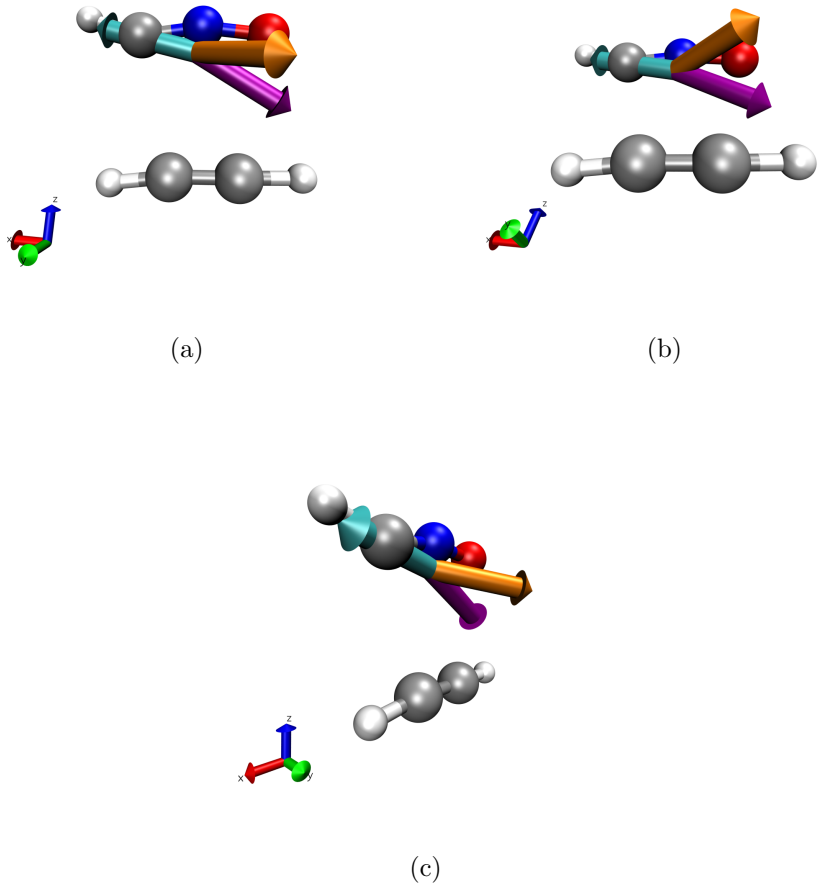

(a) (b)

(c)

Figure 3.8: Three views from different perspectives of the oBBP geometry. The purple arrow represents the direction of the optimal external field calculated considering the PMED model (i.e.: considering both the molecular electric polarizability and the dipole). The orange arrow represents the direction of the optimal external field calculated considering only the electric dipole. The cyan arrow represents the direction of the electric dipole moment vector.

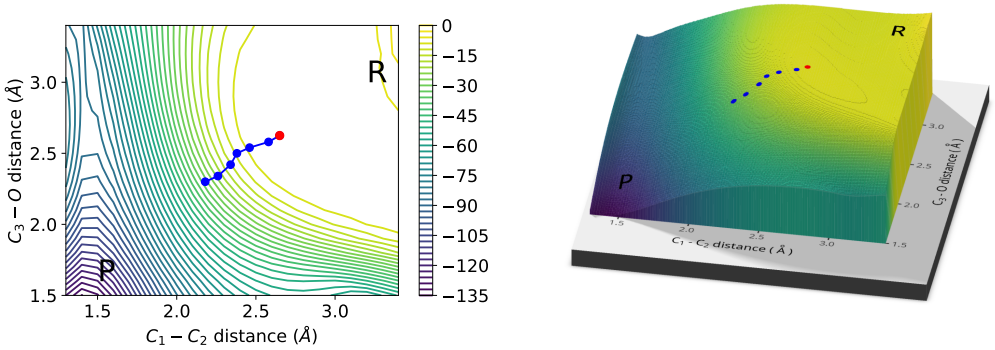

(a) (b)

Figure 3.9: 2D (top) and 3D representations of the perturbed PES with an oOEEF calculated using the PMED model (i.e.: by considering both the polarizability and the dipole). The red dot is the oBBP. The blue dots represent some calculated points of the oFDSP curve. The energy is relative to the minimum of the unperturbed PES in fig. 3.7.

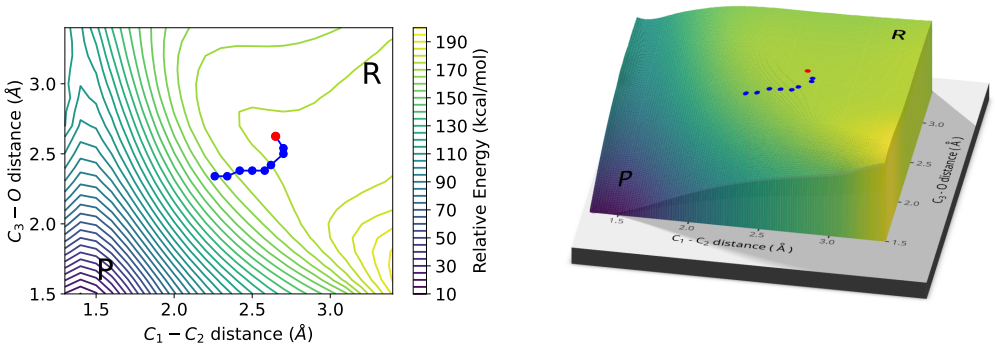

(a) (b)

Figure 3.10: 2D (top) and 3D representations of the perturbed PES with an oOEEF calculated using the simplified model consindering only the electric dipole. The red dot is the oBBP. The blue dots represent some calculated points of the oFDSP curve. The energy is relative to the minimum of the unperturbed PES in fig. 3.7.

3.4 Remarks

In the context of semiclassical interactions between quantized matter and classical electric fields, a model for the electrostatic catalysis of chemical processes has been introduced. The model is based on the Polarizable Molecular Electric Dipole (PMED) ansatz and rooted in catastrophe and optimal control theories. The aim is to provide a framework to find the direction and amplitude of the lowest electric field able to erase a chemical reaction barrier.

The PMED includes two substantial improvements over the widely used models for electrostatic catalysis. Firstly, it goes beyond the first order dipole approximation considering the effect of the polarizability; secondly, it considers the effect of the external electric field on the entire PES, improving the "rigid" models based solely on the electric properties in the reactants and transition state regions.

The central concept is the bond-breaking point (BBP), which is a "special" point of the PES. For each direction of the external electric field there exists an amplitude E such as the reactants and transition state collapse in the BBP, removing the reaction barrier. The BBP, therefore, is a catastrophe point.

Given the infinite number of field directions and associated BBPs, the next step is to find the optimal OEEF and BBP. In this context the optimal OEEF is the electric field with the lowest amplitude able to remove the reaction barrier, the optimal BBP is the BBP associated with the optimal OEEF. Necessary and sufficient conditions to find the optimal BBP and the compute the optimal OEEF are provided, along with an algorithmic procedure.

The capabilities of the PMED model are shown with the application to two chemical examples: the s-trans to s-cis isomerization of a [3]cumulene derivative and the Huisgen cycloaddition of acetylene to fulminic acid. In both the examples the electric field completely removes the reaction barrier, at the same time the inclusion of the polarizability greatly affect the direction and/or the amplitude of the optimal OEEF. It must be reported that the amplitude of the optimal OEEF can become larger than the ones employed in STM experiments. Nevertheless, due to the quadratic effect of the field on the PES, a considerable reduction of the optimal field amplitude can still lead to significant catalytic effects.

In summary, the PMED model offers a comprehensive framework for identifying the optimal direction of an external electric field, moving beyond reliance on chemical intuition. This model yields valuable insights into electrostatic catalytic effects observed across diverse organic and biological processes.

3.A Appendices

3.A.1 Implementation of the PMED Model in the MANULS Code

In this appendix I will cover some of the practical aspects about the location of the optimal BBP and the calculation of the optimal OEEF.

At the moment, the MANULS code works exclusively with 1- and 2-Dimensional scans of the potential energy surface. The computational method used to perform the scan is up to the user, but it has to support the calculation of the dipole moment and of the polarizability at each point of the scan. The user has to provide files that contain the total energies, the dipole moments and the polarizability matrices at each point of the scan. I refer the reader to Ref. [74] for an overview of the input format.

The code works as follows:

1. The code reads the data from the files supplied by the user and reshapes the data in matrices, in this way it is easier to implement the derivatives.

2. The code locates the optimal bond-breaking point. To do so the hessian and the gradient of the original/unperturbed PES are computed in each point. If the unperturbed hessian is called $\mathbf{H}$ and the unperturbed gradient is called $\mathbf{g}$ for each point of the grid the code computes $\|\mathbf{H}\cdot\mathbf{g}\|$ (the norm of this dot product). Then it picks the user-defined number n_bbps of points in which $\|\mathbf{H}\cdot\mathbf{g}\|$ is the smallest and the optimal bond-breaking point is the point, chosen between these n_bbps, in which the unperturbed gradient is maximum. The default for n_bbps is 5, it can be changed by the user.

3. The code generates several points on the unit sphere. The points are generated using the Fibonacci sphere algorithm. Each point, along with the origin, defines a unit vector. The unit vectors generated are stored and used later as directions of the electric field, $\mathbf{e}_n$. In principle, the higher is the number of directions generated, the better is the quality of the result.

4. From now on the code works only on the optimal bond-breaking point. The code picks a direction computed in point 3 and calculates the "ingredients" needed for the analysis. It computes the first and second derivatives of the dipole, of the $\mathbf{f}_{\mathbf{e}_n}$ vector, the hessian and the gradient of the original PES (see eqs. (3.21), (3.23) to (3.26), (3.29) and (3.30)).

5. With the direction of the field ($\mathbf{e}_n$) fixed the code computes the amplitude of the electric field by solving the quadratic equation

$$\begin{aligned}&\mathbf{m}^T_{\mathbf{e}^*_n}(\mathbf{x}_{oBBP},E_{oBBP})\mathbf{m}_{\mathbf{e}^*_n}(\mathbf{x}_{oBBP},E_{oBBP})-\mathbf{g}^T(\mathbf{x}_{oBBP})\mathbf{g}(\mathbf{x}_{oBBP})=\\&1/4\mathbf{p}^T_{\mathbf{e}^*_n}(\mathbf{x}_{oBBP})\mathbf{p}_{\mathbf{e}^*_n}(\mathbf{x}_{oBBP})E^4_{oBBP}+\mathbf{h}^T_{\mathbf{e}^*_n}(\mathbf{x}_{oBBP})\mathbf{p}_{\mathbf{e}^*_n}(\mathbf{x}_{oBBP})E^3_{oBBP}+\\&\mathbf{h}^T_{\mathbf{e}^*_n}(\mathbf{x}_{oBBP})\mathbf{h}_{\mathbf{e}^*_n}(\mathbf{x}_{oBBP})E^2_{oBBP}-\mathbf{g}^T(\mathbf{x}_{oBBP})\mathbf{g}(\mathbf{x}_{oBBP})=0\ ,\end{aligned}\tag{3.48}$$

6. Now the code found, given a direction, the amplitude of the electric field. It needs to check if the field satisfies the requirements for the optimality. To do so there are three (plus one optional) tests:

   (a) The code computes the f function (see eq. (3.47)), the absolute value should be as close as possible to zero. Numerically, if the absolute value of the f function is below a threshold the test is passed. This is the most important test, since the f function contains all the information required.

The other tests are implemented to further check the correctness of the results.

(b) The code computes the norm of the gradient of the PES perturbed by the external field found in the previous points (see eq. (3.26)). This quantity should be as close as possible to zero, if this quantity is below a threshold the test is passed.

(c) The code computes the quantity $\frac{\mathbf{m}\cdot\mathbf{e}}{\|\mathbf{g}\|}$, the absolute value of this quantity should be as close as possible to 1, if the absolute value of this quantity is over a threshold the test is passed. This is a slight reformulation of eq. (3.39). This quantity is included in the f function, so this is a supplementary test.

(d) (**Optional**) The mathematical nature of the problem admits many solutions, this optional test helps to select the one relevant to the chemical problem under consideration. The user has to input the coordinates that define (or that are close to) the reactants. Then the code finds the point of the grid that is closest to these coordinate, that is the point on the grid closest to the reactants. Now the code checks, in the point closest to the reactants, that the energy under the effect of the field is equal or higher to the energy of the optimal bond-breaking point, this ensures that the optimal field correctly catalyzes the reaction. In practice, this steps checks that under the optimal external electric field the reaction goes "downhill".

If all the tests are passed the field is stored. The procedure is repeated for all the directions generated by the Fibonacci algorithm.

7. Lastly the code checks all the fields that satisfy the requirements for the optimality and picks, as the optimal external electric field, the field with the lowest amplitude.

The thresholds used in the code are the following:

- f_tol =5e−5 is the threshold on the f function
- m_tol=0.999 is the threshold on the $\frac{\mathbf{m}\cdot\mathbf{e}}{\|\mathbf{g}\|}$ value
- g_pert_tol =5e−5 is the threshold on the norm of the perturbed gradient
- energy_tol=−0.0048 is the threshold on the difference between the energy of the optimal BBP under the effect of the field and the energy of the reactants under the effect of the field. The default value is the equivalent, in Hartrees, of 3 kcal/mol. In practice, the energy of the reactants under the effect of the field cannot be lower than 3 kcal/mol with respect to the energy of the optimal BBP.

References

[1] Francesca Toschi et al. "Effects of Electric Field Stress on a β-Amyloid Peptide". In: *J. Phys. Chem. B* 113.1 (Jan. 2009). Publisher: American Chemical Society, pp. 369–376. ISSN: 1520-6106. DOI: 10.1021/jp807896g. URL: https://doi.org/10.1021/jp807896g.

[2] Alessandro Venturini and Francesco Zerbetto. "Dynamics of a lipid bilayer induced by electric fields". en. In: *Phys. Chem. Chem. Phys.* 13.20 (May 2011). Publisher: The Royal Society of Chemistry, pp. 9216–9222. ISSN: 1463-9084. DOI: 10.1039/C1CP20322C. URL: https://pubs.rsc.org/en/content/articlelanding/2011/cp/c1cp20322c.

[3] Francesca Lugli et al. "Electric Field Effects on Short Fibrils of Aβ Amyloid Peptides". In: *J. Chem. Theory Comput.* 6.11 (Nov. 2010). Publisher: American Chemical Society, pp. 3516–3526. ISSN: 1549-9618. DOI: 10.1021/ct1001335. URL: https://doi.org/10.1021/ct1001335.

[4] Tobias Cramer, Francesco Zerbetto, and Ricardo García. "Molecular Mechanism of Water Bridge Buildup: Field-Induced Formation of Nanoscale Menisci". In: *Langmuir* 24.12 (June 2008). Publisher: American Chemical Society, pp. 6116–6120. ISSN: 0743-7463. DOI: 10.1021/la800220r. URL: https://doi.org/10.1021/la800220r.

[5] Tobias Cramer et al. "Water-induced polaron formation at the pentacene surface: Quantum mechanical molecular mechanics simulations". In: *Phys. Rev. B* 79.15 (Apr. 2009). Publisher: American Physical Society, p. 155316. DOI: 10.1103/PhysRevB.79.155316. URL: https://link.aps.org/doi/10.1103/PhysRevB.79.155316.

[6] M. Calvaresi et al. "Splitting CO2 with Electric Fields: A Computational Investigation". In: *J. Phys. Chem. Lett.* 1.22 (Nov. 2010). Publisher: American Chemical Society, pp. 3256–3260. DOI: 10.1021/jz101005u. URL: https://doi.org/10.1021/jz101005u.

[7] J.L. Andrés et al. "Electric fields acting as catalysts in chemical reactions. An ab initio study of the walden inversion reaction". In: *Chem. Phys. Lett.* 153.1 (1988), pp. 82–86. ISSN: 0009-2614. DOI: https://doi.org/10.1016/0009-2614(88)80136-2. URL: https://www.sciencedirect.com/science/article/pii/0009261488801362.

[8] Emili Carbonell et al. "Catalysis of Friedel-Crafts reactions by electric fields". In: *J. Phys. Chem.* 95.1 (1991), pp. 179–183. DOI: 10.1021/j100154a036. URL: https://doi.org/10.1021/j100154a036.

[9] Rinat Meir et al. "Oriented Electric Fields Accelerate Diels–Alder Reactions and Control the endo/exo Selectivity". In: *ChemPhysChem* 11.1 (2010), pp. 301–310. DOI: https://doi.org/10.1002/cphc.200900848. URL: https://chemistry-europe.onlinelibrary.wiley.com/doi/abs/10.1002/cphc.200900848.

[10] Sason Shaik, Sam P. de Visser, and Devesh Kumar. "External Electric Field Will Control the Selectivity of Enzymatic-Like Bond Activations". In: *Journal of the American Chemical Society* 126.37 (2004). PMID: 15366922, pp. 11746–11749. DOI: 10.1021/ja047432k. URL: https://doi.org/10.1021/ja047432k.

[11] Hajime Hirao et al. "Effect of External Electric Fields on the C-H Bond Activation Reactivity of Nonheme Iron-oxo Reagents". In: *J. Am. Chem. Soc.* 130.11 (2008), pp. 3319–3327. DOI: 10.1021/ja070903t. URL: https://doi.org/10.1021/ja070903t.

[12] Albert C. Aragonès et al. "Electrostatic catalysis of a Diels–Alder reaction". en. In: *Nature* 531.7592 (Mar. 2016). Number: 7592 Publisher: Nature Publishing Group, pp. 88–91. ISSN: 1476-4687. DOI: 10.1038/nature16989. URL: https://www.nature.com/articles/nature16989.

[13] Long Zhang et al. "Electrochemical and Electrostatic Cleavage of Alkoxyamines". In: *J. Am. Chem. Soc.* 140.2 (2018), pp. 766–774. DOI: 10.1021/jacs.7b11628. URL: https://doi.org/10.1021/jacs.7b11628.

[14] Xiaoyan Huang et al. "Electric field-induced selective catalysis of single-molecule reaction". In: *Sci. Adv.* 5.6 (2019), eaaw3072. DOI: 10.1126/sciadv.aaw3072. URL: https://advances.sciencemag.org/content/5/6/eaaw3072.

[15] Yaping Zang et al. "Directing isomerization reactions of cumulenes with electric fields". In: *Nat. Commun.* 10.1 (2019), p. 4482. DOI: 10.1038/s41467-019-12487-w. URL: https://doi.org/10.1038/s41467-019-12487-w.

[16] Junfeng Lin et al. "Cleavage of non-polar C(sp^2)-C(sp^2) bonds in cycloparaphenylenes via electric field-catalyzed electrophilic aromatic substitution". In: *Nat. Commun.* 14.1 (2023), pp. 293–299. DOI: 10.1038/s41467-022-35686-4. URL: https://doi.org/10.1038/s41467-022-35686-4.

[17] Boyuan Zhang et al. "Electric fields drive bond homolysis". In: *Chem. Sci.* 14.7 (2023), pp. 1769–1774. DOI: 10.1039/d2sc06411a. URL: https://doi.org/10.1039/d2sc06411a.

[18] Xiye Wang et al. "Alkane Solvent-Derived Acylation Reaction Driven by Electric Fields". In: *J. Am. Chem. Soc.* 145.22 (2023), pp. 11903–11906. DOI: 10.1021/jacs.3c02064. URL: https://doi.org/10.1021/jacs.3c02064.

[19] Simone Ciampi et al. "Harnessing electrostatic catalysis in single molecule, electrochemical and chemical systems: a rapidly growing experimental tool box". In: *Chem. Soc. Rev.* 47 (14 2018), pp. 5146–5164. DOI: 10.1039/C8CS00352A. URL: http://dx.doi.org/10.1039/C8CS00352A.

[20] Masaaki Akamatsu, Naomi Sakai, and Stefan Matile. "Electric-Field-Assisted Anion-π Catalysis". In: *J. Am. Chem. Soc.* 139.19 (2017), pp. 6558–6561. DOI: 10.1021/jacs.7b02421. URL: https://doi.org/10.1021/jacs.7b02421.

[21] Yan B. Vogel et al. "Reproducible flaws unveil electrostatic aspects of semiconductor electrochemistry". In: *Nat. Comm.* 8.1 (2017), p. 2066. DOI: 110.1038/s41467-017-02091-1. URL: https://doi.org/10.1038/s41467-017-02091-1.

[22] Craig F. Gorin et al. "Interfacial Electric Field Effects on a Carbene Reaction Catalyzed by Rh Porphyrins". In: *J. Am. Chem. Soc.* 135.30 (2013), pp. 11257–11265. DOI: 10.1021/ja404394z. URL: https://doi.org/10.1021/ja404394z.

[23] Marta Klinska et al. "Experimental demonstration of pH-dependent electrostatic catalysis of radical reactions". In: *Chem. Sci.* 6 (10 2015), pp. 5623–5627. DOI: 10.1039/C5SC01307K. URL: http://dx.doi.org/10.1039/C5SC01307K.

[24] Mitchell T. Blyth and Michelle L. Coote. "A pH-Switchable Electrostatic Catalyst for the Diels-Alder Reaction: Progress toward Synthetically Viable Electrostatic Catalysis". In: *J. Org. Chem.* 84.3 (2019), pp. 1517–1522. DOI: 10.1021/acs.joc.8b02940. URL: https://doi.org/10.1021/acs.joc.8b02940.

[25] Nadia G. Léonard et al. "Electric Fields in Catalysis: From Enzymes to Molecular Catalysts". In: *ACS Catalysis* 11.17 (2021), pp. 10923–10932. DOI: 10.1021/acscatal.1c02084. URL: https://doi.org/10.1021/acscatal.1c02084.

[26] Sason Shaik and Thijs Stuyver, eds. *Effects of Electric Fields on Structure and Reactivity*. New Horizons in Chemistry, Theoretical and Computational Chemistry Series. The Royal Society of Chemistry, 2021, pp. 001–428.

[27] Thijs Stuyver et al. "External electric field effects on chemical structure and reactivity". In: *WIRES Comput. Mol. Sci.* 10.2 (2020), e1438. DOI: https://doi.org/10.1002/wcms.1438. URL: https://wires.onlinelibrary.wiley.com/%doi/abs/10.1002/wcms.1438.

[28] Zhanfeng Wang et al. "Oriented-External Electric Fields Create Absolute Enantioselectivity in Diels-Alder Reactions: Importance of the Molecular Dipole Moment". In: *J. Am. Chem. Soc.* 140.41 (2018), pp. 13350–13359. DOI: 10.1021/jacs.8b08233. URL: https://doi.org/10.1021/jacs.8b08233.

[29] Heather M. Aitken and Michelle L. Coote. "Can electrostatic catalysis of Diels-Alder reactions be harnessed with pH-switchable charged functional groups?" In: *Phys. Chem. Chem. Phys.* 20 (16 2018), pp. 10671–10676. DOI: 10.1039/C7CP07562F. URL: http://dx.doi.org/10.1039/C7CP07562F.

[30] Kalishankar Bhattacharyya, Sharmistha Karmakar, and Ayan Datta. "External electric field control: driving the reactivity of metal-free azide-alkyne click reactions". In: *Phys. Chem. Chem. Phys.* 19 (33 2017), pp. 22482–22486. DOI: 10.1039/C7CP04202G. URL: http://dx.doi.org/10.1039/C7CP04202G.

[31] Song Yu et al. "How Oriented External Electric Fields Modulate Reactivity". In: *Chem. Eur. J.* 27.18 (2021), pp. 5683–5693. DOI: https://doi.org/10.1002/chem.202004906. URL: https://chemistry-europe.onlinelibrary.wiley.com/doi/abs/10.1002/chem.202004906.

[32] Pau Besalú-Sala et al. "Fast and Simple Evaluation of the Catalysis and Selectivity Induced by External Electric Fields". In: *ACS Catalysis* 11.23 (2021), pp. 14467–14479. DOI: 10.1021/acscatal.1c04247. URL: https://doi.org/10.1021/acscatal.1c04247.

[33] Rajeev Ramanan et al. "Catalysis of Methyl Transfer Reactions by Oriented External Electric Fields: Are Gold-Thiolate Linkers Innocent?" In: *J. Am. Chem. Soc.* 140.12 (2018), pp. 4354–4362. DOI: 10.1021/jacs.8b00192. URL: https://doi.org/10.1021/jacs.8b00192.

[34] Edoardo Jun Mattioli et al. "Oriented External Electric Fields Affect Rate and Stereoselectivity of Electrocyclic Reactions". In: *J. Phys. Chem. C* 123.43 (2019), pp. 26370–26378. DOI: 10.1021/acs.jpcc.9b07358. URL: https://doi.org/10.1021/acs.jpcc.9b07358.

[35] Thijs Stuyver et al. "Electrophilic Aromatic Substitution Reactions: Mechanistic Landscape, Electrostatic and Electric-Field Control of Reaction Rates, and Mechanistic Crossovers". In: *J. Am. Chem. Soc.* 141.24 (2019), pp. 9719–9730. DOI: 10.1021/jacs.9b04982. URL: https://doi.org/10.1021/jacs.9b04982.

[36] Jyothish Joy, Thijs Stuyver, and Sason Shaik. "Oriented External Electric Fields and Ionic Additives Elicit Catalysis and Mechanistic Crossover in Oxidative Addition Reactions". In: *J. Am. Chem. Soc.* 142.8 (2020), pp. 3836–3850. DOI: 10.1021/jacs.9b11507. URL: https://doi.org/10.1021/jacs.9b11507.

[37] Carles Acosta-Silva et al. "Kemp Elimination Reaction Catalyzed by Electric Fields". In: *ChemPhysChem* 21.4 (2020), pp. 295–306. DOI: https://doi.org/10.1002/cphc.201901155. URL: https://chemistry-europe.onlinelibrary.wiley.com/%doi/abs/10.1002/cphc.201901155.

[38] Yu Chen et al. "Degradation of bromobenzene via external electric field". In: *J. Theor. Comput. Chem.* 19.01 (2020), p. 2050004. DOI: 10.1142/S0219633620500042. URL: https://doi.org/10.1142/S0219633620500042.

[39] Jie Wu et al. "Oriented External Electric Fields Regurating the Reaction Mechanism of CH4 Oxidation Catalyzed by Fe(IV)-Oxo-Corrolazine: Insight from Density Functional Calculations". In: *Frontiers in Chemistry* 10 (2022). ISSN: 2296-2646. DOI: 10.3389/fchem.2022.896944. URL: https://www.frontiersin.org/articles/10.3389/fchem.2022.896944.

[40] Fanglin Che et al. "Improving Ni Catalysts Using Electric Fields: A DFT and Experimental Study of the Methane Steam Reforming Reaction". In: *ACS Catal.* 7.1 (2017), pp. 551–562. DOI: 10.1021/acscatal.6b02318. URL: https://doi.org/10.1021/acscatal.6b02318.

[41] Fanglin Che et al. "Elucidating the Roles of Electric Fields in Catalysis: A Perspective". In: *ACS Catal.* 8.6 (2018), pp. 5153–5174. DOI: 10.1021/acscatal.7b02899. URL: https://doi.org/10.1021/acscatal.7b02899.

[42] Emily M. Kempfer-Robertson and Lee M. Thompson. "Effect of Oriented External Electric Fields on the Photo and Thermal Isomerization of Azobenzene". In: *The Journal of Physical Chemistry A* 124.18 (2020). PMID: 32286821, pp. 3520–3529. DOI: 10.1021/acs.jpca.0c00492. URL: https://doi.org/10.1021/acs.jpca.0c00492.

[43] Kílian Jutglar Lozano et al. "Twistable dipolar aryl rings as electric field actuated conformational molecular switches". In: *Phys. Chem. Chem. Phys.* 23 (6 2021), pp. 3844–3855. DOI: 10.1039/D0CP06549H. URL: http://dx.doi.org/10.1039/D0CP06549H.

[44] Thijs Stuyver and Sason Shaik. "Resolving Entangled Reactivity Modes through External Electric Fields and Substitution: Application to E_2/S_N2 Reactions". In: *J. Org. Chem.* 86.13 (2021), pp. 9030–9039. DOI: 10.1021/acs.joc.1c01010. URL: https://doi.org/10.1021/acs.joc.1c01010.

[45] Mingxia Zhang et al. "Green Catalytic Method for Hydrothiolation of Allylamines: An External Electric Field". In: *ACS Omega* 7.7 (2022), pp. 5782–5790. DOI: 10.1021/acsomega.1c05741. URL: https://doi.org/10.1021/acsomega.1c05741.

[46] H. Ray Kelly et al. "Controlling Hydricity of Adsorbed Catalysts with Applied Electric Fields". In: *J. Phys. Chem. C* 127.14 (Mar. 2023), pp. 6733–6743. DOI: 10.1021/acs.jpcc.3c00829. URL: https://doi.org/10.1021/acs.jpcc.3c00829.

[47] Dalton J. Hanaway and C. Rose Kennedy. "Automated Variable Electric-Field DFT Application for Evaluation of Optimally Oriented Electric Fields on Chemical Reactivity". In: *J. Org. Chem.* 88.1 (2023), pp. 106–115. DOI: 10.1021/acs.joc.2c01893. URL: https://doi.org/10.1021/acs.joc.2c01893.

[48] Arieh Warshel et al. "Electrostatic Basis for Enzyme Catalysis". In: *Chemical Reviews* 106.8 (2006). PMID: 16895325, pp. 3210–3235. DOI: 10.1021/cr0503106. URL: https://doi.org/10.1021/cr0503106.

[49] Stephen D. Fried, Sayan Bagchi, and Steven G. Boxer. "Extreme electric fields power catalysis in the active site of ketosteroid isomerase". In: *Science* 346.6216 (2014), pp. 1510–1514. DOI: 10.1126/science.1259802. URL: https://www.science.org/doi/abs/10.1126/science.1259802.

[50] Stephen D. Fried and Steven G. Boxer. "Electric Fields and Enzyme Catalysis". In: *Annual Review of Biochemistry* 86.1 (2017). PMID: 28375745, pp. 387–415. DOI: 10.1146/annurev-biochem-061516-044432. URL: https://doi.org/10.1146/annurev-biochem-061516-044432.

[51] Asmit Bhowmick, Sudhir C. Sharma, and Teresa Head-Gordon. "The Importance of the Scaffold for de Novo Enzymes: A Case Study with Kemp Eliminase". In: *J. Am. Chem. Soc.* 139.16 (2017), pp. 5793–5800. DOI: 10.1021/jacs.6b12265. URL: https://doi.org/10.1021/jacs.6b12265.

[52] Mark Dittner and Bernd Hartke. "Globally Optimal Catalytic Fields – Inverse Design of Abstract Embeddings for Maximum Reaction Rate Acceleration". In: *Journal of Chemical Theory and Computation* 14.7 (2018). PMID: 29883539, pp. 3547–3564. DOI: 10.1021/acs.jctc.8b00151. URL: https://doi.org/10.1021/acs.jctc.8b00151.

[53] Valerie Vaissier Welborn and Teresa Head-Gordon. "Fluctuations of Electric Fields in the Active Site of the Enzyme Ketosteroid Isomerase". In: *J. Am. Chem. Soc.* 141.32 (2019), pp. 12487–12492. DOI: 10.1021/jacs.9b05323. URL: https://doi.org/10.1021/jacs.9b05323.

[54] Valerie Vaissier Welborn, Luis Ruiz Pestana, and Teresa Head-Gordon. "Computational optimization of electric fields for better catalysis design". en. In: *Nat Catal* 1.9 (Sept. 2018). Number: 9 Publisher: Nature Publishing Group, pp. 649–655. ISSN: 2520-1158. DOI: 10.1038/s41929-018-0109-2. URL: https://www.nature.com/articles/s41929-018-0109-2.

[55] Mark Dittner and Bernd Hartke. "Globally optimal catalytic fields for a Diels–Alder reaction". In: *The Journal of Chemical Physics* 152.11 (Mar. 2020), p. 114106. ISSN: 0021-9606. DOI: 10.1063/1.5142839. URL: https://doi.org/10.1063/1.5142839.

[56] Chu Zheng et al. "A two-directional vibrational probe reveals different electric field orientations in solution and an enzyme active site". en. In: *Nat. Chem.* 14.8 (Aug. 2022). Number: 8 Publisher: Nature Publishing Group, pp. 891–897. ISSN: 1755-4349. DOI: 10.1038/s41557-022-00937-w. URL: https://www.nature.com/articles/s41557-022-00937-w.

[57] Thijs Stuyver et al. "Oriented (Local) Electric Fields Drive the Millionfold Enhancement of the H-Abstraction Catalysis Observed for Synthetic Metalloenzyme Analogues". In: *Angew. Chem. Int. Ed.* 59.20 (Mar. 2020), pp. 7915–7920. DOI: 10.1002/anie.201916592. URL: https://doi.org/10.1002/anie.201916592.

[58] Rene Thom. *Structural Stability and Morphogenesis: An Outline of a General Theory of Models*. Reading, MA: Addison-Wesley, 1989.

[59] R. Gilmore. *Catastrophe Theory for Scientists and Engineers*. Dover, New York, 1993.

[60] Josep Maria Bofill et al. "Controlling Chemical Reactivity with Optimally Oriented Electric Fields: A Generalization of the Newton Trajectory Method". In: *Journal of Chemical Theory and Computation* 18.2 (2022). PMID: 35044173, pp. 935–952. DOI: 10.1021/acs.jctc.1c00943. URL: https://doi.org/10.1021/acs.jctc.1c00943.

[61] Constantin Carathéodory. *Calculus of Variations and Partial Differential Equations of the First Order*. New York, N. Y. 10016: Chelsea Publishing Company, 1982.

[62] J. Pancíř. "Calculation of the least energy path on the energy hypersurface". In: *Collection Czechoslov Chem Commun* 40 (1975), pp. 1112–1118.

[63] M.V. Basilevsky and A.G. Shamov. "The local definition of the Optimum ascent path on a multi-dimensional potential energy surface and its practical application for the location of saddle points". In: *Chemical Physics* 60.3 (1981), pp. 347–358. ISSN: 0301-0104. DOI: https://doi.org/10.1016/0301-0104(81)80170-X. URL: https://www.sciencedirect.com/science/article/pii/030101048180170X.

[64] D. J. Rowe and A. Ryman. "Valleys and fall lines on a Riemannian manifold". In: *Journal of Mathematical Physics* 23.5 (May 1982), pp. 732–735. ISSN: 0022-2488. DOI: 10.1063/1.525427. URL: https://doi.org/10.1063/1.525427.

[65] M.V. Basilevsky. "The topography of potential energy surfaces". In: *Chem. Phys.* 67.3 (1982), pp. 337–346. ISSN: 0301-0104. DOI: https://doi.org/10.1016/0301-0104(82)85194-X. URL: https://www.sciencedirect.com/science/article/pii/030101048285194X.

[66] David K. Hoffman, Ross S. Nord, and Klaus Ruedenberg. "Gradient extremals". en. In: *Theoret. Chim. Acta* 69.4 (May 1986), pp. 265–279. ISSN: 1432-2234. DOI: 10.1007/BF00527704. URL: https://doi.org/10.1007/BF00527704.

[67] Wolfgang Quapp. "Gradient extremals and valley floor bifurcations on potential energy surfaces". en. In: *Theoret. Chim. Acta* 75.6 (Nov. 1989), pp. 447–460. ISSN: 1432-2234. DOI: 10.1007/BF00527676. URL: https://doi.org/10.1007/BF00527676.

[68] Dietmar Heidrich, Wolfgang Kliesch, and Wolfgang Quapp. *Properties of Chemically Interesting Potential Energy Surfaces*. Berlin, Heidelberg: Springer, 1991.

[69] H. Bernhard Schlegel. "Following gradient extremal paths". en. In: *Theoret. Chim. Acta* 83.1 (Jan. 1992), pp. 15–20. ISSN: 1432-2234. DOI: 10.1007/BF01113240. URL: https://doi.org/10.1007/BF01113240.

[70] Jun-Qiang Sun and Klaus Ruedenberg. "Gradient extremals and steepest descent lines on potential energy surfaces". In: *The Journal of Chemical Physics* 98.12 (June 1993), pp. 9707–9714. ISSN: 0021-9606. DOI: 10.1063/1.464349. URL: https://doi.org/10.1063/1.464349.

[71] Kent Bondensgård and Frank Jensen. "Gradient extremal bifurcation and turning points: An application to the H_2CO potential energy surface". In: *J. Chem. Phys.* 104.20 (1996), pp. 8025–8031. DOI: 10.1063/1.471495. URL: https://doi.org/10.1063/1.471495.

[72] Josep Maria Bofill, Wolfgang Quapp, and Marc Caballero. "The Variational Structure of Gradient Extremals". In: *Journal of Chemical Theory and Computation* 8.3 (2012). PMID: 26593355, pp. 927–935. DOI: 10.1021/ct200805d. URL: https://doi.org/10.1021/ct200805d.

[73] Wolfgang Quapp and Josep Maria Bofill. "A contribution to a theory of mechanochemical pathways by means of Newton trajectories". en. In: *Theor Chem Acc* 135.4 (Apr. 2016), p. 113. ISSN: 1432-2234. DOI: 10.1007/s00214-016-1880-2. URL: https://doi.org/10.1007/s00214-016-1880-2.

[74] Josep Maria Bofill Villà et al. *MANULS (Make chemicAl reactioNs spontaneoUs via optimaL fieldS)*. Version 1.0.0.

[75] Josep Maria Bofill et al. "An algorithm to locate optimal bond breaking points on a potential energy surface for applications in mechanochemistry and catalysis". In: *The Journal of Chemical Physics* 147.15 (Aug. 2017), p. 152710. ISSN: 0021-9606. DOI: 10.1063/1.4994925. URL: https://doi.org/10.1063/1.4994925.

[76] Josep Maria Bofill et al. "Barnes Update Applied in the Gauss–Newton Method: An Improved Algorithm to Locate Bond Breaking Points". In: *Journal of Chemical Theory and Computation* 17.2 (2021). PMID: 33464895, pp. 996–1007. DOI: 10.1021/acs.jctc.0c00910. URL: https://doi.org/10.1021/acs.jctc.0c00910.

[77] Frank Neese. "The ORCA program system". In: *WIREs Computational Molecular Science* 2.1 (2012), pp. 73–78. DOI: https://doi.org/10.1002/wcms.81. URL: https://wires.onlinelibrary.wiley.com/doi/abs/10.1002/wcms.81.

[78] Frank Neese. "Software update: the ORCA program system, version 4.0". In: *WIREs Computational Molecular Science* 8.1 (2018), e1327. DOI: https://doi.org/10.1002/wcms.1327. URL: https://wires.onlinelibrary.wiley.com/doi/abs/10.1002/wcms.1327.

[79] Frank Neese et al. "The ORCA quantum chemistry program package". In: *The Journal of Chemical Physics* 152.22 (June 2020), p. 224108. ISSN: 0021-9606. DOI: 10.1063/5.0004608. URL: https://doi.org/10.1063/5.0004608.

[80] Frank Neese. "Software update: The ORCA program system—Version 5.0". In: *WIREs Computational Molecular Science* 12.5 (2022), e1606. DOI: https://doi.org/10.1002/wcms.1606. URL: https://wires.onlinelibrary.wiley.com/doi/abs/10.1002/wcms.1606.

[81] Frank Neese. "The SHARK integral generation and digestion system". In: *Journal of Computational Chemistry* 44.3 (2023), pp. 381–396. DOI: https://doi.org/10.1002/jcc.26942. URL: https://onlinelibrary.wiley.com/doi/abs/10.1002/jcc.26942.

[82] Yaping Zang et al. "Directing isomerization reactions of cumulenes with electric fields". In: *Nat. Commun.* 10.1 (2019), p. 4482. ISSN: 2041-1723. DOI: 10.1038/s41467-019-12487-w. URL: https://doi.org/10.1038/s41467-019-12487-w.

[83] Berthier, Gaston. "Configurations électroniques incomplètes - Partie I. La Méthode du Champ Moléculaire Self-Consistent et l'Etude des Etats à Couches Incomplètes". In: *J. Chim. Phys.* 51 (1954), pp. 363–371. DOI: 10.1051/jcp/1954510363. URL: https://doi.org/10.1051/jcp/1954510363.

[84] J. A. Pople and R. K. Nesbet. "Self-Consistent Orbitals for Radicals". In: *The Journal of Chemical Physics* 22.3 (Dec. 2004), pp. 571–572. ISSN: 0021-9606. DOI: 10.1063/1.1740120. URL: https://doi.org/10.1063/1.1740120.

[85] W. J. Hehre, R. Ditchfield, and J. A. Pople. "Self—Consistent Molecular Orbital Methods. XII. Further Extensions of Gaussian—Type Basis Sets for Use in Molecular Orbital Studies of Organic Molecules". In: *Journal of Chemical Physics* 56 (Mar. 1972), pp. 2257–2261. ISSN: 0021-96060301-0104. DOI: 10.1063/1.1677527. URL: https://ui.adsabs.harvard.edu/abs/1972JChPh..56.2257H.

[86] Rolf Huisgen. "1,3-Dipolar Cycloadditions. Past and Future". In: *Angewandte Chemie International Edition in English* 2.10 (1963), pp. 565–598. DOI: https://doi.org/10.1002/anie.196305651. URL: https://onlinelibrary.wiley.com/doi/abs/10.1002/anie.196305651.

[87] Axel D. Becke. "Density-functional thermochemistry. III. The role of exact exchange". In: *The Journal of Chemical Physics* 98.7 (Apr. 1993), pp. 5648–5652. ISSN: 0021-9606. DOI: 10.1063/1.464913. URL: https://doi.org/10.1063/1.464913.

[88] Chengteh Lee, Weitao Yang, and Robert G. Parr. "Development of the Colle-Salvetti correlation-energy formula into a functional of the electron density". In: *Phys. Rev. B* 37 (2 1988), pp. 785–789. DOI: 10.1103/PhysRevB.37.785. URL: https://link.aps.org/doi/10.1103/PhysRevB.37.785.

[89] P. J. Stephens et al. "Ab Initio Calculation of Vibrational Absorption and Circular Dichroism Spectra Using Density Functional Force Fields". In: *The Journal of Physical Chemistry* 98.45 (1994), pp. 11623–11627. DOI: 10.1021/j100096a001. URL: https://doi.org/10.1021/j100096a001.

[90] Florian Weigend and Reinhart Ahlrichs. "Balanced basis sets of split valence, triple zeta valence and quadruple zeta valence quality for H to Rn: Design and assessment of accuracy". In: *Phys. Chem. Chem. Phys.* 7 (18 2005), pp. 3297–3305. DOI: 10.1039/B508541A. URL: http://dx.doi.org/10.1039/B508541A.

[91] Stefan Grimme et al. "A consistent and accurate ab initio parametrization of density functional dispersion correction (DFT-D) for the 94 elements H-Pu". In: *The Journal of Chemical Physics* 132.15 (Apr. 2010), p. 154104. ISSN: 0021-9606. DOI: 10.1063/1.3382344. URL: https://doi.org/10.1063/1.3382344.

[92] Stefan Grimme, Stephan Ehrlich, and Lars Goerigk. "Effect of the damping function in dispersion corrected density functional theory". In: *Journal of Computational Chemistry* 32.7 (2011), pp. 1456–1465. DOI: https://doi.org/10.1002/jcc.21759. URL: https://onlinelibrary.wiley.com/doi/abs/10.1002/jcc.21759.

[93] Frank Neese et al. "Efficient, approximate and parallel Hartree–Fock and hybrid DFT calculations. A 'chain-of-spheres' algorithm for the Hartree–Fock exchange". In: *Chemical Physics* 356.1 (2009). Moving Frontiers in Quantum Chemistry: pp. 98–109. ISSN: 0301-0104. DOI: https://doi.org/10.1016/j.chemphys.2008.10.036. URL: https://www.sciencedirect.com/science/article/pii/S0301010408005089.

Chapter 4

Polaritonic Chemistry

In this last chapter, finally, the treatment of both electric field and matter is addressed within the framework of quantum mechanics. Therefore there is the need to explicitly consider the quanta of the electromagnetic field, the photons [1, 2].

Traditionally, the application of electric fields in chemistry has relied upon a semiclassical formalism, assuming a classical electric field. However, certain phenomena defy this approximation, necessitating a quantum mechanical description of the electric field. Noteworthy among these phenomena are spontaneous emission and lasing [3]. The expanding intersection between chemistry and quantum optics is driven by advancements in the precise control of photonic states. This advancement has given rise to innovative experimental methodologies grounded in the principles of quantized light. Examples include ultrafast spectroscopies [4], spectroscopies relying on quantum states of light, such as entangled photons [5], and quantum imaging techniques [6].

Within the intersection between quantum optics and chemistry, a research area gained popularity in the last decade: polaritonic chemistry.

The premise of polaritonic chemistry is the existence of hybrid light-matter states, denoted as polaritonic states or polaritons, wherein light and matter undergo a mixing akin to the hybridization observed in atomic orbitals [7]. The formation of polaritons occurs under specific conditions commonly referred to as strong light-matter coupling. A precise definition of strong light-matter coupling will be provided later in this chapter. At this juncture it is sufficient to underline that in conventional photochemistry it is often assumed that the coupling of molecules with external fields is weak and that the nature of the molecular states is not modified by the electric field (whether classical or quantized); due to the formation of new polaritonic states this assumption does not hold under strong light-matter coupling conditions[8].

The formation of polaritonic states leads to a new way to control chemical phenomena [9–14]. The most immediate consequence of the polariton formation is a modification of the Potential Energy Surface (PES), which alters reaction pathways and rates [9, 15–21]. From the computational point of view it is now possible to simulate, both statically and dynamically [22–25], proton transfer [26],energy transfer [27], electron transfer [28–30], intermolecular interactions [31], relativistic effects [32] and, in general, the effect of polaritons on reactivity [33–37].

In this chapter, section 4.1 is devoted to a theoretical introduction to the computational modeling of molecular polaritons and sections 4.2.1 and 4.2.2 to the examination of the response of butadiene and hexatriene molecules to strong light-matter coupling.

4.1 Theory

The study of polaritonic systems necessitates a quantum mechanical treatment of electromagnetic modes, requiring the application of quantum electrodynamics (QED). The simplest approach to introduce the interaction between a two-level system and a single mode is the Jaynes-Cummings model [38]. Despite its simplicity, which will be addressed later, the Jaynes-Cummings model provides valuable insights into light-matter interaction.

The model considers a single emitter with two states, a ground state $|g\rangle$ and an excited state $|e\rangle$. The associated Hamiltonian is

$$\hat{H}_M = E_g |g\rangle \langle g| + E_e |e\rangle \langle e| \tag{4.1}$$

where E_g is the ground state energy and E_e is the excited state energy. The interaction between a single emitter and a single mode is described by the Jaynes-Cummings Hamiltonian

$$\hat{H}_{JC} = \hat{H}_M + \hbar\omega_c \left(\hat{a}^\dagger \hat{a} + \frac{1}{2}\right) + \hbar g_c \left(\hat{\sigma}^\dagger \hat{a} + \hat{\sigma}\hat{a}^\dagger\right) \tag{4.2}$$

In this expression, $\hat{a}^\dagger$ and $\hat{a}$ denote the creation and annihilation operators for the field, $\hat{\sigma}^\dagger = |e\rangle \langle g|$ and $\hat{\sigma} = |g\rangle \langle e|$ serve as the raising and lowering operators for molecular excitation, and ω_c represents the mode frequency.

The Jaynes-Cummings Hamiltonian is made of three terms. $\hat{H}_M$ stands for the emitter Hamiltonian. $\hbar\omega_c \left(\hat{a}^\dagger \hat{a} + \frac{1}{2}\right)$ is the Hamiltonian of the quantized electromagnetic field under the single mode approximation, its eigenstate $|n\rangle$ represents the number of photons. The final term describes the light-matter interaction, allowing the excitation or de-excitation of the emitter and the subsequent annihilation or creation of a photon. This interaction is governed by the coupling strength parameter g_c, defined as:

$$g_c = \sqrt{\frac{\hbar\omega_c}{2\varepsilon V}} \hat{e}\mu_{eg} \tag{4.3}$$

where ε is the medium permittivity, V is the effective quantization volume, $\hat{e}$ is the unit vector associated with the direction of the electromagnetic field mode and μ_{eg} is the transition dipole moment vector between the ground and excited state.

A non-zero g_c parameter allows the emitter-mode interaction. The resulting eigenstates mix the matter degrees of freedom and the photonic degrees of freedom, forming hybrid states called polaritonic states or polaritons. In this context, the matter and photonic degrees of freedom are combined in the same fashion as s and p orbitals are[7]. The effective strength of the coupling increases with the number of emitters coupled with the electromagnetic mode. According to the Tavis-Cummings

model, an extension of the Jaynes-Cummings model to N emitters, the coupling strength becomes $g_c\sqrt{N}$[39].

Traditional photochemistry in gas or liquid phase already treats a large number of molecule variously coupled with the electromagnetic modes [8], however the formation of polaritons cannot be measured with the traditional experimental setups. This is due to the fact that in free space the light-matter coupling strength is negligible, therefore the emitter states are not modified by the field mode.

To actually generate polaritonic states it is necessary to confine the field modes. The confinement of the modes leads to a decrease of the quantization volume V and to a consequent increase of the coupling strength g_c, according to eq. (4.3). The most common, but not unique [40], way to confine the electromagnetic field is with a cavity of the appropriate size. Actually, the cavity is fundamental for two reasons: i) with the cavity it is possible to select and produce one or few modes of the quantized electromagnetic field with the desired properties [1] and ii) the small quantization volume associated with the cavity increases the coupling strength, leading to the formation of polaritons that can be measured distinctly.

As reported in fig. 4.1(panels a-b) mainly two types of cavities are used. Plasmonic cavities can reach the nanometric scale and are used for single-or few-molecules experiments [42]. Fabry-Perot cavities are larger than plasmonic cavities and used for experiments in the collective coupling regime, that is many molecules coupled to one or more modes [43]. Figure 4.1(panels c-d) presents a scheme of the hybridization of the emitter and cavity energy levels. As occurs between atomic orbitals or between electronic states in dimers, the energy levels of the field and of the emitter hybridize, generating at least a lower polariton (LP) and an upper polariton (UP). The splitting of a single emitter level into two polaritons clearly changes the absorption spectrum, a single absorption peak is divided in two (panels e-f).

From this discussion it emerges that when dealing with polaritons the main variable is the coupling strength. Based on the g_c parameter and the experimental setup the coupling can be classified as weak, $g_c\sqrt{N}/\gamma < 1$, or strong, $g_c\sqrt{N}/\gamma > 1$,being γ the loss rate of the molecule or the cavity. A further classification can be done considering also the frequency ω of the cavity mode. In the ultrastrong coupling regime $0.1 < g_c\sqrt{N}/\omega < 1$, while in the deep strong coupling regime $g_c\sqrt{N}/\omega > 1$ [44].

While the Jaynes-Cummings and Tavis-Cummings models are the cornerstone upon which the modern theory of polaritons has been built, they shows some shortcomings in the strong coupling regime [45]. The application of the Jaynes-Cummings model leads to an unstable light-matter system, that is there is no proper description of the ground state. There is the necessity of a new model.

In polaritonic chemistry the popular models rely on the Pauli-Fierz Hamiltonian, which will be briefly introduced in section 4.1.1.

4.1.1 The Pauli-Fierz Hamiltonian

Traditional cavity QED models like the Jaynes-Cummings o the Tavis-Cummings rely on the single mode approximation and on the long wavelength approximation. The long wavelength approximation holds if the object under consideration is much smaller than the wavelength of the cavity mode, in polaritonic chemistry this is often

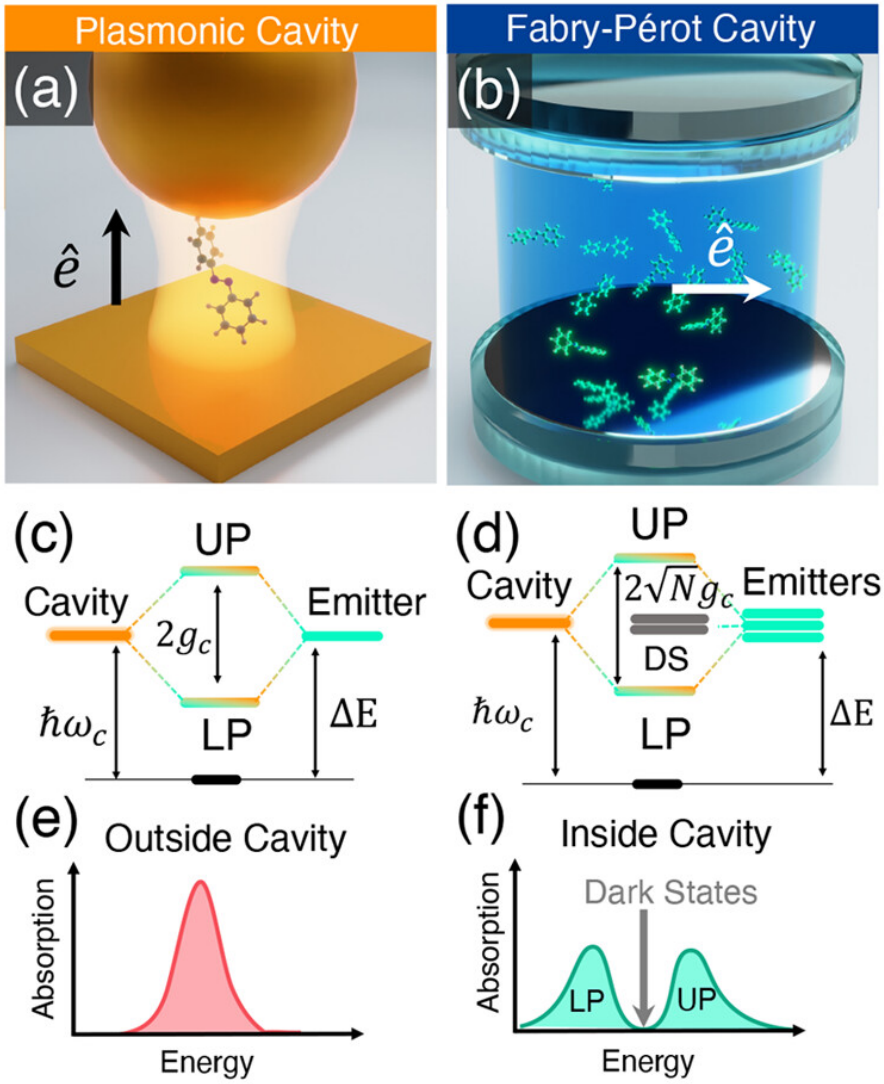

Figure 4.1: Schematic illustrations of commonly used optical cavities in molecular polariton research. (a) Plasmonic cavity: A single molecule coupled to a plasmonic field. (b) Fabry–Pérot cavity: An ensemble of molecules coupled to a quantized vacuum radiation field. In both panels, the arrows and ê indicate the dominant cavity field polarization directions that matter couple to. Panels (c) and (d) depict the polariton spectrum for a single molecule coupled to cavity (depicted in panel a) and N molecules collectively coupled to a cavity (depicted in panel b). (e) Molecular absorption, and (f) the Polariton absorption. For a single molecule case, there is no dark state (see panel c), but for the N-molecule collective coupling case, one can observe the dark states due to their nearly zero transition dipole. Reproduced from [41] in compliance to the CC-BY 4.0 license.

true. The single mode approximation, as anticipated above discussing Fabry-Perot cavities, does not describe the experiments in the collective regime, however it is convenient to build the theory considering a single cavity mode and then extend it later.

Under the single mode approximation, the long wavelength approximation and after the choice of the Coulomb gauge the light-matter Hamiltonian reads [1, 46–48]

$$\hat{H}_{p\cdot A} = \sum_j \frac{1}{2m_j}\left(\hat{\mathbf{p}}_j - z_j\hat{\mathbf{A}}\right)^2 + \hat{V} + \hat{H}_{ph} \tag{4.4}$$

This is often called the minimal coupling or the "$p \cdot A$" Hamiltonian. The index j runs over the number of particles. $\hat{\mathbf{p}}_j = -i\hbar\nabla_j$ is the momentum operator, z_j is the charge of the j-th particle, $\hat{A}$ is the quantized vector potential operator, $\hat{V}$ describes the potential terms between charged particles and $\hat{H}_{ph}$ is the photon Hamiltonian. In eq. (4.4) the kinetic energy of the nuclei is discarded.

The photon Hamiltonian is defined as in the Jaynes-Cummings model

$$\hat{H}_{ph} = \hbar\omega_c\left(\hat{a}^\dagger\hat{a} + \frac{1}{2}\right) = \frac{1}{2}\left(\hat{p}_c^2 + \omega_c^2\hat{q}_c^2\right) \tag{4.5}$$

where

$$\hat{q}_c = \sqrt{\frac{\hbar}{2\omega_c}}(\hat{a}^\dagger + \hat{a}) \tag{4.6}$$

and

$$\hat{p}_c = i\sqrt{\frac{\hbar\omega_c}{2}}(\hat{a}^\dagger - \hat{a}) \tag{4.7}$$

$\hat{q}_c$ and $\hat{p}_c$ are called the photonic coordinate and momentum operators, respectively. Lastly the vector potential operator is defined, under the single mode approximation,

$$\hat{\mathbf{A}} = \mathbf{A}_0(\hat{a}^\dagger + \hat{a}) \tag{4.8}$$

$$\mathbf{A}_0 = \sqrt{\frac{\hbar}{2\omega_c\varepsilon_0 V}}\hat{\mathbf{e}} \tag{4.9}$$

The "$p \cdot A$" Hamiltonian is the starting point for the derivation of Pauli-Fierz Hamiltonian. For quantum chemical application it is desirable to work with a real Hamiltonian [49], the "$p \cdot A$" Hamiltonian is complex and to obtain the real Pauli-Fierz Hamiltonian it is sufficient to apply two unitary transformations.

The first is the Power-Zienau-Wooley (PZW) gauge transformation [50, 51], associated with the operator

$$\hat{U} = \exp\left[-\frac{i}{\hbar}\hat{\boldsymbol{\mu}}\cdot\hat{\mathbf{A}}\right] \tag{4.10}$$

in which $\hat{\boldsymbol{\mu}}$ is the usual dipole moment operator $\hat{\boldsymbol{\mu}} = \sum_j z_j\hat{\mathbf{x}}_j$.

The application of the PZW unitary transformation, eq. (4.10), to the the "$p \cdot A$" Hamiltonian, eq. (4.4), leads to the Hamiltonian in the so-called "dipole gauge", "length gauge" or $d \cdot E$ form [50–53].

$$\hat{H}_{d\cdot E} = \hat{U}\hat{H}_{p\cdot A}\hat{U}^{\dagger} = \hat{H}_{el} + \hat{H}_{ph} + i\omega_c\hat{\boldsymbol{\mu}}\cdot\mathbf{A}_0(\hat{a}^{\dagger} - \hat{a}) + \frac{\omega_c}{\hbar}(\hat{\boldsymbol{\mu}}\cdot\mathbf{A}_0)^2 \tag{4.11}$$

$\hat{H}_{el}$ is the usual electronic Hamiltonian that describes the molecular electronic structure.

While it is important to recall that an unitary transformation does not change the underlying physics, the PZW transformation leads to new terms that help to clarify the nature of the model.

In the dipole gauge the Hamiltonian takes a decoupled form, easier to interpret. The electronic Hamiltonian refers to the isolated molecule, the photonic Hamiltonian describes a single photon in free space and the last two terms include the light-matter interactions. The expectation value of the $i\omega_c\hat{\boldsymbol{\mu}}\cdot\mathbf{A}_0(\hat{a}^{\dagger} - \hat{a})$ term is non-zero only if the integration is carried out with two functions that are associated to different photon numbers, mixing the electronic and photonic degrees of freedom.

The last term is commonly called dipole self-energy, $\frac{\omega_c}{\hbar}(\hat{\boldsymbol{\mu}}\cdot\mathbf{A}_0)^2$. The dipole self-energy arises from the polarization of the quantum field due to the permanent molecular dipole, and the consequent interaction between the polarized mode and the permanent dipole [41]. Neglecting the dipole self energy term leads to the loss of the gauge invariance and may lead to numerical error in the strong, ultrastrong and deep strong coupling regimes [41], in particular it may lead to an unstable ground state [45].

The $\hat{H}_{d\cdot E}$ Hamiltonian offers some valuable insights into the physics of light-matter interactions, nevertheless it still shows some complex terms. A second unitary transformation removes the complex terms and leads to the Pauli-Fierz Hamiltonian in the dipole gauge [45, 53, 54]. This time the unitary transformation operator is defined as

$$\hat{U}_0 = \exp\left[-i\frac{\pi}{2}\hat{a}^{\dagger}\hat{a}\right] \tag{4.12}$$

The application of eq. (4.12) to eq. (4.11) leads to the Pauli-Fierz Hamiltonian, cornerstone of molecular QED.

$$\hat{H}_{PF} = \hat{U}\hat{H}_{d\cdot E}\hat{U}^{\dagger} = \hat{H}_{el} + \hat{H}_{ph} + \omega_c\hat{\boldsymbol{\mu}}\cdot\mathbf{A}_0(\hat{a}^{\dagger} + \hat{a}) + \frac{\omega_c}{\hbar}(\hat{\boldsymbol{\mu}}\cdot\mathbf{A}_0)^2 \tag{4.13}$$

The Pauli-Fierz Hamiltonian is real. The absence of complex terms eases the numerical procedures and the implementation in traditional quantum chemical codes [41].

Before delving into the procedures to solve the Pauli-Fierz Hamiltonian it is worth aligning the notation used until now to the one widely used in polaritonic chemistry literature [53–56].

The preferred way to define the Pauli-Fierz Hamiltonian is the following:

$$\hat{H}_{PF} = \hat{H}_{el} + \hbar\omega_c\left(\hat{a}^{\dagger}\hat{a} + \frac{1}{2}\right) + \sqrt{\frac{\omega_c}{2}}\lambda(\hat{\boldsymbol{\mu}}\cdot\hat{\mathbf{e}})(\hat{a}^{\dagger} + \hat{a}) + \frac{\lambda^2}{2\hbar}(\hat{\boldsymbol{\mu}}\cdot\hat{\mathbf{e}})^2 \tag{4.14}$$

the coupling strength is now defined by the parameter λ

$$\lambda = \sqrt{2\omega_c}\mathbf{A}_0 = \sqrt{\frac{\hbar}{\varepsilon_0 V}}\hat{\mathbf{e}} \tag{4.15}$$

The Pauli-Fierz Hamiltonian maintains the structure (and the gauge) of the "$d \cdot E$" Hamiltonian: the first term describes the isolated molecule, the second the isolated quantum of the field, the third the field-matter interaction and the fourth the dipole self energy.

Equation (4.14) probably is the central equation of this chapter, since its solution provide an accurate description of a polaritonic system.

The focus now shifts from how to define a correct Hamiltonian to how to solve the Hamiltonian. There are two popular approaches: i) solve the electronic Hamiltonian via an electronic structure package and then analytically solve the Pauli-Fierz Hamiltonian through a coupled molecular-photonic basis, ii) solve directly the Pauli-Fierz Hamiltonian including its terms in the electronic structure methods. An excellent review that treats in detail the state of the art of the computational methods is [41].

In the following sections some details regarding two of the various available methods will be introduced, along with a consequent application to real molecules. Section 4.1.2 presents an analytical method, section 4.1.3 presents a self consistent field method.

4.1.2 Analytical Solution

In this section it is briefly presented one of the simplest approaches to solve the Pauli-Fierz Hamiltonian. It resorts to a basis that mixes the molecular and photonic degrees of freedom and that is "frozen", not updated through a SCF procedure. It is often called adiabatic, frozen basis or parametrized QED approach [41, 57, 58].

The first step is the definition of the basis. In this approach the Pauli-Fierz Hamiltonian is represented in the adiabatic-Fock basis defined as

$$|\psi_\alpha(R), n\rangle = |\psi_\alpha(R)\rangle \otimes |n\rangle \tag{4.16}$$

where $|\psi_\alpha(R)\rangle$ is an adiabatic electronic state (in this case, a single or a combination of Slater determinants) and $|n\rangle$ is a Fock state, eigenfunction of the photon Hamiltonian. The Pauli-Fierz Hamiltonian depends parametrically on the nuclear coordinates R, and so does the electronic state $|\psi_\alpha(R)\rangle$. Each Fock state is associated with a well-defined number (n) of photons.

The minimal basis is defined with two electronic states and two photonic states; a ground state $|g\rangle$, an excited state $|e\rangle$, the vacuum quantized field $|0\rangle$ and a single photon $|1\rangle$. The minimal basis counts four elements

$$|g, 0\rangle \tag{4.17}$$
$$|e, 0\rangle \tag{4.18}$$
$$|g, 1\rangle \tag{4.19}$$
$$|e, 1\rangle \tag{4.20}$$

After the definition of the basis it is necessary to compute the matrix elements associated with eq. (4.14). Under the choice of the frozen basis the matrix elements read [56, 59]

$$
\begin{aligned}
(\hat{H}_{PF})_{\alpha\beta,nm} &= \langle \psi_\alpha(R), n | \, \hat{H}_{PF} \, | \psi_\beta(R), m \rangle \\
&= \left[E_\beta(R) + \hbar\omega_c \left(m + \frac{1}{2} \right) \right] \delta_{\alpha\beta}\delta_{nm} + \\
&+ \sqrt{\frac{\omega_c}{2}} \lambda \left(\boldsymbol{\mu}_{\alpha\beta}(R) \cdot \hat{\mathbf{e}} \right) \left(\sqrt{m}\delta_{n,m-1} + \sqrt{m+1}\delta_{n,m+1} \right) + \\
&+ \frac{1}{2\hbar} \lambda^2 \sum_{\gamma=1}^{N} \left(\boldsymbol{\mu}_{\alpha\gamma}(R) \cdot \hat{\mathbf{e}} \right) \left(\boldsymbol{\mu}_{\gamma\beta}(R) \cdot \hat{\mathbf{e}} \right) \delta_{nm}
\end{aligned}
\tag{4.21}
$$

The N electronic states are labeled by $\{\alpha, \beta, \gamma\}$ and $\{n, m\}$ label the photon number states. It is worth recalling that if $\alpha \neq \beta$ then $\boldsymbol{\mu}_{\alpha\beta}$ is the transition dipole moment, if $\alpha = \beta$ then $\boldsymbol{\mu}_{\alpha\beta}$ is the permanent dipole moment.

The diagonalization of the Hamiltonian results in the polaritonic states and the associated energies. The polaritonic states can be expressed as a linear combination of the Kronecker product basis functions as

$$
|\Psi_i(R)\rangle = \sum_{\alpha,n} c^i_{\alpha,n} \, |\psi_\alpha(R), n\rangle \tag{4.22}
$$

The strength of the parametrized QED approach is its simplicity. The energies of the electronic states and the dipole moment can be computed with any electronic structure method and software, then the construction of the Hamiltonian matrix and its diagonalization are straightforward. The solution is exact in the infinite basis limit, excluding the errors due to the electronic structure method. However the number of electronic and photonic states needed for the convergence of the solution cannot be defined a priori, and must be tuned by the user [41].

4.1.3 SCF Solution

The second family of methods is based on a self-consistent field solution. As the traditional electronic Hamiltonian led to a variety of electronic structure methods, in the recent years several approaches have been presented to solve the Pauli-Fierz Hamiltoninan in a SCF manner. Most of them leverage on the concepts introduced in traditional electronic structure theory, adapted to the QED problem. This led to methods like QED-HF, QED-CI, QED-CASSCF, QED-CC and QED-DFT, just to name a few. These methods have been extended also the calculation of excited states [60–68].

In this section the focus is only on the simplest of these method, the quantum electrodynamics Hartree-Fock (QED-HF), which will be applied in section 4.2.1. From now on the treatment of the QED-HF method is mainly taken from [65].

As the canonical HF method, the QED-HF is limited to the ground state. The main difference with respect to the parametrized QED method is the solution is iteratively computed and updated, in order to minimize the energy. The QED-HF method requires the choice of a basis set, whether gaussian orbitals and plane waves, as the canonical HF.

The main conceptual task is to extend the usual electronic wavefunction to include the photonic degrees of freedom. The way to introduce the photonic degrees of freedom is not unique, but the popular choice is to use coherent states [69]. The choice of coherent states is motivated by their algebraic simplicity and by physical intuition, they are the closest states to a classical plane wave allowed by quantum mechanics.

Under these assumptions the polaritonic ground state ansatz, that will be optimized through the SCF procedure, is

$$\left|\Phi_0^{pl}\right\rangle = \left|\Phi^{HF}\right\rangle \otimes \sum_n c_n \frac{(a^\dagger)^n}{\sqrt{n!}} \left|0\right\rangle \tag{4.23}$$

The ground state ansatz is a product state between the HF ground state (which is a Slater determinant of molecular spin orbitals, hence the need of a traditional basis set) and a coherent state of a single cavity mode. In eq. (4.23) $|0\rangle$ is the photon vacuum state of the photonic Hamiltonian (eq. (4.5)) and c_n are the expansion coefficients. In this context n is the number of photons in the mode.

At this point it should not be surprising that the next step is a unitary transformation on the Pauli-Fierz Hamiltonian [61]. In this case the transformation is

$$\hat{U}_Z = e^{Z\hat{a}^\dagger - Z^*\hat{a}} \tag{4.24}$$

where

$$Z = -\frac{\left\langle\Phi^{HF}\right| \lambda \cdot \hat{\boldsymbol{\mu}} \left|\Phi^{HF}\right\rangle}{\sqrt{2\omega_c}} \tag{4.25}$$

After the unitary transformation the Pauli-Fierz Hamiltonian reads

$$\hat{H}_{PF}^Z = \hat{H}_{el} + \hbar\omega_c \left(\hat{a}^\dagger\hat{a} + \frac{1}{2}\right) + \sqrt{\frac{w_c}{2}}(\lambda \cdot \Delta\hat{\boldsymbol{\mu}})(\hat{a}^\dagger + \hat{a}) + \frac{1}{2\hbar}(\lambda \cdot \Delta\hat{\boldsymbol{\mu}})^2 \tag{4.26}$$

with $\Delta\hat{\boldsymbol{\mu}} = \hat{\boldsymbol{\mu}} - \left\langle\Phi^{HF}\right| \hat{\boldsymbol{\mu}} \left|\Phi^{HF}\right\rangle$, which describes how the molecular dipole fluctuates after the coupling with the field. At a first glance one of the difficult tasks is integrating the light-matter interaction term $\hat{a}^\dagger + \hat{a}$ in a way consistent with the gaussian basis set. However, as it is presented in [65] and later applied, the QED-HF method is applied with a simplified ansatz, considering only the vacuum field.

$$\left|\Phi_0^{pl}\right\rangle = \left|\Phi^{HF}\right\rangle \otimes \left|0\right\rangle \tag{4.27}$$

This choice leads to a simplified Fock operator

$$F_{pq,nm} = F_{pq}^{el}\delta_{nm} - \frac{\delta_{nm}}{2}\left[\sum_i^{N_o}(\lambda \cdot \boldsymbol{\mu}_{pi})(\lambda \cdot \boldsymbol{\mu}_{iq}) - \sum_j^{N_v}(\lambda \cdot \boldsymbol{\mu}_{pj})(\lambda \cdot \boldsymbol{\mu}_{jq})\right] \tag{4.28}$$

Here the p, q indexes run over the molecular orbitals, N_o is the number of occupied orbitals, N_v the number of virtual orbitals and n, m label the photonic number

basis states (in this case it is trivial, since there is just only one photonic state). F_{pq}^{el} is the electronic Fock operator. Lastly, the QED-HF energy can be written as

$$E_{QED-HF} = E_{HF} + \frac{1}{2}\left\langle \Phi^{HF} \right| (\lambda \cdot \delta\hat{\boldsymbol{\mu}})^2 \left| \Phi^{HF} \right\rangle = E_{HF} + \sum_{ij} (\lambda \cdot \boldsymbol{\mu}_{ij})^2 \tag{4.29}$$

The variational minimization of the QED-HF energy can then be carried out with any of the traditional techniques, remembering to update the Z value after each iteration.

With respect to the parametrized QED method, the QED-HF offers a faster calculation of the polaritonic ground state, since there is no need to explicitly compute several electronic excited states, however the QED-HF is limited to one polaritonic state, while the parametrized QED method can compute many polaritonic states.

4.2 Applications

In this sections both the methods outlined in section 4.1 are applied to real chemical systems. Several classes of systems and processes have been studied under strong coupling conditions [70–73], however the focus is on a class of molecules that did not receive as much attention: polyenes.

Polyenes served as a prototypical class of molecules for the development of fundamental models in theoretical chemistry, such as frontier orbitals, Woodward-Hoffmann rules and Hückel model [74–77]. Even a simple particle-in-a-box model can be applied, with some limitations, to predict the electronic properties of the polyenes [78].

Polyenes are a popular class of molecules not only due to their simplicity but also for the wide range of applications. They are involved in various natural processes, such as vision and antibiotic functions [79–81]. In the last twenty years they have been used in organic electronics, from the fabrication of sensors to light-emitting diodes [82, 83]. The electric field, whether locally generated by the enzymatic environment during the natural processes or externally produced in the organic electronic applications, plays a central role.

It is tempting to extend the current knowledge to the light-matter strong coupling scenario. In the following subsections the simplest conjugated polyenes, butadiene and hexatriene, are studied under strong coupling conditions. In both cases the investigation focused on the isomerization. For the butadiene it has been applied the QED-HF method, for the hexatriene the parametrized QED method.

4.2.1 Effect of Strong Coupling on the Ground State: Butadiene

From the Pauli-Fierz Hamiltonian (eq. (4.14)) it emerges that two parameters influence the effect of the cavity on a molecular system: the coupling strength λ and molecular orientation. The higher the coupling strength and the higher the effect of the cavity mode on the electronic structure. The effect of the molecular orientation is more elusive. When considering the formation of the polaritons at least three

dipole moments must be taken into account: the permanent dipole of the ground state, the permanent dipole of the excited state and the transition dipole moment.

To isolate the role of a single dipole moment on the energy, the investigation is limited to the effect of the vacuum field on the ground state. The ground state inside the cavity can be studied with the QED-HF method and the only dipole moment that plays a role in the Hamiltonian is the permanent dipole moment of the ground state (see eq. (4.26)).

The process under examination is the rotation around the single C-C bond of 1,3-butadiene, which leads to a s-trans to s-cis isomerization. Figure 4.2 shows a few geometries that describe the process and the molecular orientation.

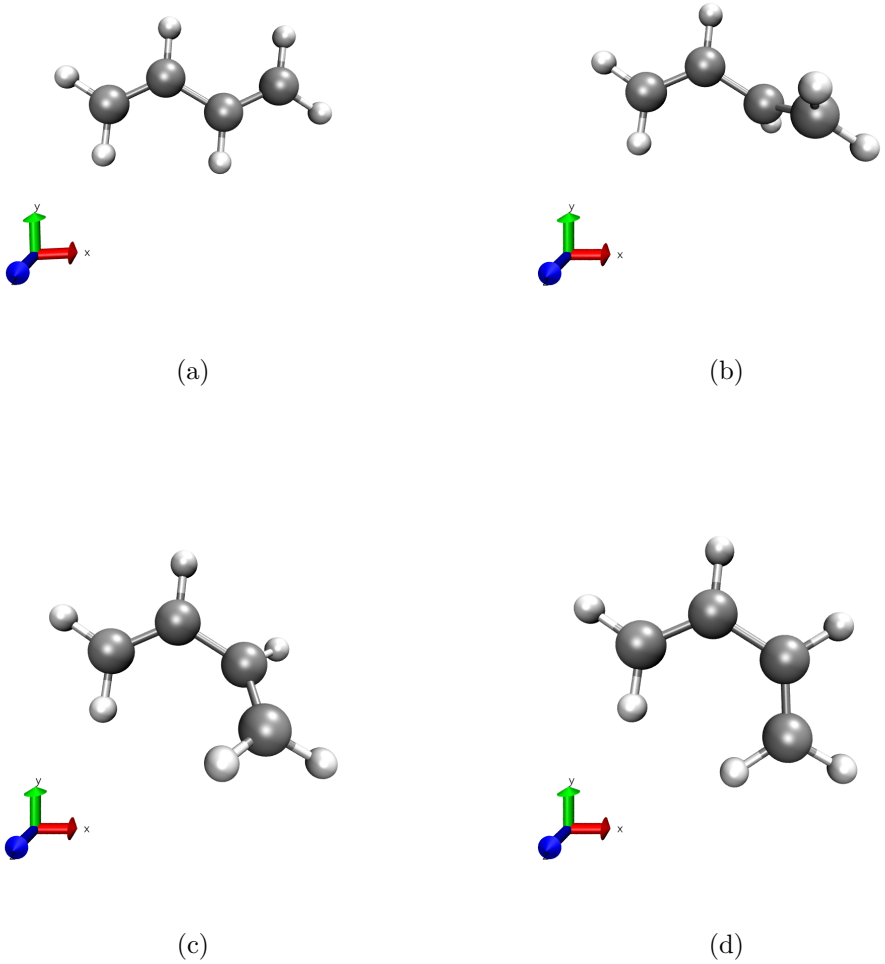

(a) (b)

(c) (d)

Figure 4.2: Selected conformations of 1,3-butadiene along the isomerization process. The axes represent the molecular orientation, red: x, green: y, blue: z

The isomerization is modeled varying the central dihedral angle and freezing all the remaining internal degrees of freedom. During the generation of the geometries it is fundamental to maintain the molecular orientation, otherwise the effect of the

cavity would not be comparable along the reaction coordinate. The procedure used here can be found at ref. [84]. For instance, it is not advisable to use a relaxed scan as it is printed by the common quantum chemical programs. The optimization is usually carried in internal coordinates, and the molecular orientation may change during the process. Experimentally, there are several techniques to control the molecular orientation [42, 85, 86].

The cavity under consideration is a bimodal cavity, for which the effective coupling strength can be computed as $\lambda_{eff} = \sqrt{\sum_{\alpha}^{2} \lambda_{\alpha}^{2}}$. Here, the effect is evaluated on a single molecule, discarding the role of the concentration on the coupling strength.

The effect of the cavity has been compared to an equivalent classical electric field. To do so, the coupling strength is related to the one-photon field amplitude (E) through

$$E = \lambda_{eff} \sqrt{\frac{\omega}{2}} \tag{4.30}$$

where it is assumed that the field is not position-dependent. The application of eq. (4.30) assumes the presence of a single classical electric field mode associated with the effective coupling strength, under this assumption when computing the amplitude of the associated field it follows that the two cavity modes are characterized by the same frequency ω.

Firstly, the molecular geometry has been optimized and then the central dihedral has been modified fixing all the remaining degrees of freedom. For each geometry produced scanning the central dihedral angle it has been performed a QED-HF simulation and a traditional HF simulation under the effect of the classical electric field. The calculations in the cavity environment were performed with the eT program (version 1.9.11)[87], the calculations with the classical field were carried out with the Gaussian 16 program [88]. All calculations were performed with the 6-31G** basis set [89–93].

The energy along the isomerization pathway in the cavity is calculated for several λ_{α}, from 0.01 to 0.04 in steps of 0.01 (in atomic units). For the calculations with the classical electric field the classical amplitude associated with the cavity mode has been computed with eq. (4.30), using $\omega = 0.01$ a.u. This frequency is associated with a wavelength of roughly 725 nm. Such a value is far from any electronic excitation. The associated values of the electric field range from 0.001 to 0.004 in steps of 0.001 (in atomic units), that is from 0.514 V/nm to 2.057 V/nm.

The conformational isomerization of 1,3-butadiene occurs via a rotation about the central C-C bond. Starting from the s-trans conformer, where by convention the torsional angle is set to 0°, the rotation leads to a transition state with the largest energy barrier, or TS1, then to the gauche conformer. The interconversion between the two gauche conformers occurs via a lower energy transition state, or TS2, which is the planar s-cis conformer[94]. At the s-cis conformer the angle is set to 180°.

Figure 4.3 reports the isomerization pathways for different directions of the cavity mode and the classical field. The molecular orientation is the one depicted in fig. 4.2. From the graphs it appears that the molecular orientation plays a central role, allowing a control on both the barriers. In fig. 4.3a the cavity mode is along

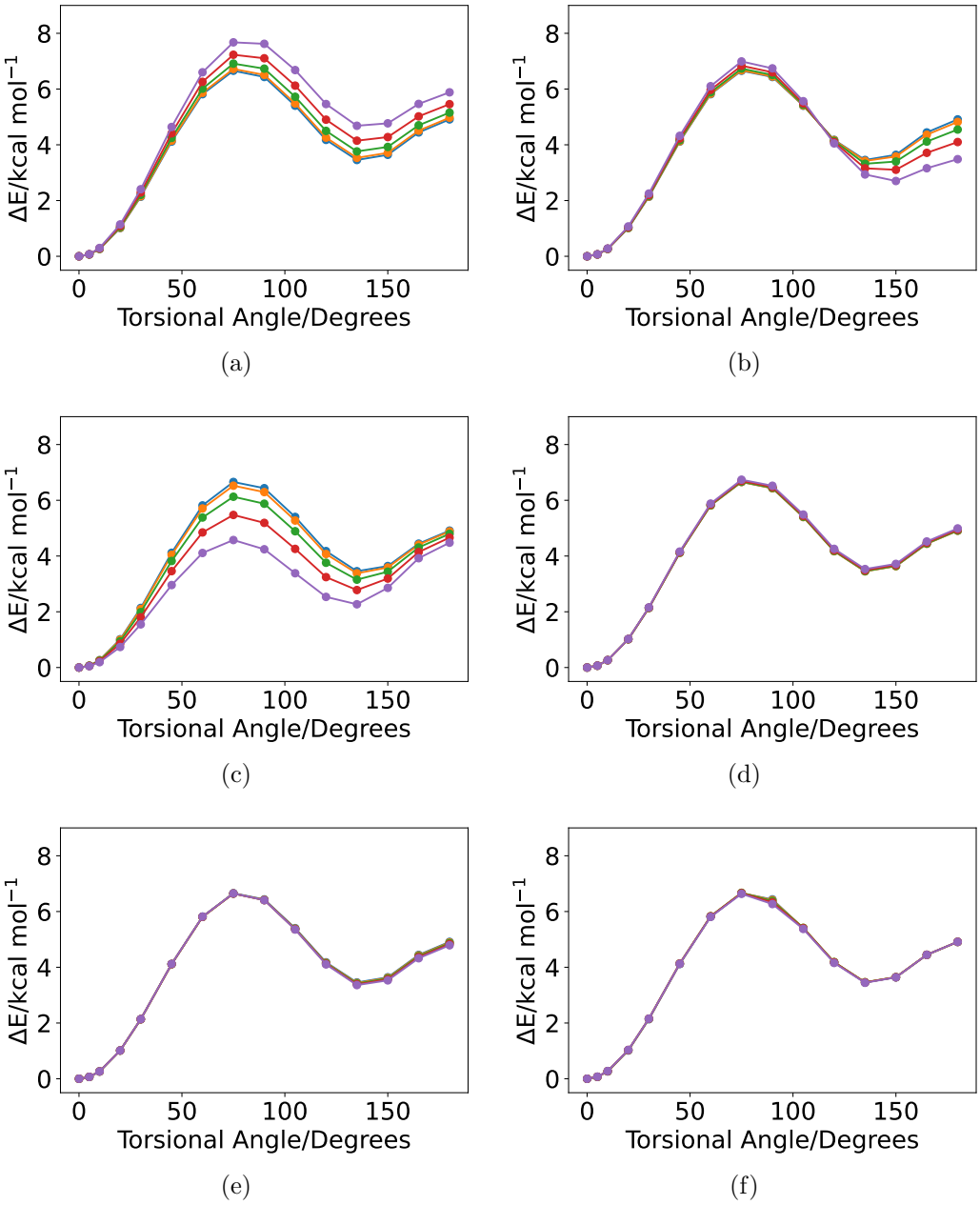

Figure 4.3: Potential energy curves of the torsion of the central bond of butadiene. a) cavity modes, x-direction, b) cavity modes, y-direction, c) cavity modes, z-direction, d) classical field, x-direction, e) classical field, y-direction, f) classical field, z-direction. Blue: $\lambda = 0.0/E = 0.0$ (free space), orange:$\lambda = 0.01$ a.u.$= 8.73 \cdot 10^{18} F^{-\frac{1}{2}} m^{-1}/E = 0.001$ a.u.$= 0.514$ V/nm, green:$\lambda = 0.02$ a.u.$= 1.77 \cdot 10^{19} F^{-\frac{1}{2}} m^{-1}/E = 0.002$ a.u.$= 1.028$ V/nm, red:$\lambda = 0.03$ a.u.$= 2.62 \cdot 10^{19} F^{-\frac{1}{2}} m^{-1}/E = 0.003$ a.u.$= 1.542$ V/nm, purple:$\lambda = 0.04$ a.u.$= 3.49 \cdot 10^{19} F^{-\frac{1}{2}} m^{-1}/E = 0.004$ a.u.$= 2.057$ V/nm

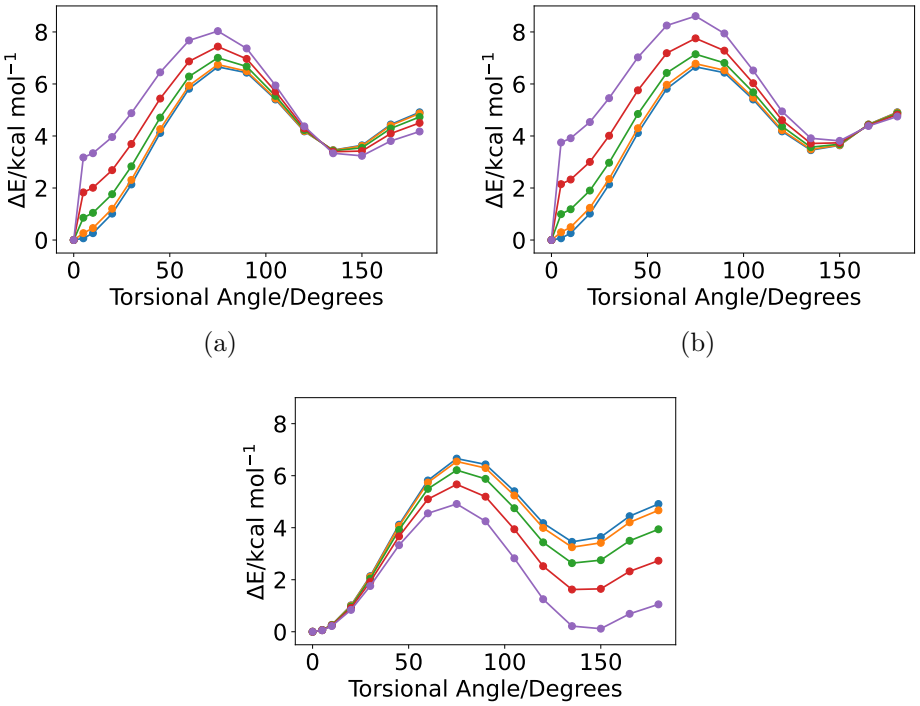

Figure 4.4: Potential energy curves of the torsion of the central bond of butadiene inside the cavity. a) the direction of the molecular dipole moment vector, b) the direction of the molecular dipole moment vector, at the origin, the field is aligned along the eigenvector of the polarizability tensor associated with the second lowest eigenvalue, c) the direction of the molecular dipole moment vector, at the origin, the field is aligned along the eigenvector of the polarizability tensor associated with the lowest eigenvalue. Blue: $\lambda = 0.0/E = 0.0$ (free space), orange:$\lambda = 0.01$ a.u.$= 8.73 \cdot 10^{18} F^{-\frac{1}{2}} m^{-1}/E = 0.001$ a.u.$= 0.514$ V/nm, green:$\lambda = 0.02$ a.u.$= 1.77 \cdot 10^{19} F^{-\frac{1}{2}} m^{-1}/E = 0.002$ a.u.$= 1.028$ V/nm, red:$\lambda = 0.03$ a.u.$= 2.62 \cdot 10^{19} F^{-\frac{1}{2}} m^{-1}/E = 0.003$ a.u.$= 1.542$ V/nm, purple:$\lambda = 0.04$ a.u.$= 3.49 \cdot 10^{19} F^{-\frac{1}{2}} m^{-1}/E = 0.004$ a.u.$= 2.057$ V/nm

the X axis, the long molecular axis, and both the barriers are increased. In fig. 4.3b the cavity mode is along the Y axis, the gauche-TS2 barrier is lowered and the gauche region flattened. In fig. 4.3c the cavity mode is along the Z axis, and the s-trans/TS1 barrier is lowered while the gauche/TS2 barrier is increased. For each molecular orientation there is a different modification of the potential energy curve.

The calculations performed with the classical electric field led to no variation of the potential energy curves, highlighting the central role of the cavity and of the polariton formation.

From fig. 4.3 it emerges, that the orientation plays a central role. To further explore the effect of the orientation the molecule has been oriented such as its dipole moment vector is aligned with the cavity modes. This setup maximizes the light-matter coupling strength. However, in the s-trans conformation the molecular dipole moment is zero, therefore, just for the s-trans geometry, the molecule is

aligned with the eigenvectors of the polarizability matrix. Figure 4.4 shows how the isomerization changes under the maximal light-matter coupling strength.

It is interesting to notice that the maximal coupling strength does not correspond to the minimum energy path, and that the potential energy curve maintains its topology. In figs. 4.4a and 4.4b, there is a sudden increase of the potential energy as the cavity field is switched on close to the s-trans conformation. This conformation has a null dipole moment, at odds with all other geometrical structures along the isomerization pathway. It would be advisable to verify the presence of this effect using more refined quantum chemical method, however, as it stands, the polaritonic states of molecules with a null dipole moment can behave as on-off switches. The molecular orientation of fig. 4.4c is significant, both the barriers are reduced and the minima stabilized.

The effect of the cavity has been further studied considering two limit cases and computing the variation of the electron density due to the cavity. The two orientations considered are the ones of figs. 4.3a and 4.3c, in one case the mode is parallel to the long molecular axis, in one case it is perpendicular to it. The change between these orientations can increase or decrease the s-trans/TS1 barrier. The multi-panel fig. 4.5 shows the electron density variation that occurs upon switching on the coupling, it simply is the electron density difference between the molecule in the cavity and in free space. For sake of clarity, the value of λ_α was set to 0.04. The panels figs. 4.5a, 4.5c and 4.5e refer to the cavity mode along the X axis (s-trans, s-cis and TS1), and show that there is an increase of the electron density along the central C-C single bond, consistent with the predicted increase of of the isomerization barrier. Similarly the panels figs. 4.5b, 4.5d and 4.5f refer to the cavity mode along the Z axis and show a depletion of the electron density along the C-C bonds, and the consequent lowering of the barrier. Inspection showed that the π orbitals are not affected by the cavity. In free space the barrier is due to the breaking of the π-bonds, in the cavity there is also a strengthening or weakening of the underlying σ framework that affects the isomerization. This peculiar mechanism, to the best of the writer's knowledge, has no classical counterpart.

4.2.2 Formation of Polaritonic States: Hexatriene

This section extends the investigation of section 4.2.1, including the actual formation of polaritonic states in addition to the coupling with the vacuum field.

The system under consideration is trans 1,3,5-hexatriene. The choice of this system is due to its peculiar photophysics. In the Franck-Condon (FC) region the first two excited states are almost degenerate and a small geometrical distortion can lead to a conical intersection [95], affecting the deactivation of its excited states. The two low-lying excited states are $1^1B_u^+$ (bright) and $2^1A_g^-$ (dark). The energy and properties of the excited states have been object of various theoretical and experimental investigations (see [95] and references therein). Modelling the excited states can be troublesome due to the different nature of the excited state wavefunction. In the FC region the $1^1B_u^+$ is mainly described by a single HOMO/LUMO excitation, while the $2^1A_g^-$ by a linear combination of a single HOMO-1/LUMO excitation, a single HOMO/LUMO+1 excitation and a double HOMO^2/LUMO^2 excitation. The states have a different biradical/ionic character. To date, similar systems have

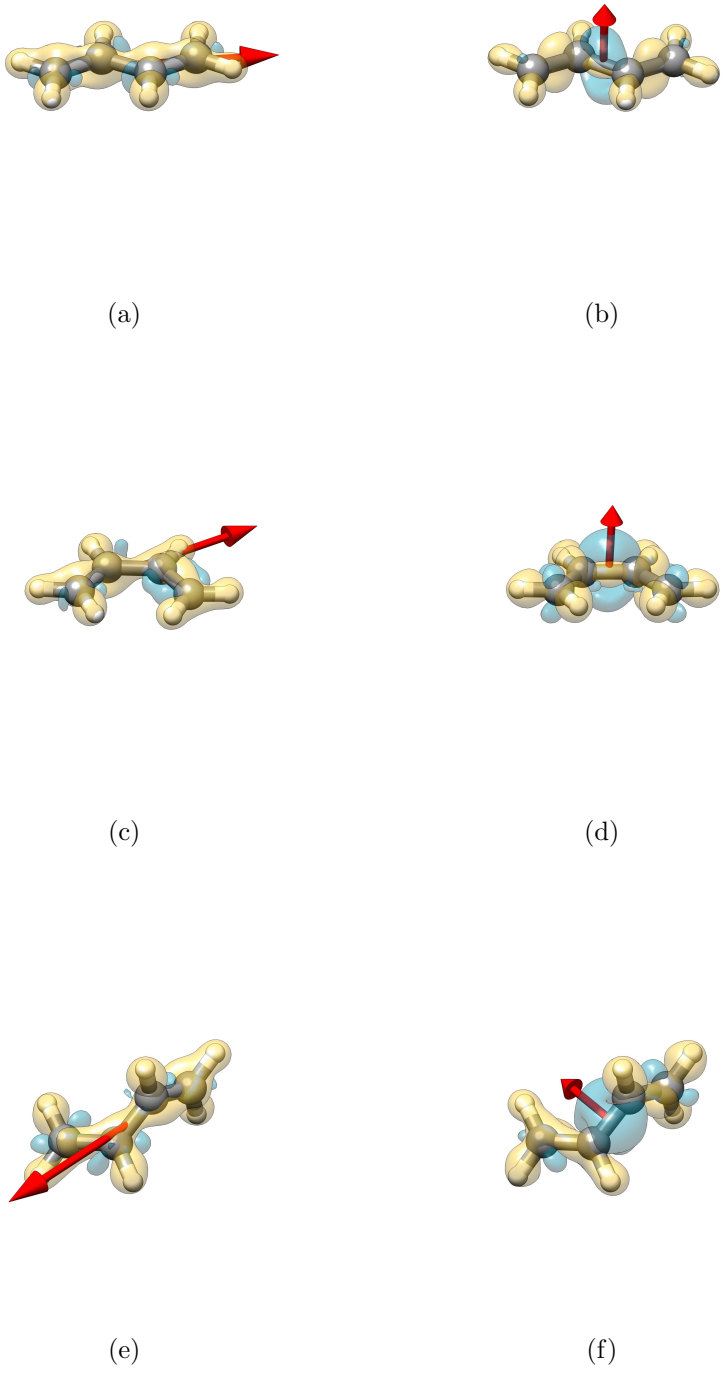

(a) (b)

(c) (d)

(e) (f)

Figure 4.5: Electron density variation upon switching on the coupling $\lambda = 0.04$ a.u.$= 3.49 \cdot 10^{19} F^{-\frac{1}{2}} m^{-1}$ for (top panels) the planar s-trans and s-cis conformations and (lower panels) TS1 and TS2. Yellow indicates regions of higher binding, blue of lower binding. The cavity modes are oriented along the arrow: a) as fig. 4.3a; b) as fig. 4.3a; c) as fig. 4.3c; d) as fig. 4.3c; e) as fig. 4.3a; f) as fig. 4.3c

been studied to chemical accuracy with the usage of quintuple-zeta basis sets and coupled cluster methods with the inclusion of quadruple excitations [96]. Beyond the complexity of the excites states in the FC region, it is of special interest the trans-to-cis isomerization of hexatriene, used as a model for the simulations of the vision process. The isomerization is promoted by the $1^1A_g^-/1^1B_u^+$ excitation, in fact the $1^1B_u^+$ potential energy surface is almost flat near the FC region and shows a minimum in correspondence of the $1^1A_g^-$ transition state. The molecule in the $1^1B_u^+$ state reaches the energy minimum geometry and then decays in the $1^1A_g^-$ TS, overcoming the reaction barrier.

This rich photophysics makes hexatriene the ideal candidate for a study in the strong light-matter coupling regime.

In this case the process under consideration is the rotation around the C3-C4 double bond, which leads to a trans-to-cis isomerization. The double bond torsion has been previously studied [97] and one of the difficulties is to correctly describe the biradical character after the π bond breaking. To do it was employed a UKS formalism coupled with the broken-symmetry procedure, at the TDA-PBE/6-311G** level [98, 99], which nicely approximates the excitation energies [100]. The geometry has been optimized in the FC region with the same level of theory and the isomerization is modeled changing only the central dihedral angle, fixing all the remaining degrees of freedom. All the calculations were performed with the ORCA 5.0.3 program system and the RIJCOSX approximation [101–106].

The central dihedral has been scanned from 0° (trans) to 180° (cis) with a 10° step. The molecular orientation is the same for all the geometries. The rotation around the central double C-C bond starts from the trans isomer and leads to a transition state (TS), then to the cis isomer. The stationary points of the isomerization curve are reported in fig. 4.6.

From the DFT calculations the energies of the states, the permanent dipoles and the transitions dipoles were extracted, in order to employ a parametrized QED method (section 4.1.2). The parametrized QED method allows the simulation of the polaritonic states, beyond the vacuum fluctuations effects described by the QED-HF method. The basis employed is made by the combinations of three electronic states (in the FC region: $1^1A_g^-$, $1^1B_u^+$ and $2^1A_g^-$) and two photonic levels (zero photons and one photon). Along the isomerization the nature of the electronic states changes and so does the symmetry label. The states used for the calculation of the polaritons are: the ground state singlet, the first bright excited singlet and the first dark excited singlet, these states are labeled, for simplicity, as $1A$, $1B$ and $2A$ respectively. The polaritons have been computed using a single mode cavity, with cavity frequency equal to the $1A/1B$ transition energy in the FC region, that is ω_c =5.23 eV=237.3 nm. The coupling strength λ is 0.01 a.u., which corresponds to a cavity volume of 18.6 nm^3. Here, the effect is evaluated on a single molecule, discarding the role of the concentration on the coupling strength. The investigation has been extended to the effect of the cavity detuning, varying ω_c by 5% of its original value.

Three electronic states and two photonic states form six polaritons, which are labeled according to their energy in the FC region as P0 (lowest energy), P1, P2, P3, P4, and P5 (highest energy). Throughout this section the resulting states will be called polaritonic states, regardless of the nature of the wavefunction, comments

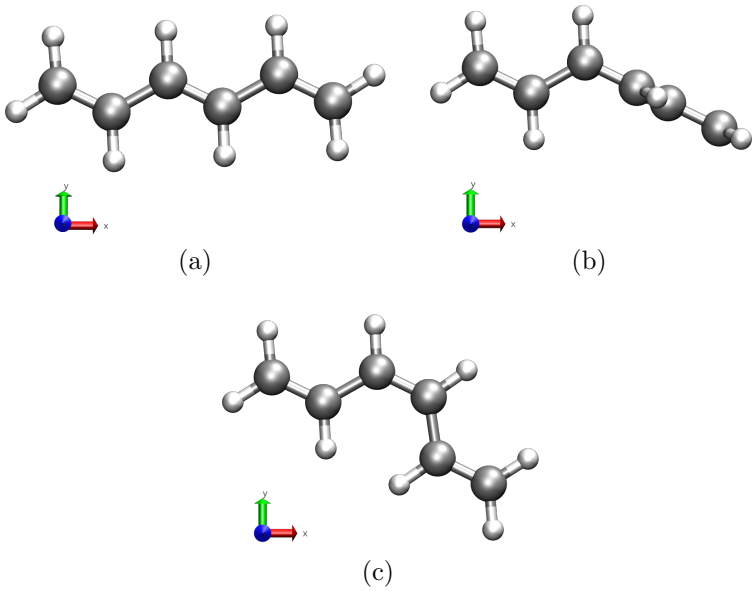

Figure 4.6: Stationary points along the isomerization potential energy curve of trans 1,3,5-hexatriene, (a) trans isomer, (b) transition state, (c) cis isomer. The axes represent the molecular orientation, red: x, green: y, blue: z

on the wavefunction will be reported when needed. Figure 4.7 shows the polaritonic potential energy curves along with the reference of the electronic states in free space. In fig. 4.7 the color is related to the highest combination coefficient of the polaritonic state wavefunction. If the highest combination coefficient is close to 1 the polaritonic state is close to one of the basis states and the dot color is darker, if the highest combination coefficient is close to $\frac{1}{\sqrt{2}}$ the polaritonic state is almost a 50/50 combination of two basis states, and the dot color is lighter.

Figure 4.7 shows that the P0 is similar in energy to the $1A$ state. The analysis of the wavefunction shows that the P0 polariton is always ruled by the $|1A, 0\rangle$ basis state and, thus, its energy is only shifted by a constant quantity with respect to the one of $1A$. From the same graph it emerges that the P4 and P5 states are high in energy with respect to the P0 state, it is necessary a far ultraviolet radiation to promote the transition to P4 and P5. For this reasons from here the discussion is limited to P1, P2 and P3.

Figure 4.8 shows the isomerization curves of P1, P2 and P3 computed using a value of ω_c resonant with the $1A/1B$ transition in the FC region and with a positive and negative detuning corresponding to the 5% of the resonant value.

As expected the basis states are highly mixed near the FC region, especially when the cavity mode is resonant with the transition (fig. 4.8a). The $2A$ state does not undergo a mixing and is solely shifted in energy, this is due to the zero transition dipole moment between the $1A$ and $2A$ state. Nevertheless the $1B/2A$ transition is allowed and therefore the $2A$ state must be included in the calculations to correctly compute the dipole self energy. The splitting between the P1 and P3 states is almost symmetrical with respect to P2 using a resonant frequency, with a negative detuning both the P1 and P3 states are stabilized and with a

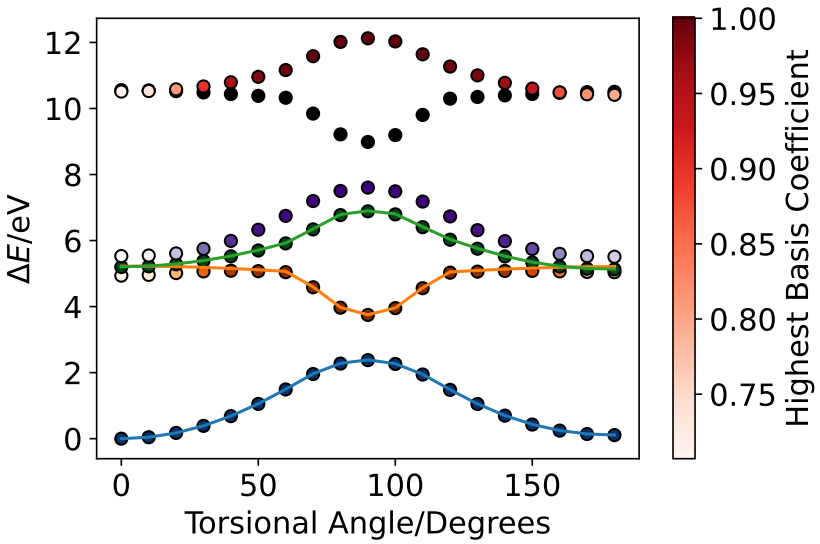

Figure 4.7: Polaritonic potential energy curves. The intensity of the color is related to the highest combination coefficient in the polaritonic state, the darker the color the closest is the polariton to one of the basis states. Blue: P0, orange: P1, green: P2, purple: P3, gray: P4, red: P5. Blue solid line: $1A$, orange solid line: $1B$, green solid line $2A$. ω_c =5.23 eV=237.3 nm, $\lambda = 0.01$ a.u.

positive detuning both the P1 and P3 states are destabilized. In the neighborhood of the TS the P1 and P3 states are almost exclusively described by the $|1B, 0\rangle$ and $|1A, 1\rangle$ basis states, due to the significant deviation of the cavity frequency from the $1A/1B$ transition and to the decrease of the transition dipole moment between the electronic states.

The stabilization of P1 eases the isomerization through the coupling-free gas-phase mechanism, requiring less energy to promote the P0/P1 excitation.

The cavity detuning has a significant impact on the P3 isomerization barrier. The resonant frequency leads to a 48 kcal/mol barrier (with respect to the 55 kcal/mol barrier of $1A$), the negatively detuned frequency to a 44 kcal/mol barrier and the positively detuned to a 50 kcal/mol barrier. As a further test, a 10% negative detuning leads to a 40 kcal/mol barrier, 15 kcal/mol lower than the one of $1A$. This suggests that the reactivity control goes beyond the usual resonant cavity frequency, an opportunely tuned cavity may lead to improved catalytic effects.

Similarly to traditional photocatalysis, polaritonic catalysis has seen a important growth due to experimental [18, 42, 107, 108] and theoretical advances [22, 109–112], but it is effective only if the polaritonic states can be populated in some way. The transitions between the P0 and the first excited polaritons have been analyzed. An estimate of the transition probability is the square of the transition dipole moment, reported along the entire reaction path. The vertical excitation energies have been computed in the FC region.

Figure 4.9 shows, on the left, the square of the transition dipole moment between the P0 polaritons and the first three excited polaritons, on the right a simulation of the absorption spectrum in which the excitation energies are computed in the FC region and the intensities are weighted on the square of the transition dipole

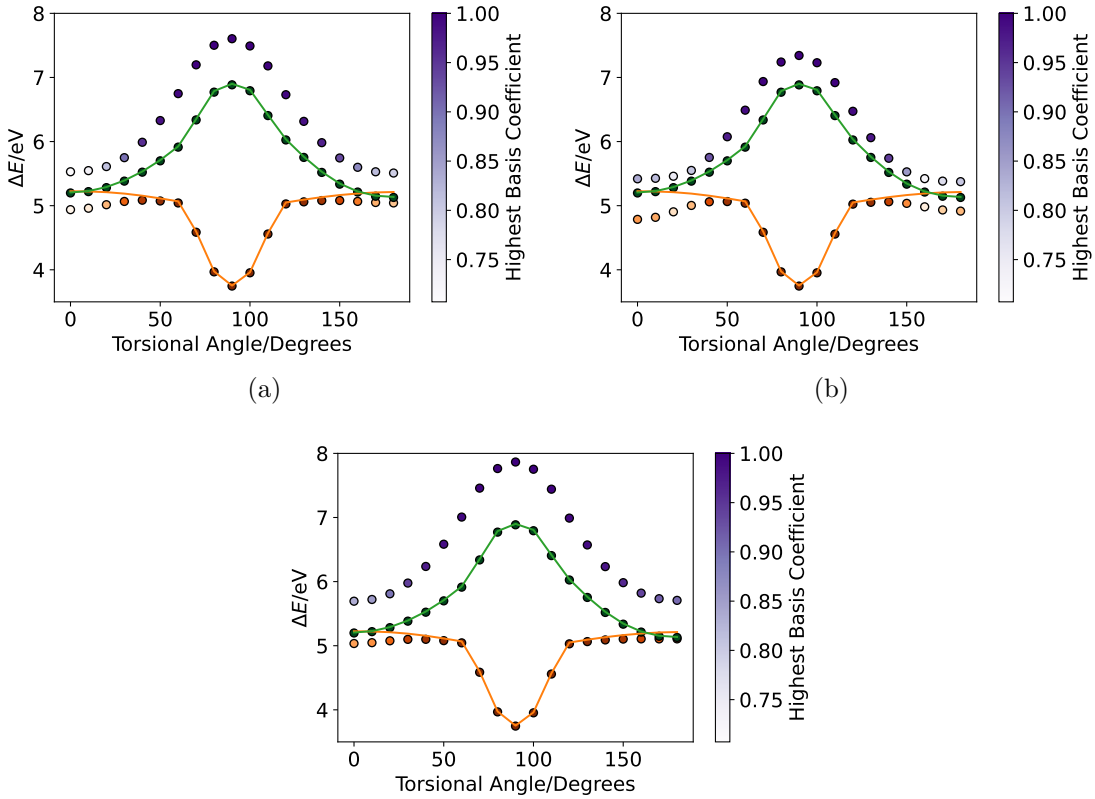

Figure 4.8: Polaritonic potential energy curves. The intensity of the color is related to the highest combination coefficient in the polaritonic state, the darker the color the closest is the polariton to one of the basis states. Orange: P1, green: P2, purple: P3. (a) ω_c =5.23 eV=237.3 nm resonant with the $1A/1B$ transition energy, (b) ω_c =4.96 eV=249.8 nm (negative detuning), (c) ω_c =5.49 eV=226.0 nm (positive detuning). $\lambda = 0.01$ a.u.

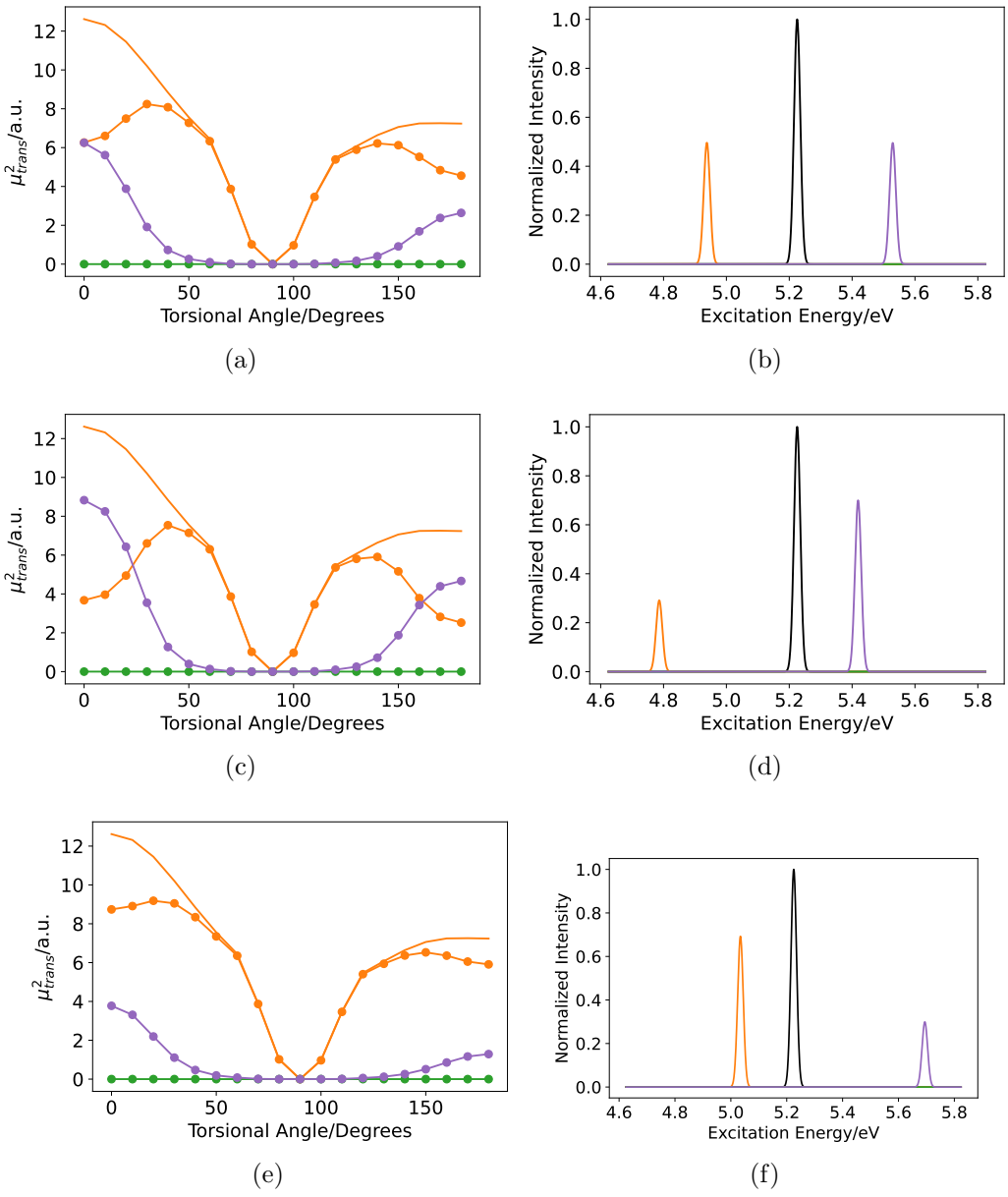

Figure 4.9: Left panels: transition dipole moments squared (μ^2_{trans}) between P0 and three excited polaritonic states, right panels: corresponding absorption spectrum from P0 in the FC region. Orange: P1, green: P2, purple: P3. In the left panels the solid orange line corresponds to $1B$. In the right panels the black line is the $1A/1B$ transition. (a-b) ω_c =5.23 eV=237.3 nm resonant with the $1A/1B$ transition energy, (c-d) ω_c =4.96 eV=249.8 nm (negative detuning), (e-f) ω_c =5.49 eV=226.0 nm (positive detuning). $\lambda = 0.01$ a.u.

moment. The peaks are fitted with an arbitrary gaussian shape.

If ω_c is resonant with the $1A/1B$ transition energy then the P0/P1 and P0/P3 transition probabilities are equal in the FC region, the small 5% detuning leads to large variations in the transition dipole moment easing and hindering one of the transitions.

It is interesting to notice that, along the isomerization, the P0/P1 transition probability rises and then goes to zero at the TS. After a small rotation the ω_c becomes off resonance, leading to a P1 state dominated by the bright $|1B, 0\rangle$ basis state, and therefore the probability increases. Close to the TS, however, the $1B$ is not bright, leading to two dark polaritonic states. This trend is verified also for the detuned cavity frequencies. The same applies to P3: after a small rotation it becomes dominated by the $|1A, 1\rangle$ basis state, which is a dark state. The P2 polariton is always described almost completely by the $|2A, 0\rangle$ basis state, and remains dark.

Under a resonant cavity mode the P0/P1 transition energy is shifted by 0.29eV to 4.94eV=251.1nm and the P0/P3 by 0.30eV to 5.53eV=224.2nm, with respect to the gas phase transition, the peak height is identical. The shift is not symmetric as in the Jaynes-Cummings model due to the different dipole self energy terms implemented in the Pauli-Fierz Hamiltonian. The negative detuning shifts the P0/P1 excitation by 0.44eV to 4.79eV=259.0nm and the P0/P3 by 0.19eV to 5.42eV=228.8nm. The positive detuning shifts the P0/P1 excitation by 0.19eV to 5.03eV=246.3nm and the P0/P3 by 0.47eV to 5.69eV=217.7nm. A detuned frequency makes one of the two transition less probable, however both are still allowed. The only forbidden transition is the P0/P2. The P0/P1 transition promotes the gas-phase isomerization mechanism, through excitation in the FC region and de-excitation near the TS. The formation of the polaritons eases this mechanism, lowering the excitation energy.

The large shift of the excitation energies upon small changes of the cavity mode suggest that hexatriene may be used as a diagnostic system to evaluate the precision and of the cavity frequency, using the free space conditions as a reference.

After studying the effect of a cavity frequency resonant with the $1A/1B$ transition in the FC region (and a small detuning) it is natural to investigate the effect of a large variation of the cavity frequency. Now, the ω_c frequency is taken equal to the $1A/1B$ transition in the TS. The polaritonic potential energy curves are reported in fig. 4.10.

This frequency does not promote a basis states mixing, since the transition dipole moments are close to zero near the TS geometry. Nevertheless it produces an intersection between the P1 polariton (dominated by the $|1B, 0\rangle$ basis, orange in fig. 4.10) and the P3 polariton (dominated by the $|1A, 1\rangle$ basis, purple in fig. 4.10). The P0/P1 and P3/P1 transitions are dipole allowed, therefore the P1 state can be efficiently populated. The de-excitation pathways then passes through a conical intersection, which promotes a faster trans-to-cis isomerization with respect to the gas-phase mechanism.

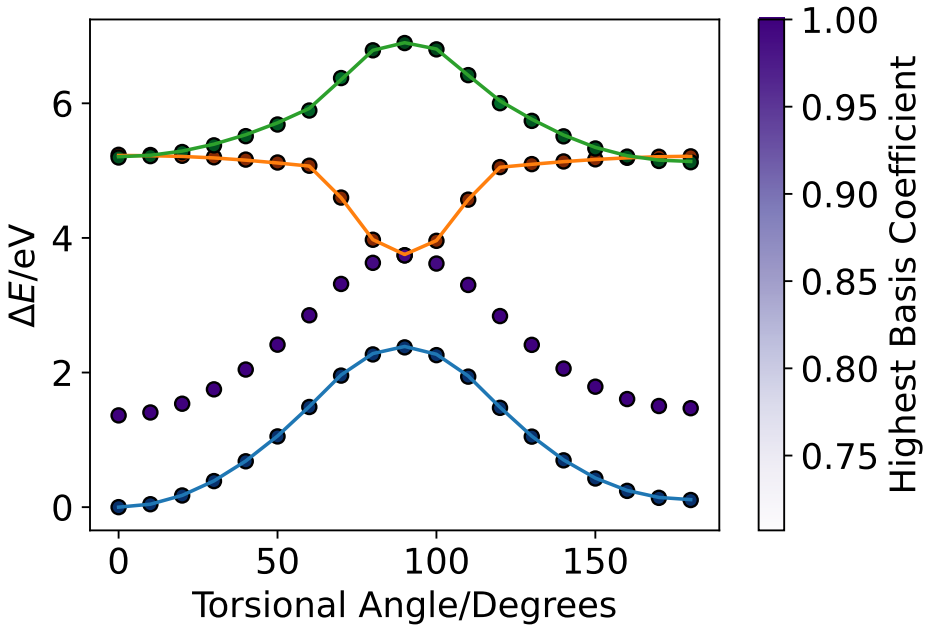

Figure 4.10: Polaritonic potential energy curves. The intensity of the color is related to the highest combination coefficient in the polaritonic state, the darker the color the closest is the polariton to one of the basis states. Blue: P0, orange: P1, green: P2, purple: P3. (a) ω_c =1.36 eV=907.8 nm resonant with the $1A/1B$ transition energy in the TS. $\lambda = 0.01$ a.u.

4.3 Remarks

The formation of hybrid light-matter states, polaritons has been investigated along the isomerization pathway of 1,3-butadiene and 1,3,5-hexatriene.

The s-trans to s-cis isomerization of butadiene has been studied using the *ab initio* quantum electrodynamics-Hartee-Fock method, limited to the vacuum field-ground state interaction. The results demonstrate that the molecular orientation plays a central role in determining the effect of the cavity. Upon varying the orientation, the isomerization barrier can be either increased or decreased. By controlling the orientation of the molecule and the strength of the coupling, it is possible to selectively control the isomerization pathway of 1,3-butadiene. The cavity modes rearrange the molecular electron density, modifying the σ framework and affecting the barrier.

The trans-to-cis isomerization of hexatriene has been studied with a parametrized QED approach, which relies on gas-phase *ab initio* calculations and can handle an arbitrary number of electronic and photonic states. This approach allows the calculation of several polaritonic states. A cavity mode resonant with the lowest electronic transition in the Franck-Condon region leads to the formation of polaritonic states in which the isomerization is easier. Also the absorption spectrum is affected, with shifts of about 0.2 eV. A 5% detuning of the cavity frequency leads to improved catalytic effects and allows the control of the position and intensity of the spectral peaks. The usage of a completely different frequency, resonant

with the lowest electronic transition in the transition state region leads to the formation of an intersection between polaritonic states, which could drastically ease the photoinduced isomerization.

References

[1] Daniel A Steck. *Quantum and Atom Optics*. en. URL: http://steck.us/teaching.

[2] I. A. Walmsley. "Quantum optics: Science and technology in a new light". In: *Science* 348.6234 (May 2015). Publisher: American Association for the Advancement of Science, pp. 525–530. DOI: 10.1126/science.aab0097. URL: https://www.science.org/doi/full/10.1126/science.aab0097.

[3] Orazio Svelto. *Principles of Lasers*. en. Boston, MA: Springer US, 2010. ISBN: 978-1-4419-1301-2. DOI: 10.1007/978-1-4419-1302-9. URL: http://link.springer.com/10.1007/978-1-4419-1302-9.

[4] Margherita Maiuri, Marco Garavelli, and Giulio Cerullo. "Ultrafast Spectroscopy: State of the Art and Open Challenges". In: *J. Am. Chem. Soc.* 142.1 (Jan. 2020). Publisher: American Chemical Society, pp. 3–15. ISSN: 0002-7863. DOI: 10.1021/jacs.9b10533. URL: https://doi.org/10.1021/jacs.9b10533.

[5] Frank Schlawin. "Entangled photon spectroscopy". en. In: *J. Phys. B: At. Mol. Opt. Phys.* 50.20 (Oct. 2017). Publisher: IOP Publishing, p. 203001. ISSN: 0953-4075. DOI: 10.1088/1361-6455/aa8a7a. URL: https://dx.doi.org/10.1088/1361-6455/aa8a7a.

[6] Marta Gilaberte Basset et al. "Perspectives for Applications of Quantum Imaging". en. In: *Laser & Photonics Reviews* 13.10 (2019), p. 1900097. ISSN: 1863-8899. DOI: 10.1002/lpor.201900097. URL: https://onlinelibrary.wiley.com/doi/abs/10.1002/lpor.201900097.

[7] Thomas W. Ebbesen. "Hybrid Light–Matter States in a Molecular and Material Science Perspective". In: *Acc. Chem. Res.* 49.11 (Nov. 2016). Publisher: American Chemical Society, pp. 2403–2412. ISSN: 0001-4842. DOI: 10.1021/acs.accounts.6b00295. URL: https://doi.org/10.1021/acs.accounts.6b00295.

[8] Markus Kowalewski and Shaul Mukamel. "Manipulating molecules with quantum light". In: *Proceedings of the National Academy of Sciences* 114.13 (Mar. 2017). Publisher: Proceedings of the National Academy of Sciences, pp. 3278–3280. DOI: 10.1073/pnas.1702160114. URL: https://www.pnas.org/doi/full/10.1073/pnas.1702160114.

[9] Francisco J. Garcia-Vidal, Cristiano Ciuti, and Thomas W. Ebbesen. "Manipulating matter by strong coupling to vacuum fields". In: *Science* 373.6551 (July 2021). Publisher: American Association for the Advancement of Science, eabd0336. DOI: 10.1126/science.abd0336. URL: https://www.science.org/doi/10.1126/science.abd0336.

[10] Johannes Flick, Nicholas Rivera, and Prineha Narang. "Strong light-matter coupling in quantum chemistry and quantum photonics". en. In: *Nanophotonics* 7.9 (Sept. 2018). Publisher: De Gruyter, pp. 1479–1501. ISSN: 2192-8614. DOI: 10.1515/nanoph-2018-0067. URL: https://www.degruyter.com/document/doi/10.1515/nanoph-2018-0067/html.

[11] D. N. Basov et al. "Polariton panorama". en. In: *Nanophotonics* 10.1 (Jan. 2021). Publisher: De Gruyter, pp. 549–577. ISSN: 2192-8614. DOI: 10.1515/nanoph-2020-0449. URL: https://www.degruyter.com/document/doi/10.1515/nanoph-2020-0449/html.

[12] Mario V. Imperatore, John B. Asbury, and Noel C. Giebink. "Reproducibility of cavity-enhanced chemical reaction rates in the vibrational strong coupling regime". In: *The Journal of Chemical Physics* 154.19 (May 2021), p. 191103. ISSN: 0021-9606. DOI: 10.1063/5.0046307. URL: https://doi.org/10.1063/5.0046307.

[13] Garret D. Wiesehan and Wei Xiong. "Negligible rate enhancement from reported cooperative vibrational strong coupling catalysis". In: *The Journal of Chemical Physics* 155.24 (Dec. 2021), p. 241103. ISSN: 0021-9606. DOI: 10.1063/5.0077549. URL: https://doi.org/10.1063/5.0077549.

[14] Blake S. Simpkins, Adam D. Dunkelberger, and Igor Vurgaftman. "Control, Modulation, and Analytical Descriptions of Vibrational Strong Coupling". In: *Chem. Rev.* 123.8 (Apr. 2023). Publisher: American Chemical Society, pp. 5020–5048. ISSN: 0009-2665. DOI: 10.1021/acs.chemrev.2c00774. URL: https://doi.org/10.1021/acs.chemrev.2c00774.

[15] Abhijit Sau et al. "Modifying Woodward–Hoffmann Stereoselectivity Under Vibrational Strong Coupling". en. In: *Angewandte Chemie International Edition* 60.11 (2021), pp. 5712–5717. ISSN: 1521-3773. DOI: 10.1002/anie.202013465. URL: https://onlinelibrary.wiley.com/doi/abs/10.1002/anie.202013465.

[16] A. Thomas et al. "Tilting a ground-state reactivity landscape by vibrational strong coupling". In: *Science* 363.6427 (Feb. 2019). Publisher: American Association for the Advancement of Science, pp. 615–619. DOI: 10.1126/science.aau7742. URL: https://www.science.org/doi/10.1126/science.aau7742.

[17] Anoop Thomas et al. "Ground-State Chemical Reactivity under Vibrational Coupling to the Vacuum Electromagnetic Field". en. In: *Angewandte Chemie* 128.38 (2016), pp. 11634–11638. ISSN: 1521-3757. DOI: 10.1002/ange.201605504. URL: https://onlinelibrary.wiley.com/doi/abs/10.1002/ange.201605504.

[18] James A. Hutchison et al. "Modifying Chemical Landscapes by Coupling to Vacuum Fields". In: *Angewandte Chemie International Edition* 51.7 (2012), pp. 1592–1596. ISSN: 1521-3773. DOI: 10.1002/anie.201107033. URL: https://onlinelibrary.wiley.com/doi/abs/10.1002/anie.201107033.

[19] Jyoti Lather et al. "Cavity Catalysis by Cooperative Vibrational Strong Coupling of Reactant and Solvent Molecules". en. In: *Angewandte Chemie International Edition* 58.31 (2019), pp. 10635–10638. ISSN: 1521-3773. DOI: 10.1002/anie.201905407. URL: https://onlinelibrary.wiley.com/doi/abs/10.1002/anie.201905407.

[20] Rocío Sáez-Blázquez et al. "Can We Observe Nonperturbative Vacuum Shifts in Cavity QED?" In: *Phys. Rev. Lett.* 131.1 (July 2023). Publisher: American Physical Society, p. 013602. DOI: 10.1103/PhysRevLett.131.013602. URL: https://link.aps.org/doi/10.1103/PhysRevLett.131.013602.

[21] John P. Philbin et al. "Chemical Reactions in Imperfect Cavities: Enhancement, Suppression, and Resonance". In: *The Journal of Physical Chemistry C* 126.35 (2022), pp. 14908–14913. DOI: 10.1021/acs.jpcc.2c04741. URL: https://doi.org/10.1021/acs.jpcc.2c04741.

[22] Arkajit Mandal and Pengfei Huo. "Investigating New Reactivities Enabled by Polariton Photochemistry". In: *J. Phys. Chem. Lett.* 10.18 (Sept. 2019). Publisher: American Chemical Society, pp. 5519–5529. DOI: 10.1021/acs.jpclett.9b01599. URL: https://doi.org/10.1021/acs.jpclett.9b01599.

[23] Raphael F. Ribeiro et al. "Polariton chemistry: controlling molecular dynamics with optical cavities". en. In: *Chem. Sci.* 9.30 (Aug. 2018). Publisher: The Royal Society of Chemistry, pp. 6325–6339. ISSN: 2041-6539. DOI: 10.1039/C8SC01043A. URL: https://pubs.rsc.org/en/content/articlelanding/2018/sc/c8sc01043a.

[24] Braden M. Weight, Todd D. Krauss, and Pengfei Huo. "Investigating Molecular Exciton Polaritons Using Ab Initio Cavity Quantum Electrodynamics". In: *The Journal of Physical Chemistry Letters* 14.25 (2023). PMID: 37343178, pp. 5901–5913. DOI: 10.1021/acs.jpclett.3c01294. URL: https://doi.org/10.1021/acs.jpclett.3c01294.

[25] Derek S. Wang et al. "Light–matter interaction of a molecule in a dissipative cavity from first principles". In: *The Journal of Chemical Physics* 154.10 (Mar. 2021), p. 104109. ISSN: 0021-9606. DOI: 10.1063/5.0036283. URL: https://doi.org/10.1063/5.0036283.

[26] Fabijan Pavošević et al. "Cavity-Modulated Proton Transfer Reactions". In: *J. Am. Chem. Soc.* 144.11 (Mar. 2022). Publisher: American Chemical Society, pp. 4995–5002. ISSN: 0002-7863. DOI: 10.1021/jacs.1c13201. URL: https://doi.org/10.1021/jacs.1c13201.

[27] Tao E. Li and Sharon Hammes-Schiffer. "QM/MM Modeling of Vibrational Polariton Induced Energy Transfer and Chemical Dynamics". In: *Journal of the American Chemical Society* 145.1 (2023). PMID: 36574620, pp. 377–384. DOI: 10.1021/jacs.2c10170. URL: https://doi.org/10.1021/jacs.2c10170.

[28] Arkajit Mandal, Todd D. Krauss, and Pengfei Huo. "Polariton-Mediated Electron Transfer via Cavity Quantum Electrodynamics". In: *J. Phys. Chem. B* 124.29 (July 2020). Publisher: American Chemical Society, pp. 6321–6340. ISSN: 1520-6106. DOI: 10.1021/acs.jpcb.0c03227. URL: https://doi.org/10.1021/acs.jpcb.0c03227.

[29] Yu-Chen Wei and Liang-Yan Hsu. "Cavity-Free Quantum-Electrodynamic Electron Transfer Reactions". In: *J. Phys. Chem. Lett.* 13.41 (Oct. 2022). Publisher: American Chemical Society, pp. 9695–9702. DOI: 10.1021/acs.jpclett.2c02379. URL: https://doi.org/10.1021/acs.jpclett.2c02379.

[30] Qi Yu and Sharon Hammes-Schiffer. "Multidimensional Quantum Dynamical Simulation of Infrared Spectra under Polaritonic Vibrational Strong Coupling". In: *The Journal of Physical Chemistry Letters* 13.48 (2022). PMID: 36448842, pp. 11253–11261. DOI: 10.1021/acs.jpclett.2c03245. URL: https://doi.org/10.1021/acs.jpclett.2c03245.

[31] Tor S. Haugland et al. "Intermolecular interactions in optical cavities: An ab initio QED study". In: *The Journal of Chemical Physics* 154.9 (Mar. 2021), p. 094113. ISSN: 0021-9606. DOI: 10.1063/5.0039256. URL: https://doi.org/10.1063/5.0039256.

[32] Ayaki Sunaga, Maen Salman, and Trond Saue. "4-component relativistic Hamiltonian with effective QED potentials for molecular calculations". In: *The Journal of Chemical Physics* 157.16 (Oct. 2022), p. 164101. ISSN: 0021-9606. DOI: 10.1063/5.0116140. URL: https://doi.org/10.1063/5.0116140.

[33] Xinyang Li, Arkajit Mandal, and Pengfei Huo. "Theory of Mode-Selective Chemistry through Polaritonic Vibrational Strong Coupling". In: *J. Phys. Chem. Lett.* 12.29 (July 2021). Publisher: American Chemical Society, pp. 6974–6982. DOI: 10.1021/acs.jpclett.1c01847. URL: https://doi.org/10.1021/acs.jpclett.1c01847.

[34] Christian Schäfer. "Polaritonic Chemistry from First Principles via Embedding Radiation Reaction". In: *J. Phys. Chem. Lett.* 13.30 (Aug. 2022). Publisher: American Chemical Society, pp. 6905–6911. DOI: 10.1021/acs.jpclett.2c01169. URL: https://doi.org/10.1021/acs.jpclett.2c01169.

[35] Felipe Herrera and Frank C. Spano. "Cavity-Controlled Chemistry in Molecular Ensembles". In: *Phys. Rev. Lett.* 116 (23 2016), p. 238301. DOI: 10.1103/PhysRevLett.116.238301. URL: https://link.aps.org/doi/10.1103/PhysRevLett.116.238301.

[36] Johannes Flick and Prineha Narang. "Ab initio polaritonic potential-energy surfaces for excited-state nanophotonics and polaritonic chemistry". In: *The Journal of Chemical Physics* 153.9 (Sept. 2020), p. 094116. ISSN: 0021-9606. DOI: 10.1063/5.0021033. URL: https://doi.org/10.1063/5.0021033.

[37] Nam Vu et al. "Enhanced Diastereocontrol via Strong Light–Matter Interactions in an Optical Cavity". In: *J. Phys. Chem. A* 126.49 (Dec. 2022). Publisher: American Chemical Society, pp. 9303–9312. ISSN: 1089-5639. DOI: 10.1021/acs.jpca.2c07134. URL: https://doi.org/10.1021/acs.jpca.2c07134.

[38] E.T. Jaynes and F.W. Cummings. "Comparison of quantum and semiclassical radiation theories with application to the beam maser". In: *Proceedings of the IEEE* 51.1 (Jan. 1963). Conference Name: Proceedings of the IEEE, pp. 89–109. ISSN: 1558-2256. DOI: 10.1109/PROC.1963.1664. URL: https://ieeexplore.ieee.org/document/1443594.

[39] Michael Tavis and Frederick W. Cummings. "Exact Solution for an N-Molecule—Radiation-Field Hamiltonian". In: *Phys. Rev.* 170.2 (June 1968). Publisher: American Physical Society, pp. 379–384. DOI: 10.1103/PhysRev.170.379. URL: https://link.aps.org/doi/10.1103/PhysRev.170.379.

[40] Philip A. Thomas, Kishan S. Menghrajani, and William L. Barnes. "Cavity-Free Ultrastrong Light-Matter Coupling". In: *J. Phys. Chem. Lett.* 12.29 (July 2021). Publisher: American Chemical Society, pp. 6914–6918. DOI: 10.1021/acs.jpclett.1c01695. URL: https://doi.org/10.1021/acs.jpclett.1c01695.

[41] Arkajit Mandal et al. "Theoretical Advances in Polariton Chemistry and Molecular Cavity Quantum Electrodynamics". In: *Chem. Rev.* 123.16 (Aug. 2023). Publisher: American Chemical Society, pp. 9786–9879. ISSN: 0009-2665. DOI: 10.1021/acs.chemrev.2c00855. URL: https://doi.org/10.1021/acs.chemrev.2c00855.

[42] Rohit Chikkaraddy et al. "Single-molecule strong coupling at room temperature in plasmonic nanocavities". en. In: *Nature* 535.7610 (July 2016). Number: 7610 Publisher: Nature Publishing Group, pp. 127–130. ISSN: 1476-4687. DOI: 10.1038/nature17974. URL: https://www.nature.com/articles/nature17974.

[43] T. Schwartz et al. "Reversible Switching of Ultrastrong Light-Molecule Coupling". In: *Phys. Rev. Lett.* 106.19 (May 2011). Publisher: American Physical Society, p. 196405. DOI: 10.1103/PhysRevLett.106.196405. URL: https://link.aps.org/doi/10.1103/PhysRevLett.106.196405.

[44] Anton Frisk Kockum et al. "Ultrastrong coupling between light and matter". en. In: *Nat Rev Phys* 1.1 (Jan. 2019). Number: 1 Publisher: Nature Publishing Group, pp. 19–40. ISSN: 2522-5820. DOI: 10.1038/s42254-018-0006-2. URL: https://www.nature.com/articles/s42254-018-0006-2.

[45] Vasil Rokaj et al. "Light–matter interaction in the long-wavelength limit: no ground-state without dipole self-energy". en. In: *J. Phys. B: At. Mol. Opt. Phys.* 51.3 (Jan. 2018). Publisher: IOP Publishing, p. 034005. ISSN: 0953-4075. DOI: 10.1088/1361-6455/aa9c99. URL: https://dx.doi.org/10.1088/1361-6455/aa9c99.

[46] Gilbert Grynberg, Alain Aspect, and Claude Fabre. *Introduction to Quantum Optics: From the Semi-classical Approach to Quantized Light*. en. Cambridge University Press, Sept. 2010. ISBN: 978-1-139-49084-9.

[47] Marlan O. Scully and M. Suhail Zubairy. *Quantum Optics*. en. Google-Books-ID: 20ISsQCKKmQC. Cambridge University Press, Sept. 1997. ISBN: 978-0-521-43595-6.

[48] Peter W. Milonni and Peter W. Milonni. *An Introduction to Quantum Optics and Quantum Fluctuations*. Oxford Graduate Texts. Oxford, New York: Oxford University Press, Jan. 2019. ISBN: 978-0-19-921561-4.

[49] Attila Szabo and Neil S. Ostlund. *Modern Quantum Chemistry: Introduction to Advanced Electronic Structure Theory*. en. Courier Corporation, July 1996. ISBN: 978-0-486-69186-2.

[50] R. G. Woolley. "A reformulation of molecular quantum electrodynamics". en. In: *J. Phys. B: Atom. Mol. Phys.* 7.4 (Mar. 1974), p. 488. ISSN: 0022-3700. DOI: 10.1088/0022-3700/7/4/023. URL: https://dx.doi.org/10.1088/0022-3700/7/4/023.

[51] Edwin Albert Power, S. Zienau, and Harrie Stewart Wilson Massey. "Coulomb gauge in non-relativistic quantum electro-dynamics and the shape of spectral lines". In: *Philosophical Transactions of the Royal Society of London. Series A, Mathematical and Physical Sciences* 251.999 (Jan. 1997). Publisher: Royal Society, pp. 427–454. DOI: 10.1098/rsta.1959.0008. URL: https://royalsocietypublishing.org/doi/10.1098/rsta.1959.0008.

[52] M. Göppert-Mayer. "Elementary processes with two quantum transitions". In: *Annalen der Physik* 521.7-8 (2009), pp. 466–479. ISSN: 1521-3889. DOI: 10.1002/andp.200952107-804. URL: https://onlinelibrary.wiley.com/doi/abs/10.1002/andp.200952107-804.

[53] Christian Schäfer, Michael Ruggenthaler, and Angel Rubio. "Ab initio nonrelativistic quantum electrodynamics: Bridging quantum chemistry and quantum optics from weak to strong coupling". In: *Phys. Rev. A* 98.4 (Oct. 2018). Publisher: American Physical Society, p. 043801. DOI: 10.1103/PhysRevA.98.043801. URL: https://link.aps.org/doi/10.1103/PhysRevA.98.043801.

[54] Johannes Flick et al. "Atoms and molecules in cavities, from weak to strong coupling in quantum-electrodynamics (QED) chemistry". In: *Proceedings of the National Academy of Sciences* 114.12 (Mar. 2017). Publisher: Proceedings of the National Academy of Sciences, pp. 3026–3034. DOI: 10.1073/pnas.1615509114. URL: https://www.pnas.org/doi/abs/10.1073/pnas.1615509114.

[55] Junjie Yang et al. "Quantum-electrodynamical time-dependent density functional theory within Gaussian atomic basis". In: *The Journal of Chemical Physics* 155.6 (Aug. 2021), p. 064107. ISSN: 0021-9606. DOI: 10.1063/5.0057542. URL: https://doi.org/10.1063/5.0057542.

[56] Wanghuai Zhou et al. "Nuclear gradient expressions for molecular cavity quantum electrodynamics simulations using mixed quantum-classical methods". In: *The Journal of Chemical Physics* 157.10 (Sept. 2022), p. 104118. ISSN: 0021-9606. DOI: 10.1063/5.0109395. URL: https://doi.org/10.1063/5.0109395.

[57] Michael A. D. Taylor et al. "Resolution of Gauge Ambiguities in Molecular Cavity Quantum Electrodynamics". In: *Phys. Rev. Lett.* 125.12 (Sept. 2020). Publisher: American Physical Society, p. 123602. DOI: 10.1103/PhysRevLett.125.123602. URL: https://link.aps.org/doi/10.1103/PhysRevLett.125.123602.

[58] Daniele De Bernardis et al. "Breakdown of gauge invariance in ultrastrong-coupling cavity QED". In: *Phys. Rev. A* 98.5 (Nov. 2018). Publisher: American Physical Society, p. 053819. DOI: 10.1103/PhysRevA.98.053819. URL: https://link.aps.org/doi/10.1103/PhysRevA.98.053819.

[59] Deping Hu et al. "Quasi-diabatic propagation scheme for simulating polariton chemistry". In: *The Journal of Chemical Physics* 157.19 (Nov. 2022), p. 194109. ISSN: 0021-9606. DOI: 10.1063/5.0127118. URL: https://doi.org/10.1063/5.0127118.

[60] Michael Ruggenthaler, Dominik Sidler, and Angel Rubio. *Understanding polaritonic chemistry from ab initio quantum electrodynamics*. arXiv:2211.04241 [quant-ph]. Nov. 2022. DOI: 10.48550/arXiv.2211.04241. URL: http://arxiv.org/abs/2211.04241.

[61] Rosario R. Riso et al. "Molecular orbital theory in cavity QED environments". en. In: *Nat Commun* 13.1 (Mar. 2022). Number: 1 Publisher: Nature Publishing Group, p. 1368. ISSN: 2041-1723. DOI: 10.1038/s41467-022-29003-2. URL: https://www.nature.com/articles/s41467-022-29003-2.

[62] Jonathan McTague and Jonathan J. Foley IV. "Non-Hermitian cavity quantum electrodynamics–configuration interaction singles approach for polaritonic structure with ab initio molecular Hamiltonians". In: *The Journal of Chemical Physics* 156.15 (Apr. 2022), p. 154103. ISSN: 0021-9606. DOI: 10.1063/5.0091953. URL: https://doi.org/10.1063/5.0091953.

[63] Florian Buchholz et al. "Light–Matter Hybrid-Orbital-Based First-Principles Methods: The Influence of Polariton Statistics". In: *J. Chem. Theory Comput.* 16.9 (Sept. 2020). Publisher: American Chemical Society, pp. 5601–5620. ISSN: 1549-9618. DOI: 10.1021/acs.jctc.0c00469. URL: https://doi.org/10.1021/acs.jctc.0c00469.

[64] Nam Vu et al. *Cavity Quantum Electrodynamics Complete Active Space Configuration Interaction Theory*. en. Nov. 2023. DOI: 10.26434/chemrxiv-2023-kbhcv. URL: https://chemrxiv.org/engage/chemrxiv/article-details/654144aec573f893f186c3ab.

[65] Tor S. Haugland et al. "Coupled Cluster Theory for Molecular Polaritons: Changing Ground and Excited States". In: *Phys. Rev. X* 10.4 (Dec. 2020). Publisher: American Physical Society, p. 041043. DOI: 10.1103/PhysRevX.10.041043. URL: https://link.aps.org/doi/10.1103/PhysRevX.10.041043.

[66] Christian Schäfer et al. "Making ab initio QED functional(s): Nonperturbative and photon-free effective frameworks for strong light–matter coupling". In: *Proceedings of the National Academy of Sciences* 118.41 (Oct. 2021). Publisher: Proceedings of the National Academy of Sciences, e2110464118. DOI: 10.1073/pnas.2110464118. URL: https://www.pnas.org/doi/10.1073/pnas.2110464118.

[67] Camilla Pellegrini et al. "Optimized Effective Potential for Quantum Electrodynamical Time-Dependent Density Functional Theory". In: *Phys. Rev. Lett.* 115.9 (Aug. 2015). Publisher: American Physical Society, p. 093001. DOI: 10.1103/PhysRevLett.115.093001. URL: https://link.aps.org/doi/10.1103/PhysRevLett.115.093001.

[68] Johannes Flick et al. "Ab Initio Optimized Effective Potentials for Real Molecules in Optical Cavities: Photon Contributions to the Molecular Ground State". In: *ACS Photonics* 5.3 (Mar. 2018). Publisher: American Chemical Society, pp. 992–1005. DOI: 10.1021/acsphotonics.7b01279. URL: https://doi.org/10.1021/acsphotonics.7b01279.

[69] T. G. Philbin. "Generalized coherent states". en. In: *American Journal of Physics* 82.8 (Aug. 2014), pp. 742–748. ISSN: 0002-9505, 1943-2909. DOI: 10.1119/1.4876963. URL: https://pubs.aip.org/ajp/article/82/8/742/1057585/Generalized-coherent-states.

[70] Rahul Bhuyan et al. "The Rise and Current Status of Polaritonic Photochemistry and Photophysics". In: *Chem. Rev.* 123.18 (Sept. 2023). Publisher: American Chemical Society, pp. 10877–10919. ISSN: 0009-2665. DOI: 10.1021/acs.chemrev.2c00895. URL: https://doi.org/10.1021/acs.chemrev.2c00895.

[71] Tao E. Li et al. "Molecular Polaritonics: Chemical Dynamics Under Strong Light–Matter Coupling". In: *Annual Review of Physical Chemistry* 73.1 (2022), pp. 43–71. DOI: 10.1146/annurev-physchem-090519-042621. URL: https://doi.org/10.1146/annurev-physchem-090519-042621.

[72] Dominik Sidler et al. "A perspective on ab initio modeling of polaritonic chemistry: The role of non-equilibrium effects and quantum collectivity". In: *The Journal of Chemical Physics* 156.23 (June 2022), p. 230901. ISSN: 0021-9606. DOI: 10.1063/5.0094956. URL: https://doi.org/10.1063/5.0094956.

[73] Johannes Feist, Javier Galego, and Francisco J. Garcia-Vidal. "Polaritonic Chemistry with Organic Molecules". In: *ACS Photonics* 5.1 (Jan. 2018). Publisher: American Chemical Society, pp. 205–216. DOI: 10.1021/acsphotonics.7b00680. URL: https://doi.org/10.1021/acsphotonics.7b00680.

[74] Robert S. H. Liu and George S. Hammond. "Photochemical reactivity of polyenes: from dienes to rhodopsin, from microseconds to femtoseconds". In: *Photochem. Photobiol. Sci.* 2 (8 2003), pp. 835–844. DOI: 10.1039/B304027E. URL: http://dx.doi.org/10.1039/B304027E.

[75] Begoña Milián-Medina and Johannes Gierschner. "π-Conjugation". In: *WIREs Computational Molecular Science* 2.4 (2012), pp. 513–524. DOI: https://doi.org/10.1002/wcms.95. URL: https://wires.onlinelibrary.wiley.com/doi/abs/10.1002/wcms.95.

[76] Bruce S. Hudson, Bryan E. Kohler, and Klaus Schulten. "Linear Polyene Electronic Structure and Potential Surfaces". In: ed. by Edward C. Lim. Vol. 6. Excited States. Elsevier, 1982, pp. 1–95. DOI: https://doi.org/10.1016/B978-0-12-227206-6.50006-5. URL: https://www.sciencedirect.com/science/article/pii/B9780122272066500065.

[77] Miquel Solà and F. Matthias Bickelhaupt. "Particle on a Ring Model for Teaching the Origin of the Aromatic Stabilization Energy and the Hückel and Baird Rules". In: *Journal of Chemical Education* 99.10 (2022), pp. 3497–3501. DOI: 10.1021/acs.jchemed.2c00523. URL: https://doi.org/10.1021/acs.jchemed.2c00523.

[78] Jochen Autschbach. "Why the Particle-in-a-Box Model Works Well for Cyanine Dyes but Not for Conjugated Polyenes". In: *Journal of Chemical Education* 84.11 (2007), p. 1840. DOI: 10.1021/ed084p1840. URL: https://doi.org/10.1021/ed084p1840.

[79] Robert R. Rando. "Polyenes and vision". In: *Chemistry & Biology* 3.4 (1996), pp. 255–262. ISSN: 1074-5521. DOI: https://doi.org/10.1016/S1074-5521(96)90105-2. URL: https://www.sciencedirect.com/science/article/pii/S1074552196901052.

[80] Philip J. M. Johnson et al. "Local vibrational coherences drive the primary photochemistry of vision". en. In: *Nature Chem* 7.12 (Dec. 2015). Number: 12 Publisher: Nature Publishing Group, pp. 980–986. ISSN: 1755-4349. DOI: 10.1038/nchem.2398. URL: https://www.nature.com/articles/nchem.2398.

[81] Yvonne Maria te Welscher et al. "Polyene antibiotic that inhibits membrane transport proteins". In: *Proceedings of the National Academy of Sciences* 109.28 (2012), pp. 11156–11159. DOI: 10.1073/pnas.1203375109. URL: https://www.pnas.org/doi/abs/10.1073/pnas.1203375109.

[82] André Moliton and Roger C. Hiorns. "The origin and development of (plastic) organic electronics". In: *Polymer International* 61.3 (2012), pp. 337–341. DOI: https://doi.org/10.1002/pi.4173. URL: https://onlinelibrary.wiley.com/doi/abs/10.1002/pi.4173.

[83] Laren M. Tolbert. "Solitons in a box: the organic chemistry of electrically conducting polyenes". In: *Accounts of Chemical Research* 25.12 (1992), pp. 561–568. DOI: 10.1021/ar00024a003. URL: https://doi.org/10.1021/ar00024a003.

[84] Marco Severi. *How to align a molecule to the cartesian axes*. original-date: 2023-09-13T12:49:55Z. Sept. 2023. URL: https://github.com/MSeveri96/how-to-align-molecule-to-axes.

[85] Albert C. Aragonès et al. "Electrostatic catalysis of a Diels–Alder reaction". en. In: *Nature* 531.7592 (Mar. 2016). Number: 7592 Publisher: Nature Publishing Group, pp. 88–91. ISSN: 1476-4687. DOI: 10.1038/nature16989. URL: https://www.nature.com/articles/nature16989.

[86] *Bretislav Friedrich - The Exacting Task of Bringing Molecules to Attention*. en-US. Section: Physical Science. Dec. 2017. URL: https://www.scientia.global/bretislav-friedrich-exacting-task-bringing-molecules-attention/.

[87] Sarai D. Folkestad et al. "e^T 1.0: An open source electronic structure program with emphasis on coupled cluster and multilevel methods". en. In: *J. Chem. Phys.* 152.18 (May 2020), p. 184103. ISSN: 0021-9606, 1089-7690. DOI: 10.1063/5.0004713. URL: https://pubs.aip.org/aip/jcp/article/973043.

[88] M. J. Frisch et al. *Gaussian˜16 Revision C.01*. Gaussian Inc. Wallingford CT. 2016.

[89] Benjamin P. Pritchard et al. "New Basis Set Exchange: An Open, Up-to-Date Resource for the Molecular Sciences Community". In: *J. Chem. Inf. Model.* 59.11 (Nov. 2019). Publisher: American Chemical Society, pp. 4814–4820. ISSN: 1549-9596. DOI: 10.1021/acs.jcim.9b00725. URL: https://doi.org/10.1021/acs.jcim.9b00725.

[90] Karen L. Schuchardt et al. "Basis Set Exchange: A Community Database for Computational Sciences". In: *J. Chem. Inf. Model.* 47.3 (May 2007). Publisher: American Chemical Society, pp. 1045–1052. ISSN: 1549-9596. DOI: 10.1021/ci600510j. URL: https://doi.org/10.1021/ci600510j.

[91] W. J. Hehre, R. Ditchfield, and J. A. Pople. "Self—Consistent Molecular Orbital Methods. XII. Further Extensions of Gaussian—Type Basis Sets for Use in Molecular Orbital Studies of Organic Molecules". In: *Journal of Chemical Physics* 56 (Mar. 1972), pp. 2257–2261. ISSN: 0021-96060301-0104. DOI: 10.1063/1.1677527. URL: https://ui.adsabs.harvard.edu/abs/1972JChPh..56.2257H.

[92] P. C. Hariharan and J. A. Pople. "The influence of polarization functions on molecular orbital hydrogenation energies". en. In: *Theoret. Chim. Acta* 28.3 (Sept. 1973), pp. 213–222. ISSN: 1432-2234. DOI: 10.1007/BF00533485. URL: https://doi.org/10.1007/BF00533485.

[93] David Feller. "The role of databases in support of computational chemistry calculations". en. In: *Journal of Computational Chemistry* 17.13 (1996), pp. 1571–1586. ISSN: 1096-987X. DOI: 10.1002/(SICI)1096-987X(199610)17:13<1571::AID-JCC9>3.0.CO;2-P. URL: https://onlinelibrary.wiley.com/doi/abs/10.1002/%28SICI%291096-987X%28199610%2917%3A13%3C1571%3A%3AAID-JCC9%3E3.0.CO%3B2-P.

[94] Matteo Barborini and Leonardo Guidoni. "Reaction pathways by quantum Monte Carlo: Insight on the torsion barrier of 1,3-butadiene, and the conrotatory ring opening of cyclobutene". In: *The Journal of Chemical Physics* 137.22 (Dec. 2012), p. 224309. ISSN: 0021-9606. DOI: 10.1063/1.4769791. URL: https://doi.org/10.1063/1.4769791.

[95] Woojin Park et al. "Internal Conversion between Bright (11Bu+) and Dark (21Ag–) States in s-trans-Butadiene and s-trans-Hexatriene". In: *J. Phys. Chem. Lett.* 12.39 (Oct. 2021). Publisher: American Chemical Society, pp. 9720–9729. DOI: 10.1021/acs.jpclett.1c02707. URL: https://doi.org/10.1021/acs.jpclett.1c02707.

[96] Mark A. Watson and Garnet Kin-Lic Chan. "Excited States of Butadiene to Chemical Accuracy: Reconciling Theory and Experiment". In: *J. Chem. Theory Comput.* 8.11 (Nov. 2012). Publisher: American Chemical Society, pp. 4013–4018. ISSN: 1549-9618. DOI: 10.1021/ct300591z. URL: https://doi.org/10.1021/ct300591z.

[97] Massimo Olivucci et al. "Excited-state cis-trans isomerization of cis-hexatriene. A CAS-SCF computational study". en. In: *J. Am. Chem. Soc.* 116.3 (Feb. 1994), pp. 1077–1085. ISSN: 0002-7863, 1520-5126. DOI: 10.1021/ja00082a033. URL: https://pubs.acs.org/doi/abs/10.1021/ja00082a033.

[98] R. Krishnan et al. "Self-consistent molecular orbital methods. XX. A basis set for correlated wave functions". In: *The Journal of Chemical Physics* 72.1 (July 2008), pp. 650–654. ISSN: 0021-9606. DOI: 10.1063/1.438955. URL: https://doi.org/10.1063/1.438955.

[99] John P. Perdew and Wang Yue. "Accurate and simple density functional for the electronic exchange energy: Generalized gradient approximation". In: *Phys. Rev. B* 33.12 (June 1986). Publisher: American Physical Society, pp. 8800–8802. DOI: 10.1103/PhysRevB.33.8800. URL: https://link.aps.org/doi/10.1103/PhysRevB.33.8800.

[100] Kateřina Fatková, Radim Cajzl, and Jaroslav V. Burda. "The vertical excitation energies and a lifetime of the two lowest singlet excited states of the conjugated polyenes from C2 to C22: Ab initio, DFT, and semiclassical MNDO-MD simulations". en. In: *Journal of Computational Chemistry* 44.6 (2023), pp. 777–787. ISSN: 1096-987X. DOI: 10.1002/jcc.27040. URL: https://onlinelibrary.wiley.com/doi/abs/10.1002/jcc.27040.

[101] Frank Neese. "The ORCA program system". In: *WIREs Computational Molecular Science* 2.1 (2012), pp. 73–78. DOI: https://doi.org/10.1002/wcms.81. URL: https://wires.onlinelibrary.wiley.com/doi/abs/10.1002/wcms.81.

[102] Frank Neese et al. "The ORCA quantum chemistry program package". In: *The Journal of Chemical Physics* 152.22 (June 2020), p. 224108. ISSN: 0021-9606. DOI: 10.1063/5.0004608. URL: https://doi.org/10.1063/5.0004608.

[103] Frank Neese. "Software update: the ORCA program system, version 4.0". In: *WIREs Computational Molecular Science* 8.1 (2018), e1327. DOI: https://doi.org/10.1002/wcms.1327. URL: https://wires.onlinelibrary.wiley.com/doi/abs/10.1002/wcms.1327.

[104] Frank Neese. "Software update: The ORCA program system—Version 5.0". In: *WIREs Computational Molecular Science* 12.5 (2022), e1606. DOI: https://doi.org/10.1002/wcms.1606. URL: https://wires.onlinelibrary.wiley.com/doi/abs/10.1002/wcms.1606.

[105] Frank Neese et al. "Efficient, approximate and parallel Hartree–Fock and hybrid DFT calculations. A 'chain-of-spheres' algorithm for the Hartree–Fock exchange". In: *Chemical Physics* 356.1 (2009). Moving Frontiers in Quantum Chemistry: pp. 98–109. ISSN: 0301-0104. DOI: https://doi.org/10.1016/j.chemphys.2008.10.036. URL: https://www.sciencedirect.com/science/article/pii/S0301010408005089.

[106] Georgi L. Stoychev, Alexander A. Auer, and Frank Neese. "Automatic Generation of Auxiliary Basis Sets". In: *J. Chem. Theory Comput.* 13.2 (Feb. 2017). Publisher: American Chemical Society, pp. 554–562. ISSN: 1549-9618. DOI: 10.1021/acs.jctc.6b01041. URL: https://doi.org/10.1021/acs.jctc.6b01041.

[107] Sitakanta Satapathy et al. "Selective isomer emission via funneling of exciton polaritons". In: *Science Advances* 7.44 (Oct. 2021). Publisher: American Association for the Advancement of Science, eabj0997. DOI: 10.1126/sciadv.abj0997. URL: https://www.science.org/doi/10.1126/sciadv.abj0997.

[108] Charlene Ng et al. "Waveguide-Plasmon Polariton Enhanced Photochemistry". en. In: *Advanced Optical Materials* 3.11 (2015), pp. 1582–1590. ISSN: 2195-1071. DOI: 10.1002/adom.201500157. URL: https://onlinelibrary.wiley.com/doi/abs/10.1002/adom.201500157.

[109] Markus Kowalewski, Kochise Bennett, and Shaul Mukamel. "Cavity Femtochemistry: Manipulating Nonadiabatic Dynamics at Avoided Crossings". In: *J. Phys. Chem. Lett.* 7.11 (June 2016). Publisher: American Chemical Society, pp. 2050–2054. DOI: 10.1021/acs.jpclett.6b00864. URL: https://doi.org/10.1021/acs.jpclett.6b00864.

[110] Markus Kowalewski, Kochise Bennett, and Shaul Mukamel. "Non-adiabatic dynamics of molecules in optical cavities". In: *The Journal of Chemical Physics* 144.5 (Feb. 2016), p. 054309. ISSN: 0021-9606. DOI: 10.1063/1.4941053. URL: https://doi.org/10.1063/1.4941053.

[111] J. Fregoni et al. "Manipulating azobenzene photoisomerization through strong light–molecule coupling". en. In: *Nat Commun* 9.1 (Nov. 2018). Number: 1 Publisher: Nature Publishing Group, p. 4688. ISSN: 2041-1723. DOI: 10.1038/s41467-018-06971-y. URL: https://www.nature.com/articles/s41467-018-06971-y.

[112] Jacopo Fregoni et al. “Strong Coupling with Light Enhances the Photoisomerization Quantum Yield of Azobenzene”. In: *Chem* 6.1 (Jan. 2020), pp. 250–265. ISSN: 2451-9294. DOI: 10.1016/j.chempr.2019.11.001. URL: https://www.sciencedirect.com/science/article/pii/S2451929419304784.

Chapter 5

Concluding Remarks

This thesis explored electric fields applications in chemistry, ranging from a semi-classical description of light and matter to a fully quantum modelling of light-matter interactions. The computational approach allowed to obtain insights into spectroscopic experiments and into the energetic and mechanistic effects of electric fields on chemical reactions.

The investigation here reported has been divided into three sections, each one corresponding to a different description of the field-matter system.

The first section studied how the formation of an electric field standing wave affected the absorption spectrum of a sample. Matter has been described as a collection of two-level systems and the electric field as a classical wave. The application of time-dependent perturbation theory allows artifacts due to the standing wave to arise from first principles, and the results are in agreement with the experimental findings. In the linear regime, transition probability significantly depends on the distance from the reflective plate. The manipulation of the wavevectors of the standing and propagating waves emerged as a key factor influencing the behavior of the integrated probability. This modulation allowed to make the integrated probability similar or divergent from the Beer-Lambert model. In the non-linear regime the effects of the standing wave are more evident, producing regions where the transition probability does not depend on the distance from the plate. Further work will need to include interference effects thought to cause the shift in the position of the peaks.

The second section introduced a model for the electrostatic catalysis of chemical reactions. Matter has been described at an atomistic level and the electric field is classical and static. The model provides a framework to compute the smallest possible electric field capable of removing a reaction barrier. It overcomes the principal limitations of traditional electrostatic catalysis models, including the polarizability contributions and considering the effect of the field on the entire potential energy surface, not only on stationary points. The capabilities of the approach are demonstrated in two chemical examples: s-trans to s-cis isomerization of a [3]cumulene derivative and a Huisgen cycloaddition of acetylene and fulminic acid. The electric field eliminates the reaction barrier, with polarizability affecting the field amplitude and direction.

The third and last section addressed polaritons, which are hybrid light-matter

states. A correct description of polaritons requires a quantum description of both matter and the electric field. Two approaches have been presented and applied to simulate electronic structure in presence of strong light-matter coupling, quantum electrodynamics Hartree-Fock (QED-HF) and a parametrized QED approach. QED-HF has been applied to the s-trans to s-cis isomerization of 1,3-butadiene, strictly on the ground state. Upon varying the orientation of the molecule, the isomerization barrier can be either increased or decreased. This effect can be rationalized analyzing the electron density; strong light-matter coupling can localize more electron density in the region of the bond around which occurs the rotation, increasing the barrier. The lowering of the barrier occurs with a similar electron density depletion. A parametrized QED approach has been applied to a trans-to-cis isomerization of 1,3,5-hexatriene, considering several polaritonic states. Employing a field frequency resonant to the lowest allowed electronic transition in the Franck-Condon region, results in polaritonic energy curves on which the isomerization is eased. A 5% detuning of the frequency improves the catalytic effects. The use of a frequency resonant with the lowest electronic transition in the transition state region of the potential energy surface leads to the formation of an intersection between polaritonic states, which could drastically ease the photoinduced isomerization.

List of Figures

Copyright Statement